AN ELECTROSTATIC POSITRON BEAM AND ITS USE IN AN EXPERIMENTAL INVESTIGATION OF THE FIRST EXCITED STATE OF POSITRONIUM

A thesis submitted to the University of London
for the degree of Doctor of Philosophy

David John Day
Department of Physics and Astronomy
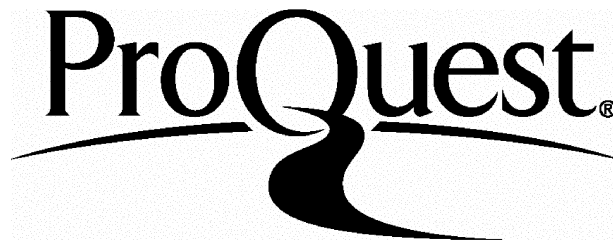University College London

June 1993

ProQuest Number: 10017699

ProQuest 10017699

ABSTRACT

The purely leptonic character of positronium, the bound state of an electron and positron, presents the opportunity to test quantum electrodynamics in the absence of quantum chromodynamical effects. In recent years persistent discrepancies have arisen between experiment and theory for values of the decay rate of the 1^3S_1 state, thus far unreconciled, and therefore investigations of other positronium states desirable.

The main body of this work has involved a study of the first excited state of this system, known as Ps*. Its production by positron impact on solid surfaces was examined, and an experiment to measure the radiative lifetime of the 2^3P_1-1^3S_1 transition performed. In order to carry out this work it was necessary to design an electrostatic positron beam, operable at low transport energies, $\sim 100eV$, with reasonable efficiency and beam quality.

Measurements of the Ps* yield have supported recent disparate measurements by providing a link between, and possible re-interpretation of, some aspects of these studies. Peak yields of several percent were observed from a variety of targets, all without prior surface treatment. Studies of positron re-emission from the same untreated targets were also made in order to estimate the energy régime of the Ps* formed and therefore shed some additional light on the formation process.

An attempt to make the first measurement of a positronium radiative lifetime was made, with many unforeseen difficulties arising. This work has identified the main problems that may be encountered in an experiment of this kind, and steps were taken to minimise their impact, to the point that the transition was isolated. Such steps however have precluded a meaningful analysis of the lifetime by virtue of their effects on the resolution of the measuring system, however as a result of the experience gained through this work the prospects for future successful experiments are much improved.

TABLE OF CONTENTS

FIGURE CAPTIONS

7

(1985)).

10

(●), and relaced with the 280nm filter (○).

for positrons incident on a Cu target ($\bigcirc$).

13

on MgO coated vanes with the sphere in place. Borosilicate slide out (a) and in (b). The time calibration is 0.13nsec/channel.

TABLE CAPTIONS

ACKNOWLEDGEMENTS

For Annette

CHAPTER 1

INTRODUCTION

1.1 Preamble

This thesis is divided into five chapters. Three of these chapters concern experimental investigations whose nature differ sufficiently that an introduction to each subject is warranted. Chapter 2 outlines the design and development of an electrostatic positron beam, chapter 3, the production and detection of the first excited state of positronium, and chapter 4 discusses an attempt to make the first measurement of the radiative lifetime of this state.

Each new area is introduced within its own chapter, and thus only those areas common to all the work presented, such as positronic properties and the slow positron technique, are included in this opening chapter.

1.2 Historical Background

Following the formulation of his relativistic wave equation, Dirac (1930a) proposed the existence of anti-matter to give a physical interpretation to the negative values of energy which arise when solving the expression,

$$E_T^2 = m_0^2 c^4 + p^2 c^2 \qquad (1.1)$$

where E_T is the total energy of a particle with rest mass m_0, c is the speed of light *in vacuo* and p is the particle's momentum. In Dirac's model all energy states below $-m_0 c^2$ are filled with electrons. The Pauli exclusion principle forbids the transition of free electrons into these states. However, if an electron in this 'negative sea' gains enough energy to escape into the free electron continuum, a positive 'hole' will be left behind which will behave as a positive particle.

Initially, to quell those sceptics who demanded evidence of this new particle, Dirac

18

nominated the proton as the anti-electron, however Weyl (1931) showed that the new particle must have the same mass as the electron. It became known as the positron.

The existence of the positron was confirmed experimentally in cloud chamber studies of cosmic rays firstly by Anderson (1932) and later corroborated by Blackett and Occhialini (1933). As the only available example of anti-matter the positron was initially subject to much research purely as an anti-particle, however with the discovery of other anti-particles, the emphasis of positron studies moved more towards the interactions of thses anti-particles with matter. The positron is an ideal candidate in this rôle as many radio-isotopes emit positrons on decay and hence sources of positrons are relatively easy to obtain.

The positron and electron masses are equal. However, they may be distinguished by their opposite charge signs. In many experiments utilising electrons as probes, exchange effects between probe and target lead to difficulties in determining interactions. Atomic scattering experiments and electron diffraction are examples. Benefit may be gained in these areas by the replacement of electrons by positrons as the probe, as they may be easily distinguished from target electrons and hence any ambiguity is removed. The differences between positron and other particle interactions are also of great interest and complement existing techniques. This is particularly clear in the case of atomic scattering experiments where positrons, electrons, protons and antiprotons have all been used and allow direct comparison between the interactions of each probe (eg. Charlton et al (1988)). The effects of mass and charge can clearly be seen and, therefore, put theoretical models of the scattering process to the test.

Positrons can annihilate with their electron counterparts with the release of a number of γ-rays, the total energy of which will be approximately equal to the sum of the particles' rest masses and kinetic energy, minus their binding energy. A particular case is that of two γ-ray annihilation. Here, for particles at rest, photons are emitted collinearly with equal energy. This fact along with the law of conservation of linear momentum may be used to good effect for positrons interacting with electrons in a bulk. The velocity of a positron in a solid is, for reasons discussed in §.1.4, very small in comparison to the

Fermi surface electrons associated with the atoms in the solid, and as a result any departure from collinearity in γ-rays from annihilation is mainly attributable to the momentum of the electrons of the solid. In addition, the rate at which positrons annihilate in any medium is an indirect indication of the effective electron density of that material.

The attractive nature of the electron/positron Coulomb interaction leads to bound states of the two particles, known as positronium, or Ps. As a purely leptonic atom, Ps is of great interest to theorists as it provides a testing ground of the two body formalism of QED, in an environment free from strong interaction, QCD, effects. Further, positronium offers opportunities to those studying neutral probe interactions (eg. Zafar *et al* (1991)), as the atom is several orders of magnitude lighter than the most common of neutral probes used in atomic physics, the He atom.

Another system of great interest to theorists, is the bound state of a positron and an antiproton, known as antihydrogen ($\hat{\text{H}}$). This atom offers the possibility of the most accurate tests of CPT to date (Deutch *et al* (1992)), as the symmetries underlying the theorem demand that the laws of physics are the same for both matter and anti-matter and is integral to gauge field theories. Comparison of the magnitudes of the H and $\hat{\text{H}}$ Lamb shifts is one example. Details of experimental efforts to produce this exotic atom, and of planned subsequent experiments, are discussed by numerous authors in 'Antihydrogen' (1993).

1.3 Basic Properties of Positrons and Positronium

CPT invariance requires that the properties of the positron and electron be the same, the exception being that the charge and magnetic moment will have opposite signs. So far the positron mass has been measured by Cohen and Taylor (1973) and found to be $(511.0034 \pm 0.0014)\text{keV/c}^2$, and a limit on any departure from equality of the positronic to electronic charge has been set at $1 \pm 4 \times 10^{-8}$ (Hughes and Deutch (1992)).

As mentioned above, positron annihilation on interaction with electrons almost always results in the emission of γ-rays, with a total energy of $\approx 1.022\text{MeV}$. The charge parity

of single photons is -1, and so, for a system of n photons, the total charge parity is given by

$$P_c = (-1)^n \qquad\qquad (1.2)$$

Yang (1950) demonstrated, using symmetry arguments, that for the annihilation of the positron/electron system, P_c is determined by

$$P_c = (-1)^{L+S} \qquad\qquad (1.3)$$

where L is the total angular momentum and S the total spin of the positron/electron pair. It can be seen from eqn.1.2 that the total parity will either be 1 or -1 and therefore that the number of photons simply restricted to an odd or even n, depending on the combination of L and S.

The probability of annihilation into n photons may be estimated by inspection of the Feynman diagram for each positron/electron/photon interaction. The cross-section for decay by a given number of photons is approximately proportional to the number of vertices, corresponding to photon emission or absorption, in the diagram. Each vertex contributes a factor of α, the fine structure constant to the cross-section, given by

$$\alpha = \frac{e^2}{2\epsilon_0^2 hc} \approx \frac{1}{137} \qquad\qquad (1.4)$$

here e is the electronic charge $(1.602 \times 10^{-19}C)$, ϵ_0 is the permittivity of free space $(8.854 \times 10^{-12} Fm^{-1})$, h is Planck's constant $(6.624 \times 10^{-34} Js)$ and c is the speed of light $(2.998 \times 10^8 ms^{-1})$.

Fig.1.1 (a)-(e) illustrates a number of possible modes of annihilation of the positron/electron pair via 1γ, 2γ, 3γ, 4γ and radiationless decay. Both (a) and (c) have three vertices and so in terms of radiative coupling the cross-sections would be the same. The single photon case, first observed by Sodickson et al (1961), requires a third body to conserve momentum and thus the total probability is less than that of 3γ decay. Of all

21
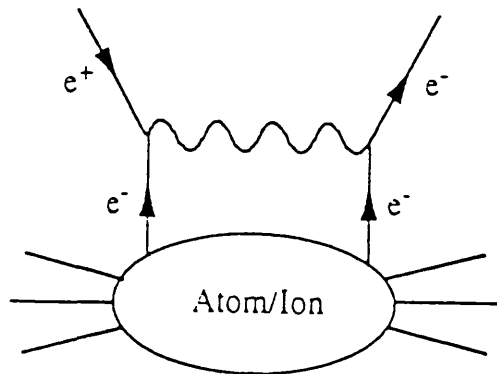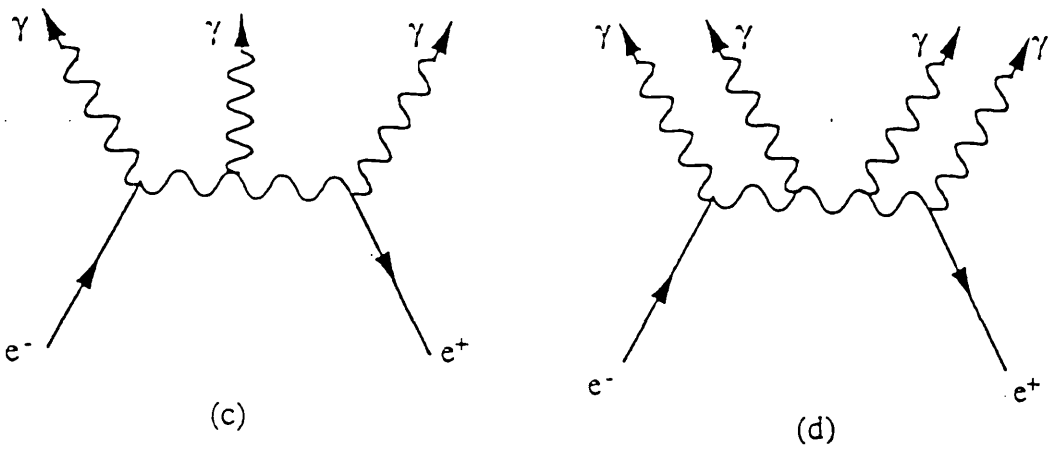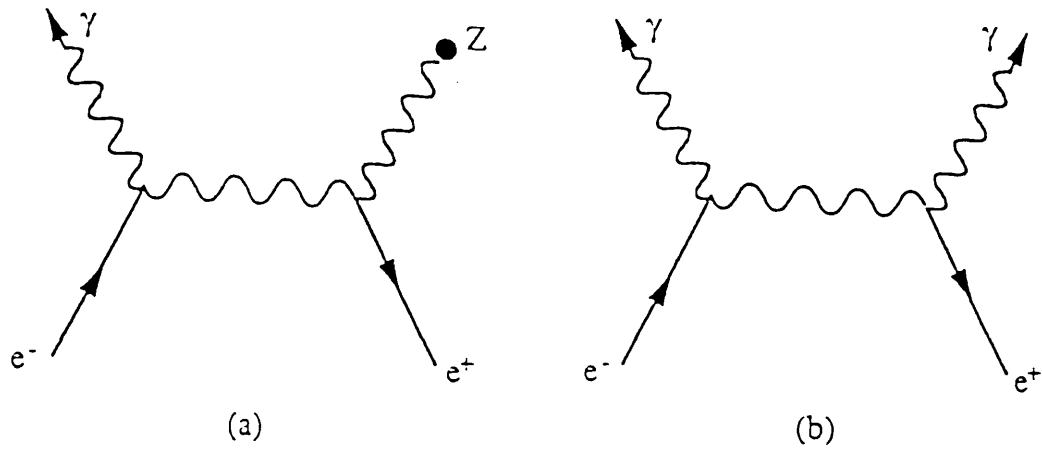
Figure 1.1 Feynman diagrams for electron/positron annihilation into (a) one, (b) two, (c) three, (d) four, and (e) zero photons.
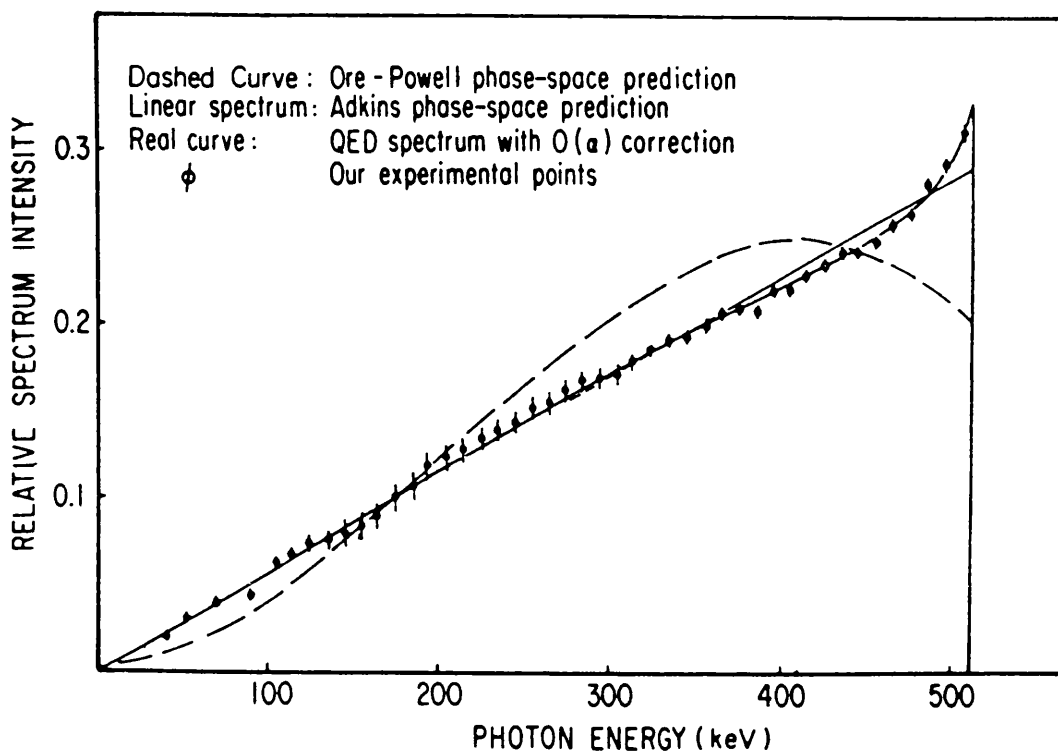
Figure 1.2 The energy distribution of γ-rays resulting from o-Ps decay (Ore and Powell (1949), Chang *et al* (1982,1985)).

the processes, (b), that of two photon annihilation has the highest probability of occurrence, with the lowest number of vertices. Ore and Powell (1949) calculated the ratio of 2γ to 3γ decays, the next most probable mode, to be 372:1. Radiationless annihilation, (e), first proposed by Brunings (1934), has the lowest probability, and was believed to have been observed by Shimizu *et al* (1965). However, recent calculations suggest that the cross-section may be much lower than that observed (Mikhailov and Porsev (1992)). Four photon annihilation, with four vertices (d), has been recently observed by Adachi *et al* (1990), with a rate in reasonable accord with theory.

The attractive Coulombic potential allows bound states of the electron/positron pair. In the ground state, where L=0, the relative orientation of the positron and electron spin determines the mode of annihilation, to satisfy charge parity, and as a result the rate of decay. The S=0 state, where the spins are antiparallel, is a singlet known as para-positronium, p-Ps, which has a lifetime against annihilation of ≈ 125psec and decays by

the two photon process. The S = 1 state, where the spins are parallel, is known as ortho-positronium, o-Ps, and is a triplet. Ortho-positronium decays by a three photon process and has a lifetime of $\approx$ 142nsec, longer than p-Ps as the cross-section for annihilation is lower. As discussed above, the two photon decay mode leads to the emission of collinear photons of equal energy, for particles at rest. Three photon annihilation however, results in coplanar photons with an energy distribution like that of fig.1.2. Here, the theoretical predictions of Ore and Powell (1949) show close agreement to the measurements of Chang *et al* (1982 and 1985). A more detailed discussion of positronium decay rates is given in chapter 4. It should be noted that for excited states of positronium, the orbital angular momentum becomes significant in determining annihilation modes, and as a result the S = 0 and S = 1 states will not always decay via two and three photons as in the ground state.

1.4. The Slow Positron Beam Technique

1.4.1 Introduction

Positrons may be obtained in a number of ways in the laboratory. The most convenient sources are radioisotopes. Many radionuclides emit positrons; table 1.1 lists the characteristics of a number of commonly used radionuclides.

Table.1.1 Some commonly used β^+ emitters.

Isotope	β^+-Branching Ratio	Endpoint Energy (MeV)	Half-life	Production Mechanism
^{22}Na	0.89	0.54	2.6 years	^{24}Mg (d,α)
^{58}Co	0.15	0.47	71 days	^{58}Ni (n,p)
^{64}Cu	0.19	0.65	12.6 hours	^{63}Cu (n,γ)

The parameters of the most importance are the branching ratio, which is the fraction of decays which result in positron emission (as opposed to electron capture), and the half-
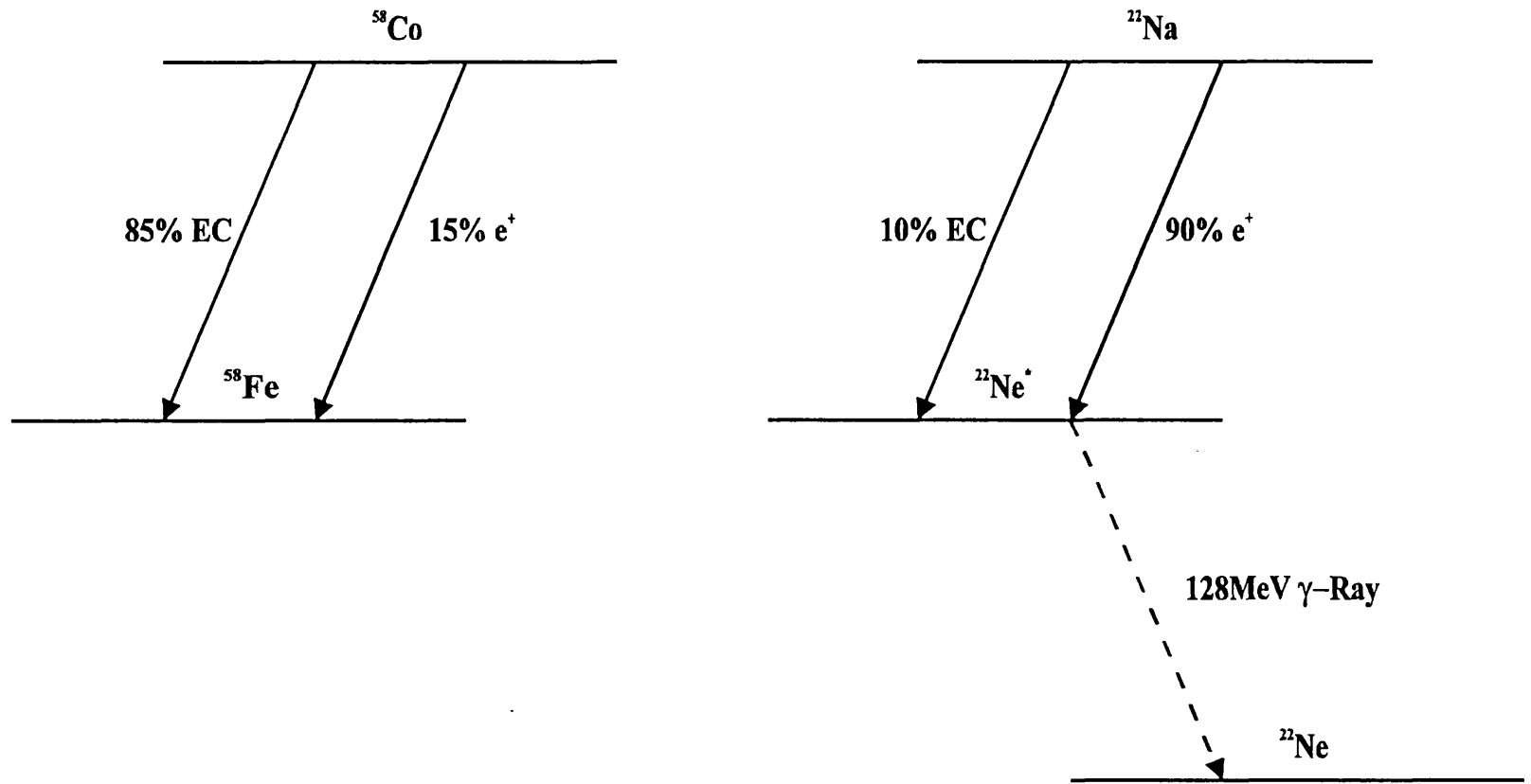
Figure 1.3 A schematic diagram of the decay schemes for ⁵⁸Co and ²²Na.

life. Another important consideration is the specific activity, which determines the physical dimensions of the source. The two most commonly used positron emitters are ^{22}Na and ^{58}Co. Fig.1.3 is a schematic diagram of the decay processes for both sources.

A somewhat more indirect source of positrons is the electron accelerator. Here electrons are accelerated to energies of tens of MeV and impinged on a target, often tantalum. The bremßtrahlung produced as the electrons are slowed will be in the $>$ 1MeV γ-ray range, thus allowing pair production to take place. These positrons are then used in the same way as described below.

Early positron experiments used the β^+-particles directly from radioactive sources, known generically as swarm experiments for their broad range of particle energies. This work proved invaluable, allowing the discovery of positronium by Deutsch (1951), the first decay rate measurements by the same author, and of the first use of positrons as probes in gaseous and solid media. However, the nature of swarm experiments, the wide range of positron energies, directions and background, due to γ-rays from the source and annihilating positrons, places severe restrictions on the information retrievable. A source of monochromatic positrons, which could be used to form a collimated beam away from background was needed.

Madanski and Rasetti (1950) proposed that positrons of thermal energies could be obtained by implanting β^+ particles from a radioactive source into a solid and which would then diffuse back to the surface. Their experiments produced null results, and it was Cherry (1958) who produced the first working 'moderator', however they did correctly predict that the efficiency of such a moderator was dependent on the ratio of the diffusion length of the positrons in the medium, and to the implantation depth of the positron within the material. They calculated a value of $\sim 10^{-3}$, although it was not until 1979 that Mills observed efficiencies of this order in his work with well-characterised Cu(111) single crystal surfaces. Fig.1.4 shows the calculated enhancement of the slow positron yield obtained by moderating the primary β^+ flux from a ^{58}Co source (Schultz and Lynn (1988)). An almost six orders of magnitude increase in the slow positron yield over the primary β^+'s in the same energy range, is predicted.
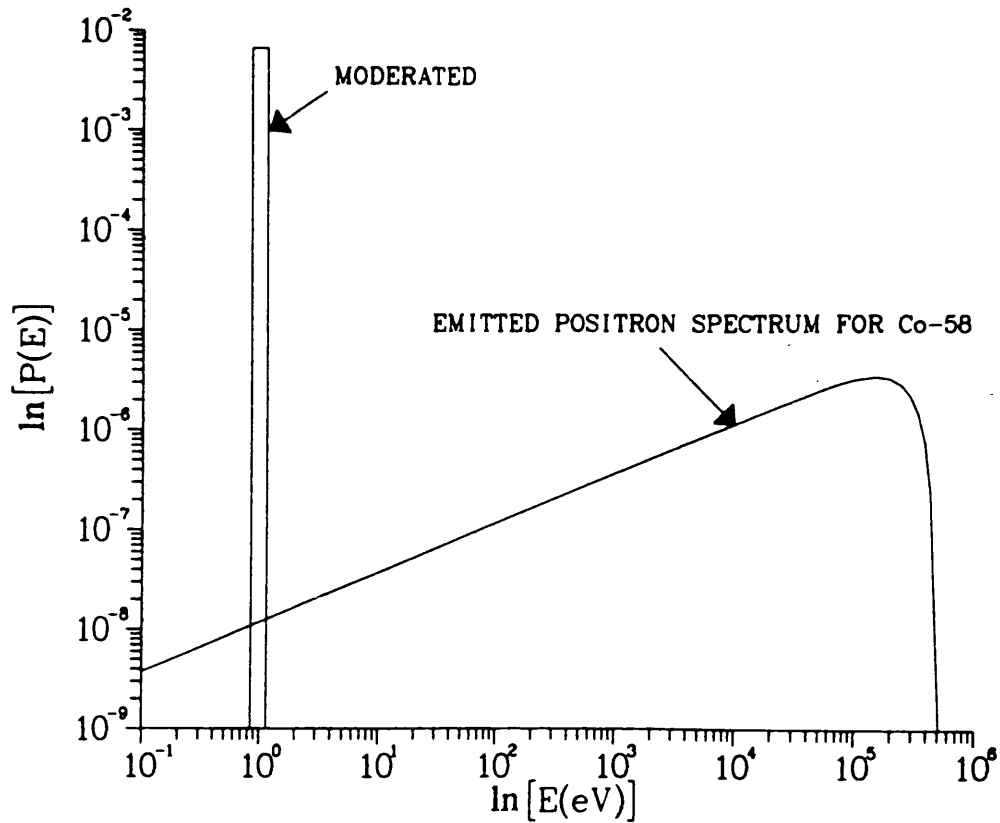
Figure 1.4 A comparison of the calculated slow positron yield from a W(110) moderator with the primary β^-'s in the same energy range directly emitted by a ^{58}Co source (Schultz and Lynn (1988)).

1.4.2 Moderation

When a positron is implanted into a solid it may lose energy in a number of ways. Each process may be the dominant source of energy loss over a given energy regime. For positrons with energies of a few MeV and above, the principle modes of energy loss (or slowing down) are by bremßtrahlung (Kim *et al* (1986)), where the positron interacts with the screened Coulomb field of a nucleus or one of the orbital electrons, and Čerenkov radiation. In the several hundred keV range, inelastic electron scattering becomes important, and below ≈ 100keV most of the positron's energy is lost through core and valence electron excitation and ionisation (Schultz and Campbell (1985) and Lennard *et al* (1988)). These processes lead very rapidly, $\sim 10^{-13}$sec, to the reduction of the positron's energy to a few tens of electron volts. Bulk lifetimes against annihilation for

positrons in solids are $\sim 10^{-10}$sec, so many implanted positrons survive long enough to achieve these energies. Not only does a positron lose energy in collisions but it will also undergo changes in direction, and it is elastic collisions with the highly charged nuclei that are chiefly responsible for this directional change. Therefore, the location of the positron within the bulk after this initial slowing down depends on the depth of implantation, which is of course dependant on the initial energy, and the atomic number (Z) of the material. Further slowing of the positron occurs, but these processes depend on the classification of the material.

In metals, conduction electron scattering, and in particular plasmon excitation (Zhang *et al* (1988)), dominates the slowing down process for positrons with energies around the Fermi energy, ϵ_f. At energies well below ϵ_f the final stage of slowing, or thermalisation, is predominantly by phonon scattering and takes $\sim 10^{-12}$sec. Fig. 1.5 shows the energy loss rate, as a function of positron energy in aluminium (Nieminen and Oliva (1980)) at a number of sample temperatures. It can be clearly seen that, as the temperature increases, the energy loss rate also increases, and therefore phonon scattering dominates. Above a few electron volts however, the energy loss rate does not change with temperature, indicating that for positrons above this energy, electron scattering becomes the more important energy loss process.

Fig. 1.6 is a schematic showing the range of the above energy loss mechanisms in each class of material (after Schultz and Lynn (1988)). For insulators there are no conduction electrons available to assist in thermalisation. In this case, when the positron's energy falls below that of the band gap, production of electron/hole pairs becomes impossible. So the only mode of energy loss is by phonon scattering. Semi-conductors exhibit similar features. Though here, as the band gaps are smaller, the phonon scattering begins to dominate at lower energies than in good insulators. Thermalisation of positrons in these materials is therefore a slower and more inefficient process than in the case of metals.

Not all positrons will undergo complete thermalisation when implanted into a solid. Fig. 1.7 is a diagram summarising the near surface interactions, and their time scales, for incident positrons with kinetic energies less than 100keV (after Schultz and Lynn (1988)).

28
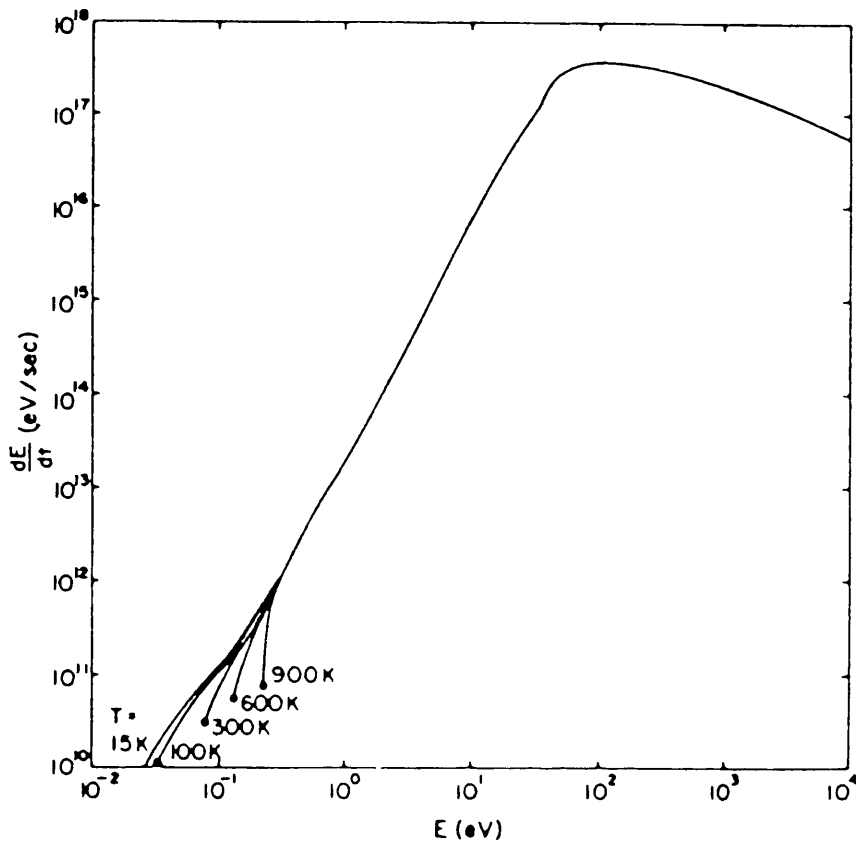
Figure 1.5 The energy loss rate as a function of energy for positrons in aluminium, for a range of sample temperatures (Nieminen & Oliva (1980)).
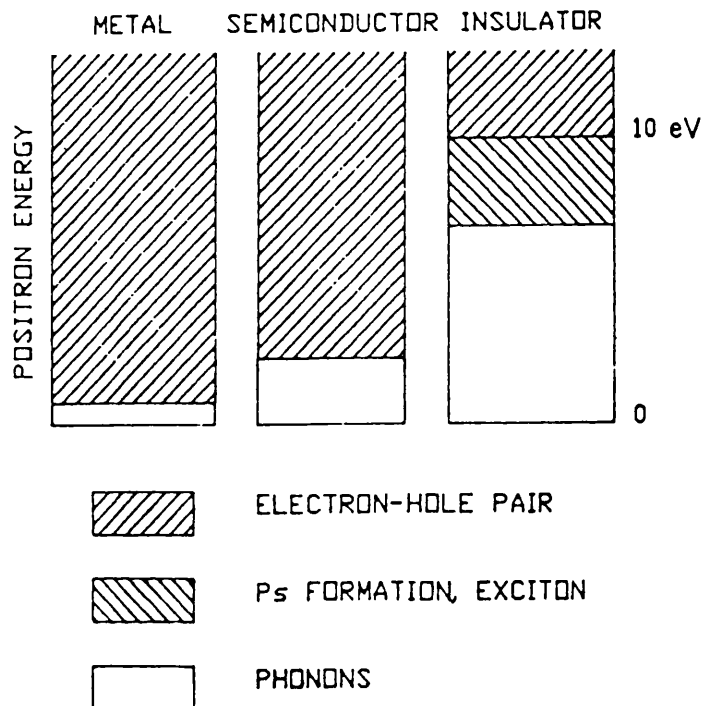
Figure 1.6 A schematic diagram showing the régime of positron energy loss processes in each class of solid (Schultz & Lynn (1988)).

29

(a) FIRST ENCOUNTER: $0 \lesssim T \lesssim 10^{-15}$ sec
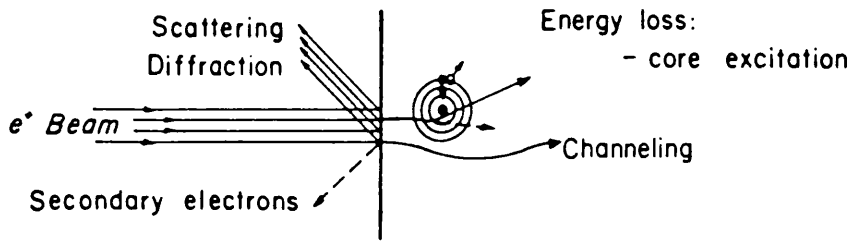
(b) ATTAINING EQUILIBRIUM: $0 \lesssim T \lesssim 10^{-12}$ sec
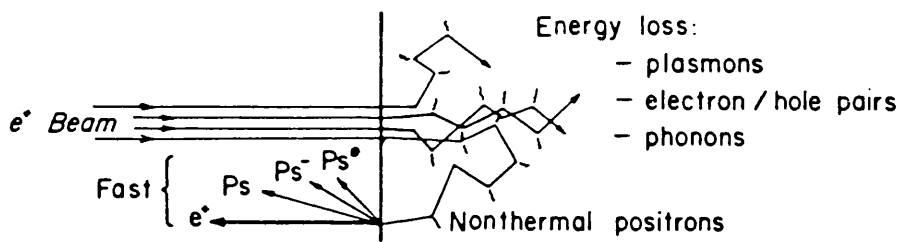
(c) EQUILIBRIUM: $0 \lesssim T \lesssim 10^{-10}$ sec
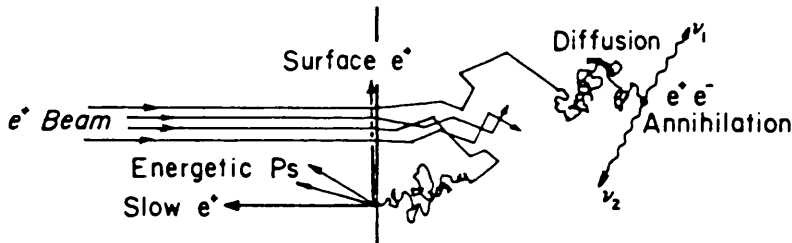
(d) LONGER TIMES: $0 \lesssim T \lesssim 10^{-7}$ sec
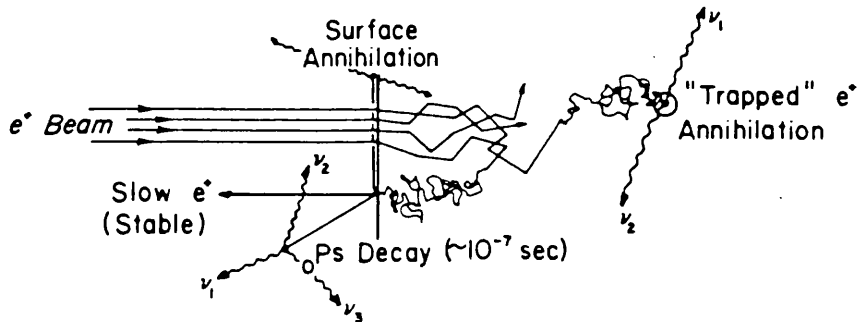
Figure 1.7 The interaction of a positron beam of energy < 100keV with the near surface region of a solid (Schultz & Lynn (1988)).

30

Non-thermalised positrons may backscatter out of the samples with energies ranging from that of the primary beam down to several eV. For positrons at the low energy end of the range, positronium formation becomes a possibility by the pick-up of an electron at the surface on exit. Both processes are of extreme significance to excited positronium formation and are discussed more fully in chapter 3.

The fate of positrons which thermalise far from the surface of entry (and exit in the case of thin samples) is to diffuse through the bulk until finally they annihilate with an electron. The probability of this occurring is higher in materials with high electron densities, and hence bulk lifetimes in insulators tend to be longer than those in metals. Bulk defects such as discontinuities or impurities may lead to trapping of the positron thus reducing its mean free path and further shortening bulk lifetimes. By annealing crystalline materials, some defects can be removed, therefore improving positron mobility. For positrons which thermalise close to the surface of a solid, the possibility of re-emission into the vacuum is possible if the positron occupies a lower energy state outside the material than inside. The resulting energy difference is known as the positron workfunction, ϕ^{+}, and is analogous to the electron workfunction, ϕ^{-}. Both are given by

$$\phi_{\pm} = \mp D - \mu_{\pm} \tag{1.5}$$

where D is the attractive/repulsive surface dipole normal to the exit surface experienced by the positron/electron due the electron gas 'spilling out' beyond the surface of the metal. The magnitude of this dipole will be the same for both positrons and electrons, only the direction of the force on the particle changes. The particle in the solid also interacts with the ion cores and conduction electrons and it is these that compose the bulk potential, $\mu_{\pm}$, the magnitude of which will differ for positrons and electrons. Positrons will be repelled by the cores and attracted by the conduction electrons, whereas for an electron the opposite is true. At the surface, the dipole will act to push the positron out of the material. Emission however, will only occur if the magnitude of the dipole is greater than the bulk potential. Fig.1.8 is an illustration of the potential as seen by a positron. V_0 is the interaction due to the ionic cores, and V_{corr} is the potential due to correlation with the conduction electrons which compose the bulk potential, μ_{+}. One can

$$\phi_+ = -D - \mu_+$$

$$\phi_- = +D - \mu_-$$
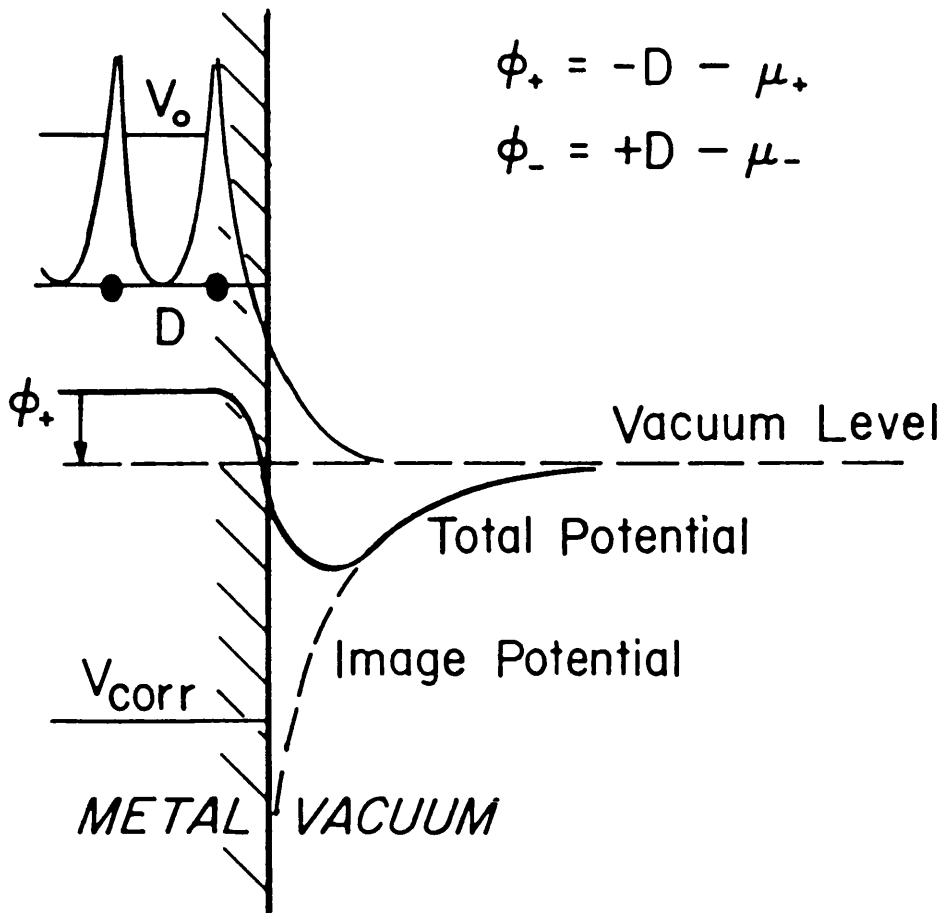
Figure 1.8 A schematic diagram of the potential energy as seen by a positron at a negative workfunction surface (Schultz & Lynn (1988)).
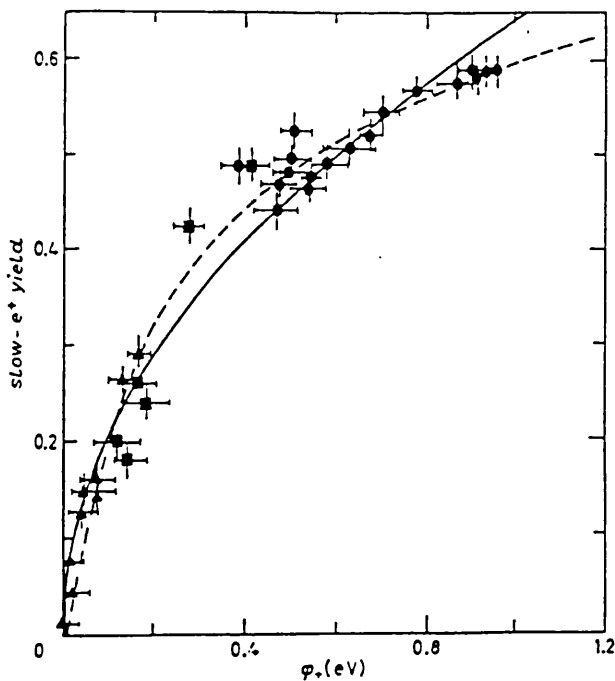
●, ▲, ■ Experimental - - -, —— Theoretical

Figure 1.9 The re-emitted positron yield from copper as a function of positron workfunction (Murray & Mills (1980)).

32

see that here the workfunction becomes negative just outside the surface. For many metals this is the case, and thus have a 'negative workfunction' for positrons.

The surface branching ratio for slow positron emission increases with the positron workfunction, ie. the more negative ϕ^+, the more re-emitted positrons. Fig.1.9 is the slow positron yield as a function of positron workfunction for Cu as measured by Murray and Mills (1980). They changed the workfunction by overlayering the surface with sulphur and by changing the crystal orientation. For a clean surface the energy spread of the re-emitted moderated positrons, ΔE, is just kT, the product of Boltzmann's constant and the temperature in Kelvin. However, in practice, the width is often of the order of ϕ^+ due to scattering by contaminants at the surface.

A few metals and many insulators and semiconductors are believed to have a positive ϕ^+. This is because the surface dipole is small, in the case of insulators as there are no conduction electrons. Thermalised positrons will not be emitted to vacuum by these materials as the positrons will not have sufficient energy to overcome the surface potential. Positron re-emission is still observed from these positive workfunction materials however, but the mechanism is believed to rely on those non-thermalised positrons which reach the surface of the solid. For a positron with an energy below that of the band gap the only possible energy loss mechanism is phonon creation. In general, the band gap energy for a solid is fairly small, often smaller than the workfunction of the material. Thus even those positrons not subject to further energy loss may not escape. Rare gas solids (RGS) however, are a class of materials from which the highest yields of non thermalised re-emitted positrons have been observed In the case of RGS however, the optical phonon creation channel is not available and, therefore, only the less efficient acoustic phonon creation channel exists to further slow the positron down. As the band gap is so large in RGS moderators, a large number of epithermal positrons reach the surface of the solid with sufficient energy to overcome the small positive workfunction. The highest yield so far from a RGS moderator was that measured by Mills and Guillikson (1986) of 0.70(2)% from Ne with a ΔE of 0.58(5)eV. This may be compared with the highest values for a metallic moderator, 0.3% for an annealed W(110) sample with a ΔE of 0.7eV, measured by Vehanen et al (1983). Of additional interest is the

formation of the first field assisted moderator demonstrated by Merrison *et al* (1992). Here by surface charging a solid argon moderator (impossible for a metallic moderator of course) a factor of 3-4 increase in the slow positron yield was achieved.

Another possible non-metallic high yield moderator is diamond. Again a material with a large band gap, diamond is different to RGS moderators in that it is believed to have a negative positron workfunction, measured by Brandes *et al* (1992). Re-emission studies, also Brandes *et al* (1992), suggest that while diamond is a low density material, it may have an efficiency in excess of 0.7%, while being much easier to handle than RGS moderators. As with all non-metals, the possibility of constructing a field assisted moderator is also available.

An important factor in enhancing the effectiveness of a moderator is the source/moderator geometry, which is dependent on the source and moderator material used. Fig. 1.10 shows the commonest geometries used. The backscattering type, (a), is suitable for a small source which will not shadow the moderator excessively. In (b), the moderator has a vane construction, the angle of the vanes ensures that the implantation depth of the primary positrons will be less than in the backscattering case, also the effective area of the moderator is larger and thus this is likely to be a more efficient system than (a). (c) is probably the most commonly used geometry at this time. Meshes, usually tungsten, provide a robust, easily handled system, though as they have a finite transmission, will not intercept all the primary positrons and thus not as efficient as (a) or (b). In addition to this the energy and angular spread of the e^+ emitted from such mesh moderators is rather poor as the re-emitted positrons are likely to be scattered a number of times before leaving the multiple meshes. This effect is worsened as the wires of the mesh have round cross-sections and so positrons will be emitted at a range of angles initially. (d), a cup arrangement and (e) a cone, are usually used with RGS moderators, which may be easily deposited onto such surfaces. These geometries give a 'second chance' to those positrons which do not thermalise, yet re-enter the moderator. The thin foil arrangement, (f), is another common moderator geometry. It is superior to (a), (b), (c), (d) and (e), in that the moderator is not shadowed by the source. If close the whole 2π flux from the source is intercepted and the energy and angular resolution of foils is better than that of meshes,
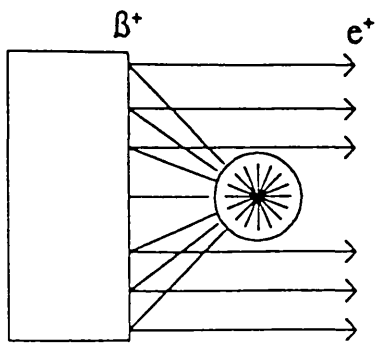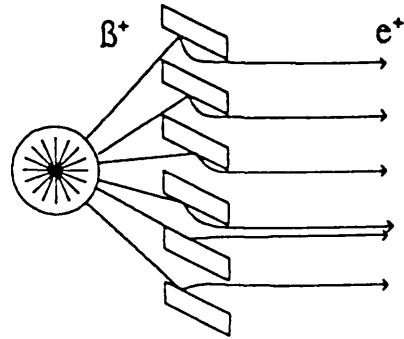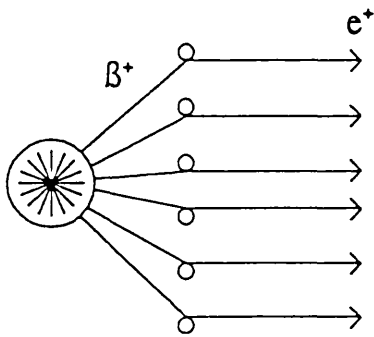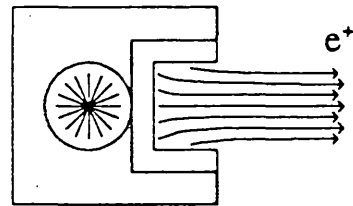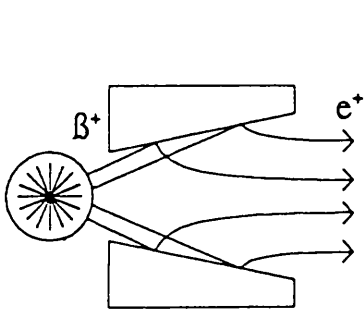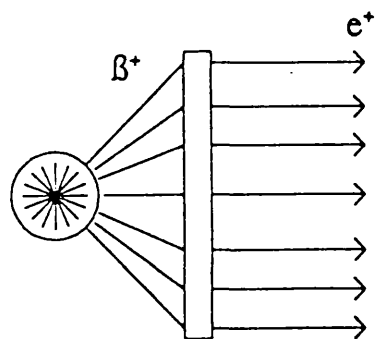
Figure 1.10 Common moderator geometries: (a) backscattering, (b) vanes, (c) grid, (d) cup, (e) cone and (f) transmission.

see §.1.4.3.3, however the benefits of using thin foils are somewhat offset by being difficult to handle. Since the first moderator was constructed, increases in efficiencies by a factor $> 10^5$ have been achieved. In addition to these achievements, methods to transport these positrons away from the source and to an interaction region as a beam, are constantly improving. It is still a sobering thought however, that with all the advances made in the field in the last forty years, the largest slow positron facility being developed in the world to date (Brookhaven National Labs, Weber *et al* (1992)) is still at least a million times less intense a source of positrons than the simple heated filament electron source. Table 1.2 outlines some important events in moderator development.

Table 1.2 Some highlights in moderator development.

Moderator	Experimental Arrangement	Efficiency	ΔE (eV)	Reference
Pt, K, Ga	Transmission	0	-	Madanski & Rasetti (1950)
Cr/Mica	Transmission	3×10^{-8}	-	Cherry (1958)
Au/Mica	Transmission	10^{-7}	2	Costello *et al* (1972)
MgO coated Au	Backscattering/Vanes	3×10^{-5}	2.3	Canter *et al* (1972)
B	Self-moderator	10^{-7}	0.15	Stein *et al* (1974)
Al(100)	Backscattering	3×10^{-5}	0.1	Mills *et al* (1978)
Cu(111)+s	Backscattering	9×10^{-4}	0.3	Mills (1979)
W	Backscattering/Vanes	7×10^{-4}	1.3	Dale *et al* (1980)
W(110)	Backscattering	3×10^{-3}	0.7	Vehanen *et al* (1983)
W(100)	Transmission, High vacuum	6×10^{-4}	3	Lynn *et al* (1985)
Ne	Transmission	7×10^{-3}	0.58	Mills & Gullikson (1986)
W(100) Ni(100) Mo	Transmission, High vacuum	5.9×10^{-4} 6.6×10^{-4} 7.5×10^{-5}	- - -	Gramsch *et al* (1987)
W(100) Ni(100)	Transmission, low vacuum annealing	8.8×10^{-4} 6.5×10^{-4}	1.7 0.3	Zafar (1988 & 1989)
Ar	Transmission/Field assisted	7×10^{-3}	-	Merrison *et al* (1992)

1.4.3 Positron Transport

After the discovery by Cherry (1958) of the first source of re-emitted moderated positrons, it was not until 1968 that Groce *et al* attempted to produce the first guided beam of slow positrons for atomic physics purposes. Improvements in beam technology soon followed and as a result, positron physics experiments have become much more sophisticated.

There are two distinct ways in which slow positrons may be transported, magnetically or electrostatically. For those experiments which require a knowledge of only the axial component of the positrons' energy, magnetic transport, in which the positrons motion is a combination of axial and transverse velocity components, may safely be used. For this reason the magnetic transport system remains the most widely used beam technique employed by e^+-researchers. This is in contrast to the formation of an image by a positron microscope for example, where the positrons motion must be clearly defined. Table 1.3 shows a few examples of experiments performed using both transport methods.

Table 1.3 Some examples of experiments utilising electrostatically or magnetically guided beams.

Experiment	Transport	Reference
$\sigma(e^+)_T$ for He	Magnetic	Costello *et al* (1972b)
$d\sigma(e^+)/d\theta$ for Ar	Magnetic	Coleman & McNutt (1979)
LEPD/LEED comparison	Electrostatic	Weiss *et al* (1983)
$d\sigma(e^+)/d\theta$ for Ar	Electrostatic	Floeder *et al* (1989)
Positron re-emission microscopy	Electrostatic	Brandes *et al* (1988)

1.4.3.1 Magnetic Transportation

A typical magnetically guided beam, such as that shown in fig.1.11, consists of a source of slow positrons extracted from the region of moderation by an accelerating potential,

Stainless Steel shielding

Source/moderator
assembly

2" diffusion pump

E x B deflector plates

Pb shielding

8mm aperture

Scattering
region

6" diffusion pump

Positron extraction
tubes

MCP
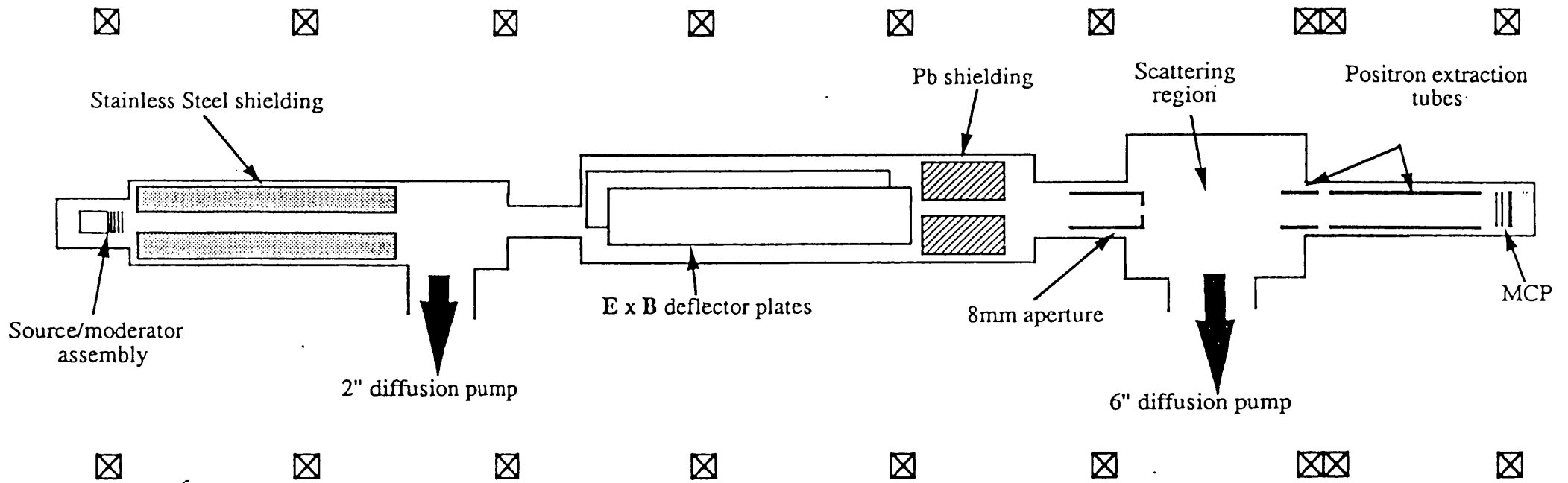
Figure 1.11 A schematic diagram of a typical magnetically guided positron beam.

and confined to their axis of propagation by an axial magnetic field. This is achieved by transporting the beam through a series of coaxial Helmholtz coils separated by a distance equal to the coil radius in which case the field in the central region is uniform. Typical field strengths for slow positron beams are $\sim 10^1$-10^2 Gauss. It should also be noted that, particularly for beams operated at low energies, it is also necessary to annul the Earth's magnetic field.

The motion of the positrons guided in this manner is not simply co-axial, since the application of the parallel magnetic field causes any transverse component of the positron's velocity to be converted into orbital motion about the magnetic field lines. The trajectory of the positron is therefore helical on or near the axis depending how close to the axis the positron starts off. The actual diameter of the beam thus formed is governed by the spatial extent of the slow positron source, in practice the moderator, and the radius of the positrons motion about the field lines, the Larmor radius, which is typically < 1mm. Moderator diameters are selected to suit the particular source used. For commonly used source materials and activities, beam diameters are of the order of a few millimetres. This can result in a very high transport efficiency, approaching unity, for some of these systems.

By transporting the slow positrons away from the source, problems due to source initiated background may be much reduced. Further improvements to this situation is achieved by inserting an $\mathbf{E} \times \mathbf{B}$ filter between the source and interaction region. This, in its simplest form consists of two parallel plates immersed in the Helmholtz field. An electric field is applied orthogonally to both the magnetic field and direction of propagation, the consequence of this is to translate the beam by an amount proportional to the Lorentz force due to the cross product of the two fields. As a result of the extended nature of the beam, simple parallel plates can lead to distortion of the beam profile. This however, may be much reduced with their substitution by curved plates (Hutchins et al, 1986). The energy resolution of these filters is sufficiently broad to allow the transmission of all positrons which have undergone the moderation process, however any residual fast β^+-particles, and of course γ-rays from the source, will not be deflected and may be stopped with suitable shielding material.

1.4.3.2 Electrostatic Transportation

Electrostatic beams are generally more complicated in construction than their magnetic counterparts. This is because even a relatively simple system consists of a number of elements each with a different function, and hence different design. It is also necessary to ensure that there are no stray magnetic fields present in the vicinity of the beam and so elaborate μ-metal shielding or correction coils are employed for this purpose. A good measure of the quality of a positron beam is the 'brightness per volt' (Canter and Mills (1982)), r_v, of the beam given for small angles by

$$r_v \approx \frac{\varepsilon}{4d^2\theta_d E^2} \tag{1.6}$$

where ϵ is the moderator efficiency, θ_d is the angular divergence in radians, d is the beam diameter and E is the kinetic energy. In order to satisfy Liouville's theorem, which states that phase space is always preserved under conservative forces, the product $\theta_d d\sqrt{E}$=Constant. So it can seen that a reduction in $\theta_d d$ can only occur if the kinetic energy is increased. By using different lens combinations and potentials, focusing at constant energy may be achieved, but again it should be noted that any improvement of one of the parameters is at the expense of the others.

1.4.3.3 Divergence on Emission

The magnitude of $\theta_d d$ is dependent on the choice of source and moderator. It is obvious that, for efficient moderation, the moderator itself must be larger than the source. Therefore to reduce d compact sources are useful. The high specific activity and mechanical stability of ^{58}Co for example, permits large source strengths to be achieved from unsealed, and hence less attenuated, compact areas. ^{58}Co sources of 100mCi may be as small as several mm^2 and open, whereas the equivalent ^{22}Na source would have to be encapsulated and the effective active area much larger.

Primary moderators generally fall into two categories: meshes and foils. There is no preferential direction of emission from meshes, it is 4π. For foils however, positrons that

stop close to the exit surface are likely to be emitted in the forward direction due to the nature of the workfunction process. For clean surfaces, the component of the emitted positron's velocity transverse to the moderator surface, $v_\parallel$, is just $(kT/m_o)^{1/2}$ as shown in fig. 1.12, where k is Boltzmann's constant, T is the temperature in Kelvin and m_o is the positron mass. It can be seen that $\theta_d \approx \tan^{-1}(v_\parallel/v_\perp)$, where $v_\perp$ is the velocity component normal to the surface, and it is therefore possible to reduce θ_d, thus improving the brightness, simply by cooling. However, this is only done in practice in a reflection geometry due to the difficulties in cooling a transmission foil (Canter *et al*, 1986) and thus is generally used in systems employing the re-moderation technique of brightness enhancement (see § 1.4.3.4).

1.4.3.4 Brightness Enhancement by Re-moderation

As discussed above for conservative forces, phase space is preserved, and hence the initial trajectories of the positrons emitted from the moderator dictate the quality of the beam. One technique to improve beam quality is known as brightness enhancement as outlined by Mills (1980). Fig. 1.13 is a schematic diagram of the process, which relies on the non-conservative nature of the moderation process. If one accelerates a beam of slow positrons to several keV, thus reducing the beam diameter, and implants them into a second moderator generally a single crystal thin film of ~ 1000Å thickness in transmission (a thicker crystal in reflection), then the area from which the positrons are re-emitted after thermalisation will be dependent on the area of the incident beam and the diffusion length (~ 1000Å) of the positrons in the re-moderator. As the moderation efficiency for keV positrons is much higher than for primary β^+-particles, useful enhancements to r_v may be achieved, and demonstrated to great effect by positron microscopists (Canter *et al* (1987)).
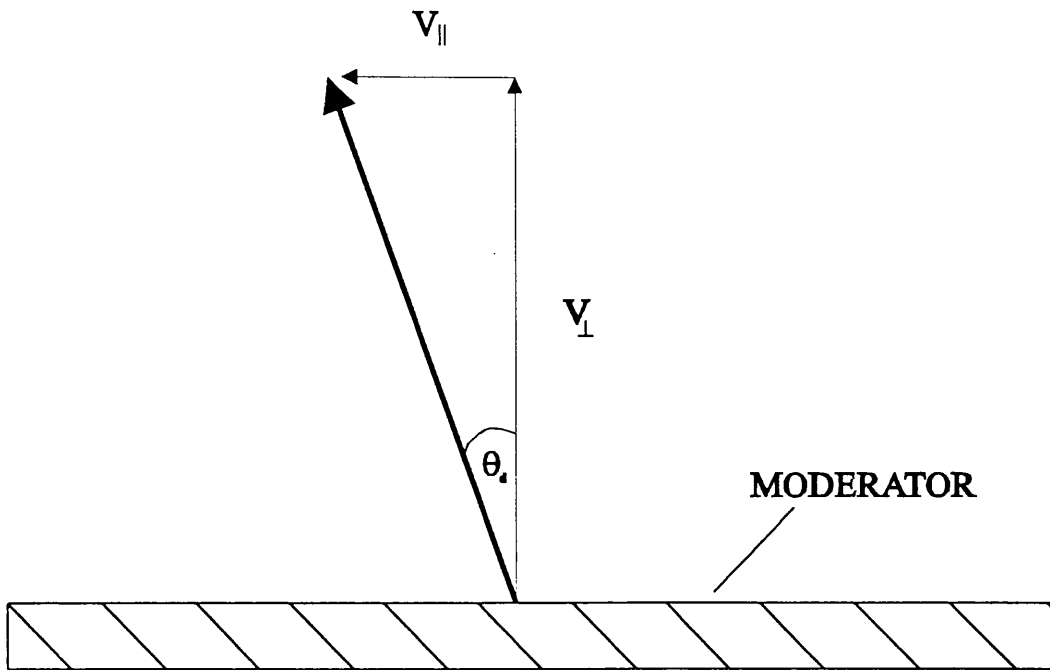
Figure 1.12 A schematic diagram showing the velocity components of a re-emitted thermalised positron, after leaving the moderator surface.
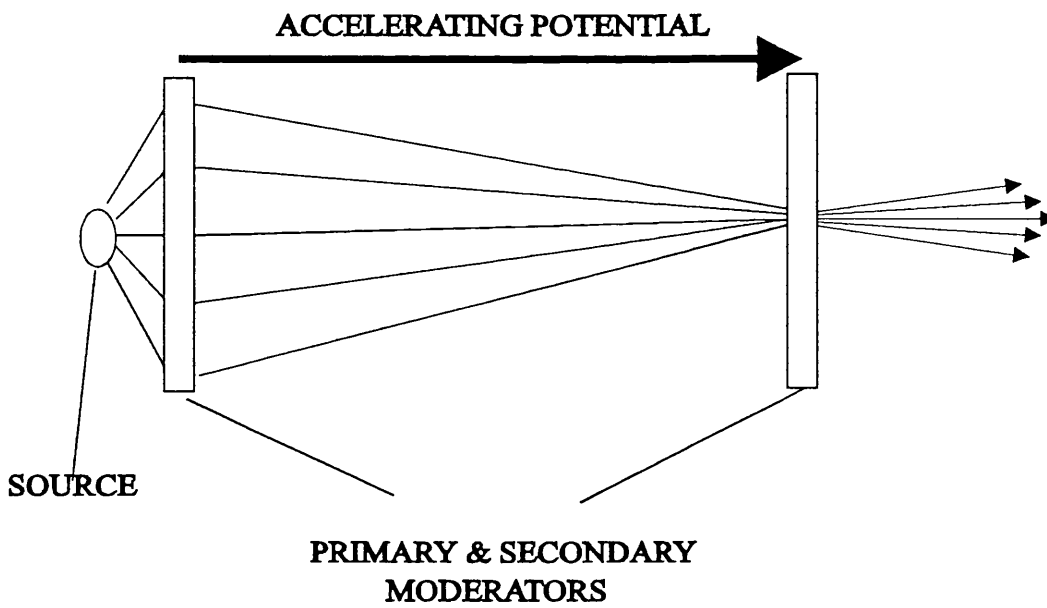
Figure 1.13 A schematic diagram depicting the process of brightness enhancement.

1.5 The Motivation for this Work

The simplest mode of slow positron transport is by magnetic confinement. Many experiments in the field of positron and positronium physics however, eg. differential scattering and atomic lifetime measurements, are made much simpler in an environment free of magnetic fields, in the case of the examples given, as angular information is preserved in the former and mixing of sub-states avoided in the latter. A high intensity electrostatic positron beam, operable at low 50-500eV transport energies, with a reasonable beam quality (divergence and cross-sectional area), is therefore a versatile tool, not only because systems may be studied in field free areas, but also as the performances of devices such as photomultiplier tubes and channel plate electron multipliers used in conjunction with positron beams, are not degraded by the magnetic fields present when magnetic transport is used.

The first aim of this work, discussed in chapter 2, was to design and construct an electrostatic positron beam as the experiments described later in this thesis required the use of a photomultiplier tube for the detection of the u-v photon emitted by the 2P-1S transition of excited positronium, Ps*. It was of primary concern that the timing resolution and gain of this device should be as high as possible and hence a magnetically guided positron beam, which would degrade both, could not be used.

Chapter 3 describes how this beam was then used to study the production of positronium in the first excited state, Ps*, by impacting positrons of various energies on a range of targets. Investigations were made into the conditions required for optimum production and the maximum yields obtainable under such conditions. In this area, little work has been performed and the formation process is still not well understood. In recent times, some controversy has arisen over the energy distribution and absolute yield of the Ps* formed and the rôle of surface conditions in the formation process, and further information in this area was badly needed.

Furnished with this information, chapter 4 describes an attempt to make the first measurement of a radiative lifetime of an excited state of positronium, in this case the 2P-

1S transition. Measurements of this kind are of great importance as they allow stringent tests to made of the models for leptonic interactions embodied in QED.

CHAPTER 2

THE ELECTROSTATIC BEAM

2.1 Introduction

Positrons are anti-electrons and therefore it is not surprising that electrostatic positron beams are not dissimilar to their electron counterparts. The main difference is scale. Electron beams typically have areas of one or less mm^2, in contrast to primary e^+-beams where cross-sectional areas at least tens of mm^2. Electron beam currents are of the order of several mA, whereas even the largest e^+-beam is many orders of magnitude less than this. Finally due to the small beam areas lens diameters are much smaller in the case of electrons, with the exception of brightness enhanced positron beam and, as background radiation is absent, may be much shorter.

A typical electrostatic e^+-beam is shown in fig.2.1. It can be seen to comprise of three main parts. A gun which consists of the slow positron source and extraction system, an electrostatic mirror, to select monoenergetic particles and to remove fast β^+ and γ-rays source from the line of sight of the detectors, and another simple lens, to transport the particles to an interaction region. More sophisticated e^+-beams, such as those used to make positron microscopes, may employ one or more re-moderation stages for brightness enhancement (eg. Ito *et al* (1992)).

2.2 Lens Design

There is a great deal of literature on the subject of lens design (eg. Klemperer and Barnett (1971)). Mostly consisting of tables of data for particular standardised parameters, known as cardinal points, selected to aid calculations and provide a database from which lens constructors may work. It should be noted however that this is only true for relatively simple lenses, and it is generally required that the beam at the input side of the lens is a compact source of particles on the axis. Fig.2.2 shows the design
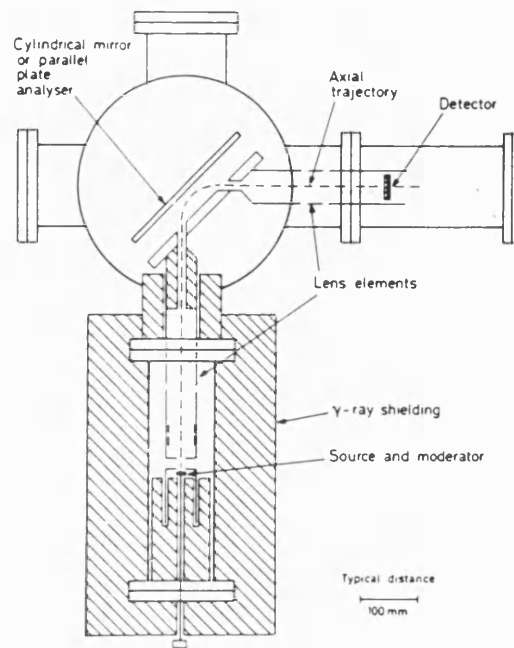
Figure 2.1 A typical electrostatically guided positron beam.

parameters pertinent to a typical lens. R is the reference plane of the lens, P and Q are the object and image distances respectively, f1 and f2 are the 'true' focal lengths of the lens which are measured relative to the principal planes, P1 and P2, and F1 and F2 are the mid-focal lengths measured with respect to the reference plane. Using the cardinal points one may determine the required lens given a particular set of circumstances, such as required linear or angular magnification and the initial and final particle energy. Each set of cardinal points are calculated by using the 'charge density' method (Read *et al* (1971)) to solve the Laplace equation in two dimensions, which describes the potential surface as seen by a charged particle. When the potential surface is known paraxial ray trajectories may be obtained by numerical integration and therefore cardinal points determined by imposing some boundary conditions.

In addition to the simple cardinal points, one may also determine the magnitude of the so-called aberration coefficients for that particular configuration. These aberrations arise from particles which have trajectories that take them off the axis, the closer a ray is to the axis,
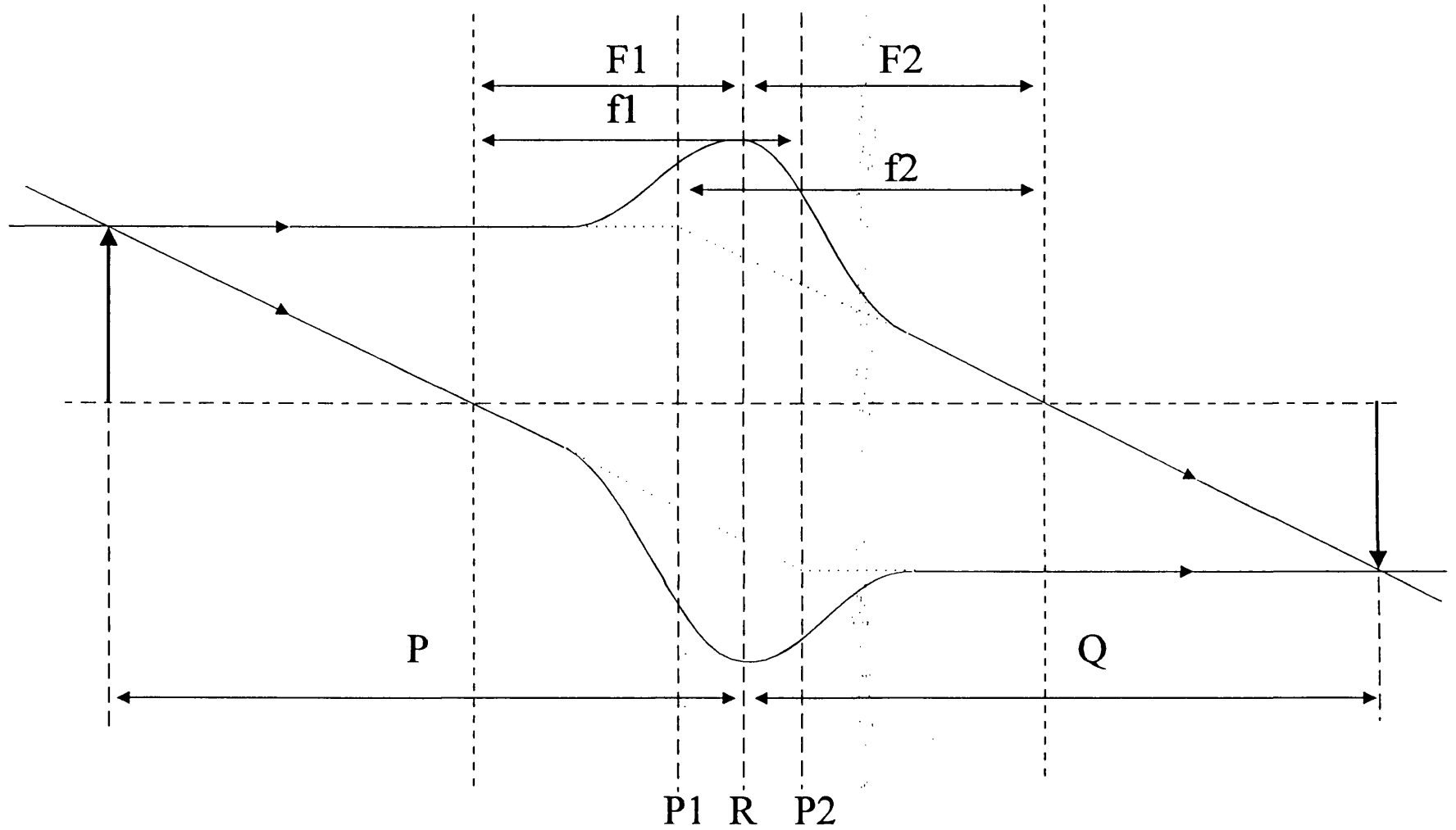
Figure 2.2 The design parameters of a simple electrostatic lens.

the less the aberration. Hence the 'filling factor' for a particular lens, ie. by how much the lens is filled by the beam, is important in the estimation of beam quality.

With the advent of powerful micro-computers, interactive programs have now become available that enable the designer to actually view the performance of an individual lens or composition of lenses and to make changes to the lens design or input ray trajectories at the touch of a key. As a result, lenses may be optimised within the program without resorting to actual construction or tedious incrementing of parameters. Such routines allow the experimenter to develop an intuitive feel for the effects of his or her actions, and thus assist in the development process.

All the lenses used in this beam were modelled using the SIMION PC/AT software (Dahl and Delmore (1987)). This software is a useful tool in the initial stages of design. However, translating from an idealised situation of zero magnetic and perfectly cylindrically symmetrical electric fields can lead to differences between the predicted and experimentally determined voltages required to optimise the beam, in addition to departures due the imperfect nature of the manufactured lens.

2.3 The Positron Gun and Einzel Lens

Modern e^--beams use heated hairpin filaments for their electron sources. These have small emitting areas, effectively point sources, and are sufficiently efficient for the experimenter to be highly selective in terms of angle of emission and energy spread of his or her beam. Electron currents are typically several mA from these sources, to the extent that they are space charge limited. The commonly used Pierce gun is designed to overcome this space charge effect, however this gun is not used in positron beams as fluxes are so low. The spatial extent of positron moderators is quite unlike the 'point-source' filament. In fact, the positron moderator bears a strong similarity to the earlier heated metal oxide discs used as electron sources by Soa (1950), and hence the primary element of most positron beams is a 'Soa type' gun.

The Soa gun used in this beam was a *modified* Soa gun after Canter *et al* (1986) and is

depicted in fig.2.3. It consists of the positron moderator, or cathode (The convention is to retain the nomenclature used with electrons even though the polarity of these elements in the e^+ case is the opposite.), a grid electrode, a Wehnelt electrode, a Soa tube and an anode. Together they form an immersion lens, so called as the object is an integral part of the lens.

The advantage of the modified Soa gun is that the addition of a 'Soa tube' allows the positrons emitted at large angles, or small angles and large energies, to fill the lens to a greater degree and still be focused and thus retained in the beam, whereas the conventional Soa gun would tend to attenuate these particles at the anode.

The overall dimensions of the electrostatic beam was largely determined by the moderator size and source strength. The former influences the diameter of the lenses and hence the μ-metal shielding and vacuum chamber, the latter the minimum distance permissible to shield scattered radiation from the interaction region. For this beam, the distance from source to the input of the CMA had to be of the order of 220mm and all of the elements have small internal diameters and are constructed from stainless steel to provide shielding against radiations from the source. The slow positron source consisted of a 100mCi ^{58}Co source in the form of a 3mm spot on a thin rhenium disc 10mm in diameter. It was separated by a 0.5mm thick PTFE washer from four pieces of annealed 60% transmission tungsten mesh which served as the moderator, the optimum number as determined by Zafar *et al* (1990). The source and moderator were mounted in a stainless steel cap, shown in fig.2.4, electrically isolated by a 0.5mm PTFE washer. The cap was tapered and located flush with the surface of the grid electrode making electrical contact. The shaping of the cap allowed it to be accurately positioned remotely via a linear manipulator to which it was attached. The cap aperture was 10mm in diameter and covered in a 95% transmission copper mesh. It was possible for the source, moderator and grid to each be held at different potentials to enhance extraction of the moderated positrons and to return positrons re-emitted towards the source back to the moderator.

The internal diameters of the Wehnelt, anode and 3-element lens elements were 19mm. The length of the Wehnelt electrode was 9.5mm and the Soa tube 34mm. The tube was

49
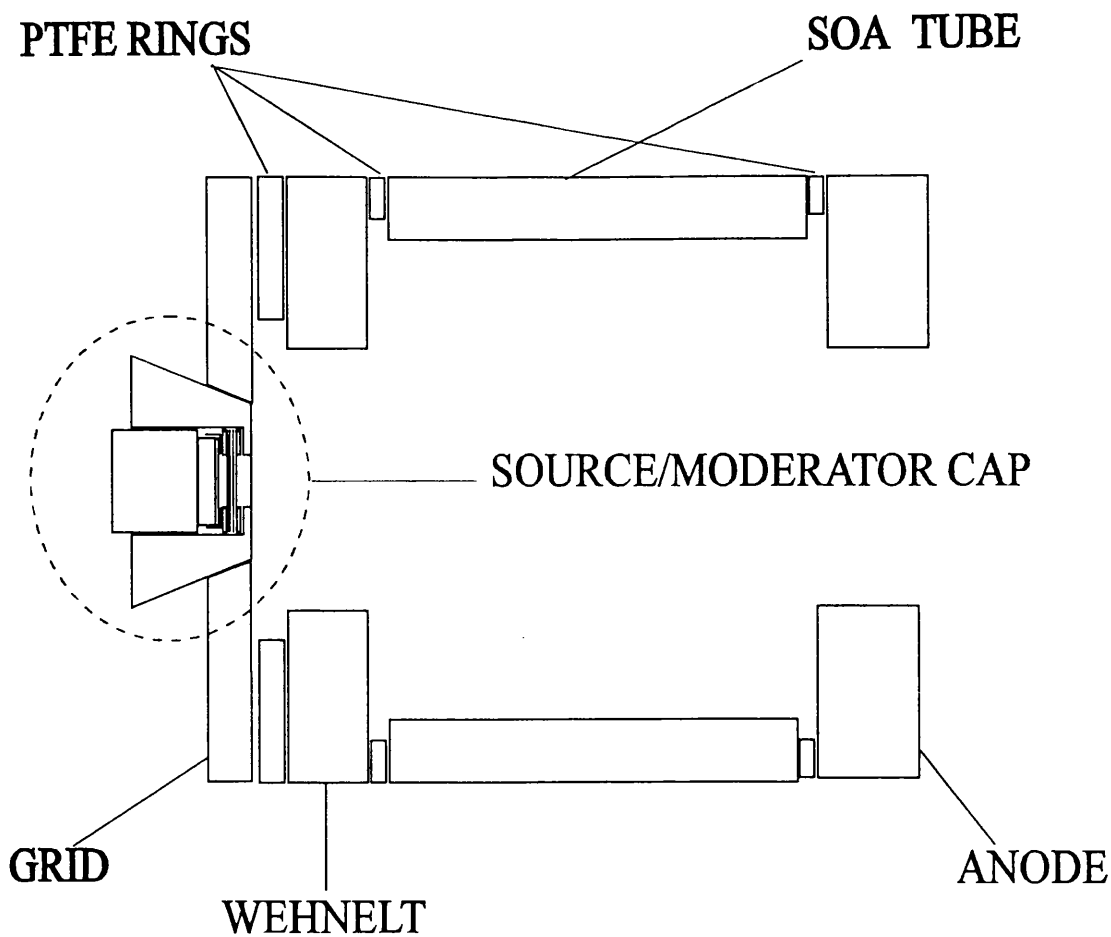
Figure 2.3 A schematic diagram of the modified Soa gun.
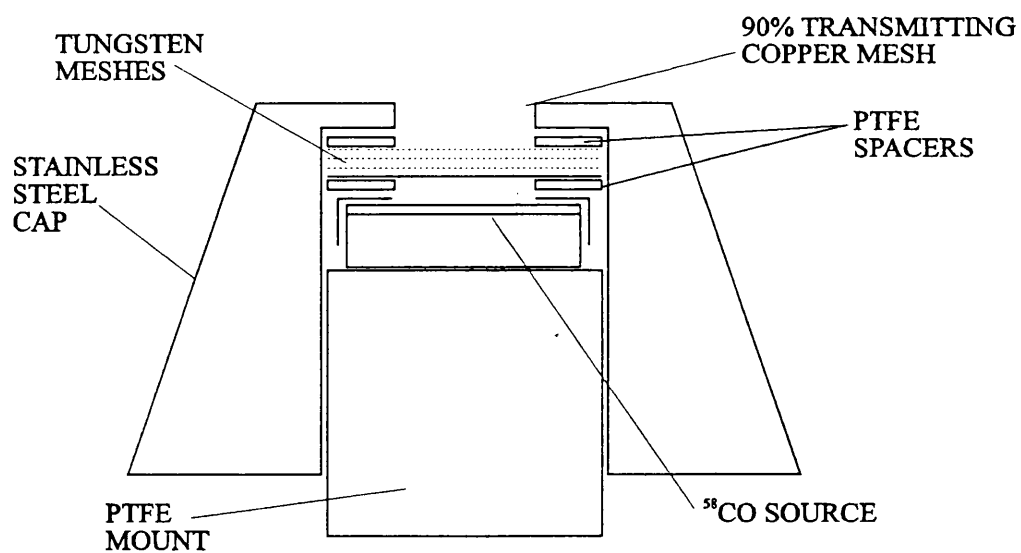
Figure 2.4 A schematic diagram of the source/moderator cap.

50
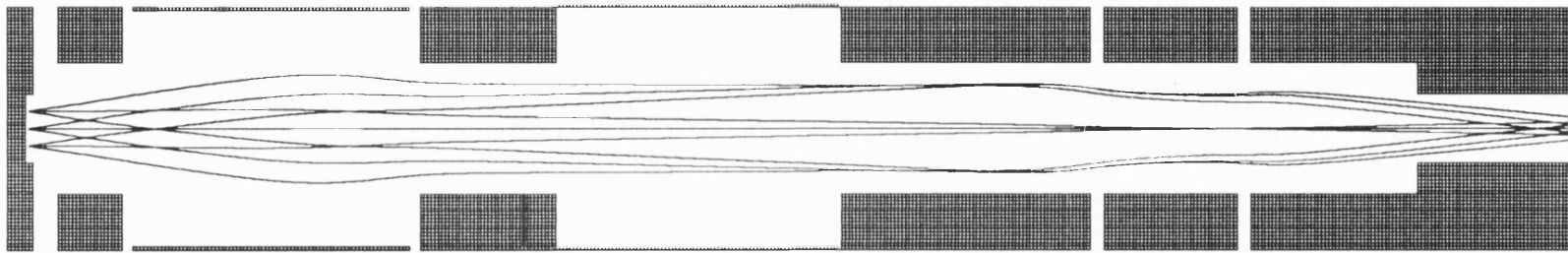
Figure 2.5 A SIMION simulation of the Soa gun and 3-element lens operating at 100eV, for positrons at 0° and 10° to the beam axis.

separated from the anode and the Wehnelt electrodes by 2mm thick PTFE rings and had an internal diameter of 35mm. The separation between the grid and Wehnelt electrodes was 4.5mm and effected by a PTFE ring.

An einzel lens is the electrostatic analogue of a simple bi-convex lens in optics. It consists of three elements two of which are held at the same potential, ie. $V_1 = V_3$ (It should be noted that these potentials are with respect to the cathode potential.). The central element is used to adjust the focal length of the lens (Adams et al, 1972). For certain particle energies and V_2 combinations, $P = Q$ and therefore $M = M_\alpha = 1$, in this case the lens preserves the input characteristics of the beam. It is for this reason that lenses of this kind are used for simple transportation away from the particle source, either singly or in a series. For this particular beam only one stage of transport was used after the Soa gun to avoid compounding aberrations.

The element forming the anode and first section of the 3-element lens was 94mm in length. The central element 17mm and the third 44mm. The final element was shaped to fit into the input of the CMA and internal diameter at the CMA was reduced to that of the beam, approximately 10mm. All components of the 3-element lens were again isolated with 2mm thick PTFE rings. Fig.2.5 is a computer simulation of the Soa gun and 3-element lens operating at 100eV.

2.4 The Cylindrical Mirror Analyser

Cylindrical mirror analysers, CMAs, are often used by ion/electron spectroscopists to energy analyse scattered particles. Here the CMA is used purely to remove fast β^+-particles and γ-rays from the line of sight of the detectors. The following discussion on CMA design and performance draws on the work of Risley (1972).

In its simplest form, a mirror analyser consists of just two parallel plates one held at ground with respect to the cathode potential and the other at a repulsive voltage sufficiently high to ensure that a particle entering the analyser follows a trajectory to the output.
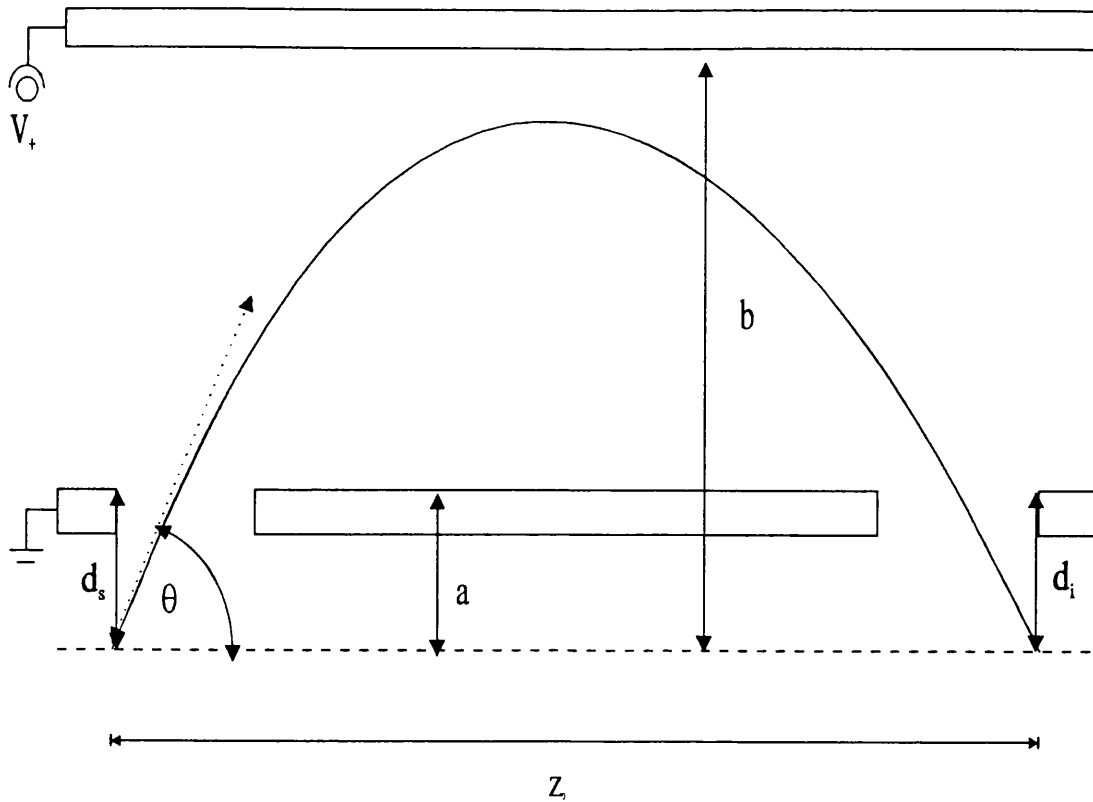
Figure 2.6 The parameters of interest when designing a CMA.

However, the transport efficiency of a parallel plate analyser is rather poor. This is because particles entering the analyser with an azimuthal angle not equal to zero are unlikely to be focused to the output and hence aberrations are large. A cylindrical mirror analyser is more suitable for divergent beams as its cylindrical symmetry ensures that all particles passing through the CMA axis will be returned to that axis.

Of primary interest when considering CMAs are the focal length, z_0, the object/image distance from the entrance/exit aperture, d_s and d_i respectively, and finally the inner cylinder and outer cylinder radii, a and b, as shown in fig.2.6.

The voltage difference, V_+, depends on the particle energy, in this case the outer cylinder is held at a positive potential and the inner cylinder is grounded. The geometry of the CMA ensures that only the radial component of the particle's kinetic energy is analysed and so V_+ will always be less than the incident particle energy, E. For a particular CMA z_0 is given by

$$z_0 = (d_s + d_i) \cot\theta + 4ak^{1/2}\cos\theta e^{k\sin^2\theta} \int_0^{\sqrt{k}\sin\theta} e^{-u^2}du \qquad (2.1)$$

where $k = (E/V_+)\ln(b/a)$ and θ is the angle made by the particle trajectory to the axis of the CMA.

The energy resolution of a CMA, is approximately proportional to the dispersion, D, of that analyser, where the dispersion is given by

$$D = E\frac{\delta z}{\delta E} \qquad (2.2)$$

D may obtained by expanding z_0 in a Taylor series about a variation in energy, ΔE, and angle, $\Delta\theta$. For $\Delta\theta = \theta - \theta_0$ and $\Delta E = E - E_0$,

$$z = z_0 + \sum_{n=1}^{\infty} \frac{1}{n!}\left(\Delta\theta\frac{\delta}{\delta\theta} + \Delta E\frac{\delta}{\delta E}\right)^n z(\theta,E)\Bigg|_{\theta=\theta_0,\ E=E_0} \qquad (2.3)$$

$\therefore$

$$z = z_0 + \sum_{i=1}^{\infty} \frac{1}{i!}\frac{\delta^i z}{\delta\theta^i}\Bigg|_{z_0}(\Delta\theta)^i + \sum_{j=1}^{\infty} \frac{1}{j!}\frac{\delta^j z}{\delta E^j}\Bigg|_{z_0}(\Delta E)^j + \sum_{i,j=1}^{\infty} \frac{c_{i,j}}{(i+j)!}\frac{\delta^{i+j}z}{\delta\theta^i\delta E^j}\Bigg|_{z_0}(\Delta\theta)^i(\Delta E)^j \qquad (2.4)$$

where c_{ij} is the binomial expansion coefficient. The first series in the expansion corresponds to the degradation in resolution due to particles with a spread in entrance angle. If the first partial derivative is zero then the analyser is said to exhibit first order focusing. Peculiar to CMA's is that second order focusing is also possible for certain combinations of the CMA's geometrical parameters, ie.

$$\frac{\delta z}{\delta\theta} = \frac{\delta^2 z}{\delta\theta^2} = 0 \qquad (2.5)$$

for which the CMA is least sensitive to angular spread at the source and therefore transmission is at a maximum. Conditions for second order focusing are rather restrictive. For any given value of $d_s + d_i$ the beam must enter the analyser about a fixed angle and at a fixed z_0. Tables (see table 2.1) of these conditions are available, and so it is possible

to select an analyser to suit particular experimental requirements.

Table 2.1 Design parameters for a selected range of analysers with second order focusing, after Risley (1972). Parameters used for this work are in italics. All lengths are in units of the inner radius, a.

d	θ(deg)	$(b/a)^{E/V+}$	z_0	$\delta^3 z/\delta\theta^3$(a/rad^3)	D
0.01	30.164	1.0199	0.0516	-0.9444	0.0345
0.50	35.723	1.8643	2.0585	-30.4912	1.5616
1.00	38.825	2.5569	3.6022	-52.2275	2.9675
2.00	*42.307*	*3.7054*	*6.1298*	*-93.1776*	*5.6038*
5.00	46.799	6.4277	12.1716	-215.7336	12.9865
10.00	49.846	10.1228	20.5373	-424.3391	24.6942
50.00	55.597	32.4104	72.9434	-2208.5996	114.2443

The actual dimensions of the CMA depend on experimental considerations. If the CMA is to be used purely as a background filter, to ensure the preservation of beam parameters at the output the d=2a configuration must be chosen where $d_s=d_i=a$ (in italics table 2.1). This corresponds to the object and image both lying the same distance from the CMA axis, or simple reflection. The inner radius a, is chosen to suit the beam size and all other dimensions scale accordingly. The outer cylinder radius is chosen to satisfy space requirements. For a given choice of d, a and b the focal length z_0 may be deduced. It should be noted that z_0 is independent of beam energy for the correct value of V_+ which may be found from col.3. Col.5, the 3rd order partial derivative, is a measure of the aberrations due to angular deviation from θ. The complete expression being

$$\Delta z(\Delta\theta) = \sum_{i=1}^{\infty} \frac{1}{i!} \left.\frac{\delta^i z}{\delta\theta^i}\right|_{z_0} (\Delta\theta)^i \qquad (2.6)$$
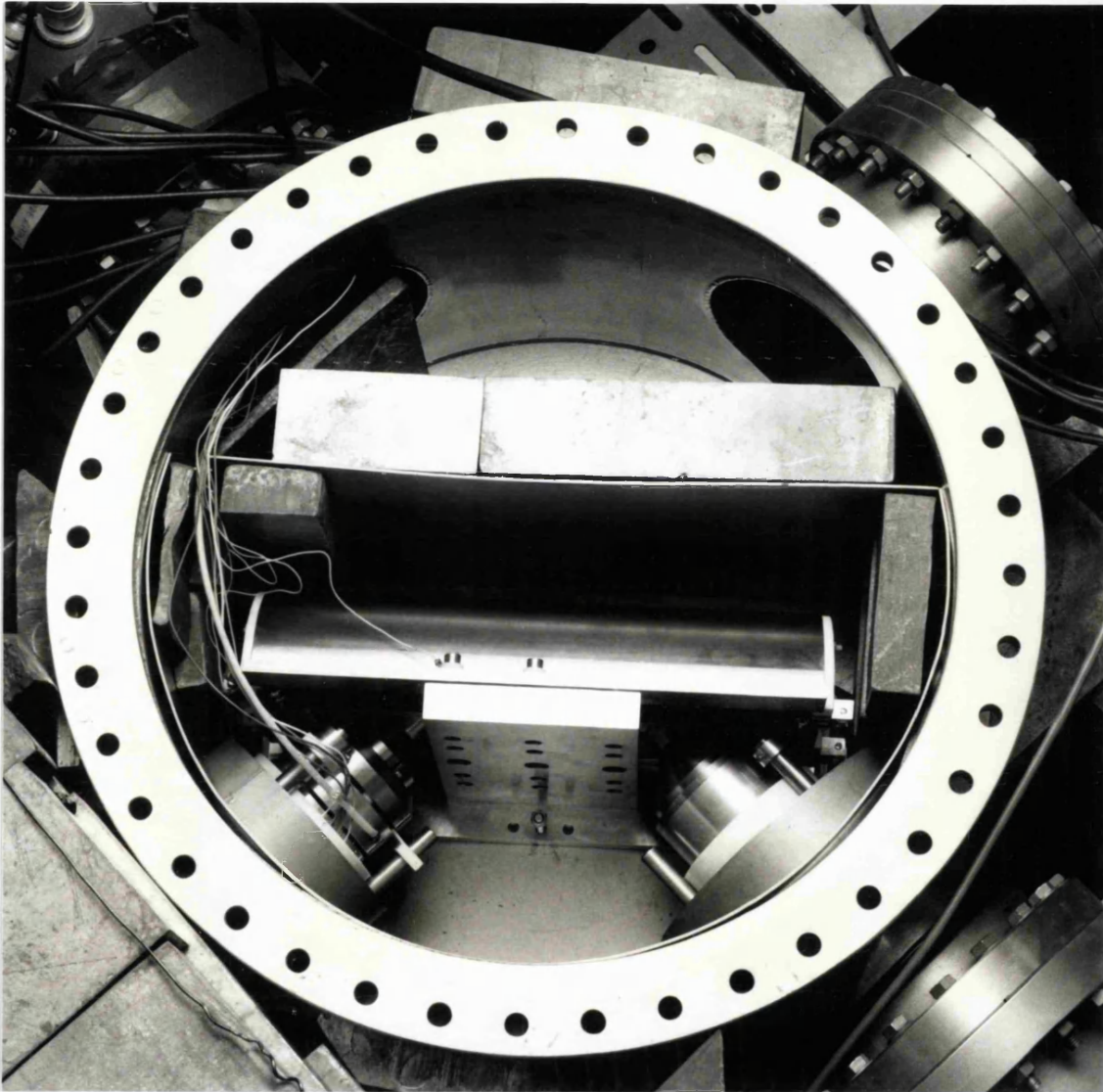
Figure 2.7 A photograph of the CMA, with the input and output lens stacks clearly in view.

In Col.6 the parameter D is the dispersion of the analyser. For beams with an intrinsic energy spread (such as e^+-beams from the moderator), it is preferable to have a low value for D for maximum transmission.

The electrostatic field inside an ideal CMA will fall off logarithmically. 'Ideal' in this context means of infinite length. In practice, the field near the ends of the CMA will not be logarithmic. If the entrance and exit apertures are located away from the ends then there is little degradation in performance, however for long focal length analysers this is not always possible. It is therefore necessary in some cases to locate semi-circular electrodes, with suitable radii, at the ends of the analyser and held at the potentials expected in a purely logarithmic field, and thus some improvement in performance transmission can be achieved.

In this beam the CMA was constructed from stainless steel. The inner radius was 20mm and outer radius 60mm. The inner element was formed from a solid semi-cylindrical rod. The outer element was constructed from half of a tube with the appropriate internal diameter. Both elements were attached to an upright post and electrically isolated from the same by ceramic rods. Situated at the ends of the analyser were copper guard rings with radii of m, m and 50mm held in a PTFE former. These electrodes also returned across the vertical plane of the analyser to further reduce field distortion and can just be seen in fig.2.7, which is a photograph of the analyser. The openness of the CMA was designed to enhance pumping.

The focal length of the analyser was 122.6mm, as calculated using the tables of Risley (1972), and the overall length of the analyser, 240mm. The entrance and exit apertures were 10mm in diameter and are covered with 95% transmission copper mesh to prevent any lensing by field distortion. The effect of this can be clearly seen by comparing fig.2.8 (top) and (bottom) which are computer simulations with (top) and without (bottom) meshes at 100eV. The front of the CMA, the last element of the 3-element and first of the 4-element lenses were in electrical contact and all three were earthed.
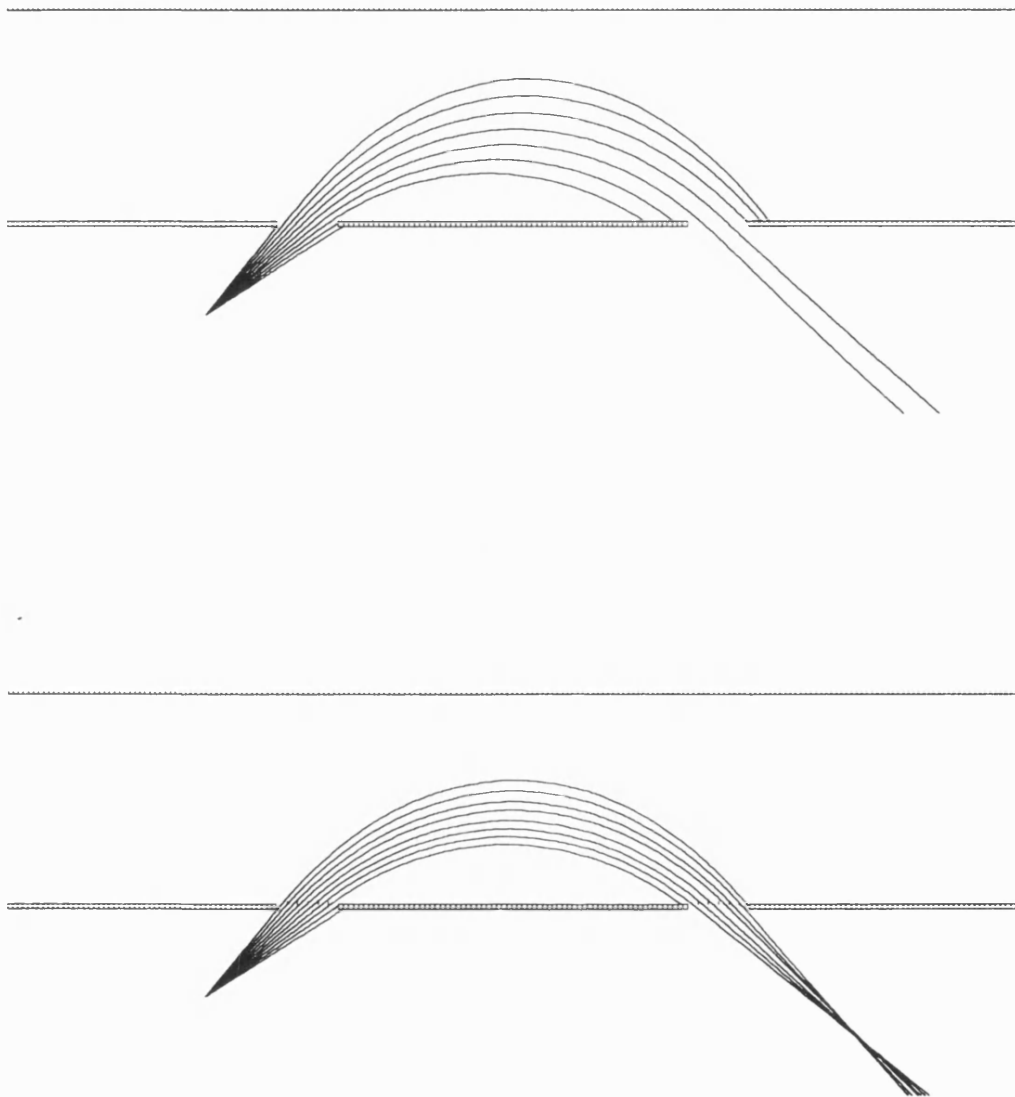
Figure 2.8 SIMION simulation of the CMA operating at 100eV, for positrons with divergences of up to ±10° from the 'magic angle' (in steps of 2°). Without meshes over the input and output (top), and with meshes in place (bottom).

This was to simplify the arrangements required to float the various elements as fewer were held above ground in this way.

2.5 The Four-Element Lens

As discussed, the properties of any lens may be described in terms familiar in linear optics: focal length, linear and angular magnification. An extra parameter of interest to electrostatic beams is the final energy of the particles. To have total control of the particle trajectories, all four of these properties must be modified simultaneously. This is impossible as Liouville's theorem states that phase space is conserved. It is possible, however, to select three of these parameters. To do this one requires at least one more degree of freedom, in this case lens voltage ratios, than selected parameters. Therefore in the final stage of this beam a four-element lens was used.

The overall length of the 4-element lens was 330mm and the internal diameter of all elements 58mm. The first element was shaped to fit into the exit aperture of the CMA and 133.1mm long. The two central elements were 23.2mm long and separated from each other and the first and last components by PTFE spacers 5.8mm thick. The final component was again 133.1mm long. All the elements were constructed in aluminium. The final element was terminated with an end-cap 6mm thick with a 15mm diameter aperture located on the beam axis. The end-cap could be removed to facilitate larger apertures to suit experimental requirements. A SIMION simulation of the four-element lens operating at 100eV is shown in fig.2.9.

2.6 Lens Voltage Requirements

For the purposes of later experiments it was preferable to keep the target held at ground. Therefore all the gun elements were held at some positive potential, as were all the CMA potentials, with the exception of the inner cylinder which was also grounded. The active components in the three and four element lenses were held negative. The beam in general
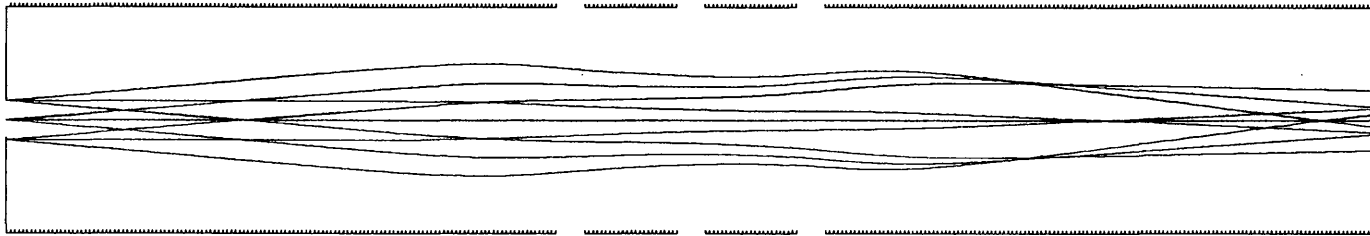
Figure 2.9 A SIMION simulation of the 4-element lens operating at 100eV, for positrons at 0° and 10° to the beam axis.

was operated at 100eV. It was found that no potential was required to be above 500V and so it was a simple matter to construct potential dividers to deliver the correct voltages. As the various elements required both positive and negative voltages, for simplicity two divider networks were built one for each set of elements. Ten-turn potentiometers were used to control the voltages to the Soa gun as it was found that it was to these that the beam was most sensitive. Single turn potentiometers were used for all other lens voltages.

2.7 Lens Mounting

All the cylindrical lenses had an exterior diameter of 70mm and were restrained axially by three stainless steel rods which passed through two annuli situated approximately 400mm apart and at 120° intervals. Each element was encircled with a PTFE band 8mm thick and 14mm long to ensure electrical isolation from the supports and to maintain alignment as shown in fig.2.10. Each annulus had an adjustable screw on its outside edge, again at 120° intervals which were in contact with the surrounding μ-metal shielding, thus facilitating further corrections to alignment of both input and output lenses with respect to the CMA.

2.8 The Vacuum Chamber

The vacuum chamber consisted of a stainless steel cylindrical tank of 400mm internal diameter and 203mm depth. Four 200mm flanges were mounted at the end of 80mm extension tubes at 90° intervals around the tank circumference. These flanges were used to feed through lens voltages, accept the input and output lens stacks and to provide an observation port, not normally used, and are depicted in fig.2.11. The tank interior was accessed by the removal of a 480mm diameter 25mm thick stainless steel blank designed to make an indium seal with a corresponding flange attached to the tank itself. However it was found that by using an aluminium former and a suitable Viton gasket the weight of the blank alone would make a vacuum tight and reusable seal. A 440mm long, 114mm diameter stainless steel tube was connected to one of the four flanges and a 150mm

PTFE RING

LENS

ALUMINIUM
ANNULUS
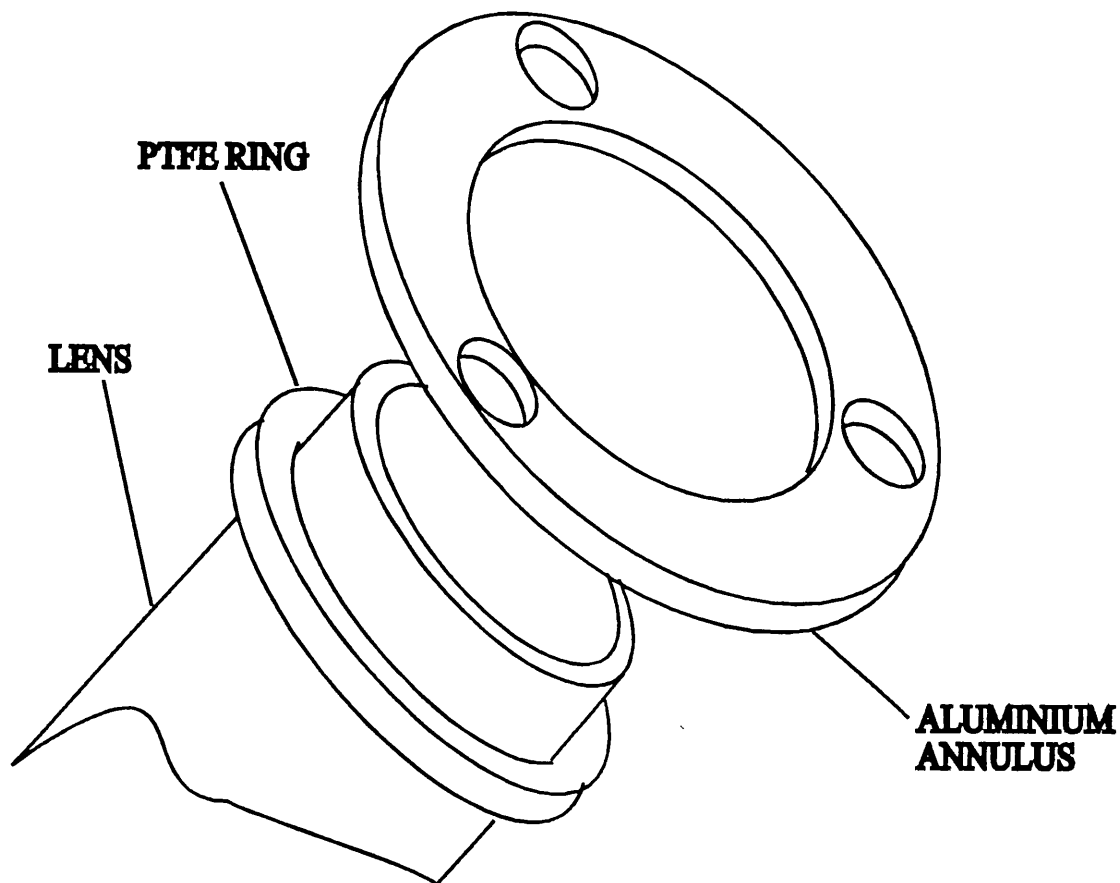
Figure 2.10 A schematic diagram of the lens mount, with tripod omitted for clarity.

internal diameter six-way cross to a flange at 90° to it. Inside the tube was situated the input lens stack and in the six-way cross the output lenses. The reduced tube diameter was chosen to allow additional shielding to be placed around the source. A semi-cylindrical μ-metal container, with lid, occupied half of the tank. There were two holes on the circumference, set at 90° apart, to accept μ-metal tubes surrounding the input and output lens stacks.

Both diffusion pumps were connected to an Edwards ED50 rotary pump via a magnetic valve held open during normal operation but which would close in the event of the pressure rising above 0.1 Torr in the backing line as measured by a Pirani gauge. In addition the supply to the channel-plate electron multiplier arrays (CEMA) and both diffusion pumps would shut down also.

The pressure in the main chamber was measured with a Vacuum Generators IGC11 naked Bayard-Alpert ionisation gauge situated close to the six-way cross, where the

LEAD
SHIELDING

DIFFUSION
PUMPS

μ–METAL
SHIELDING

WELL

IONISATION GAUGE

MANIPULATORS
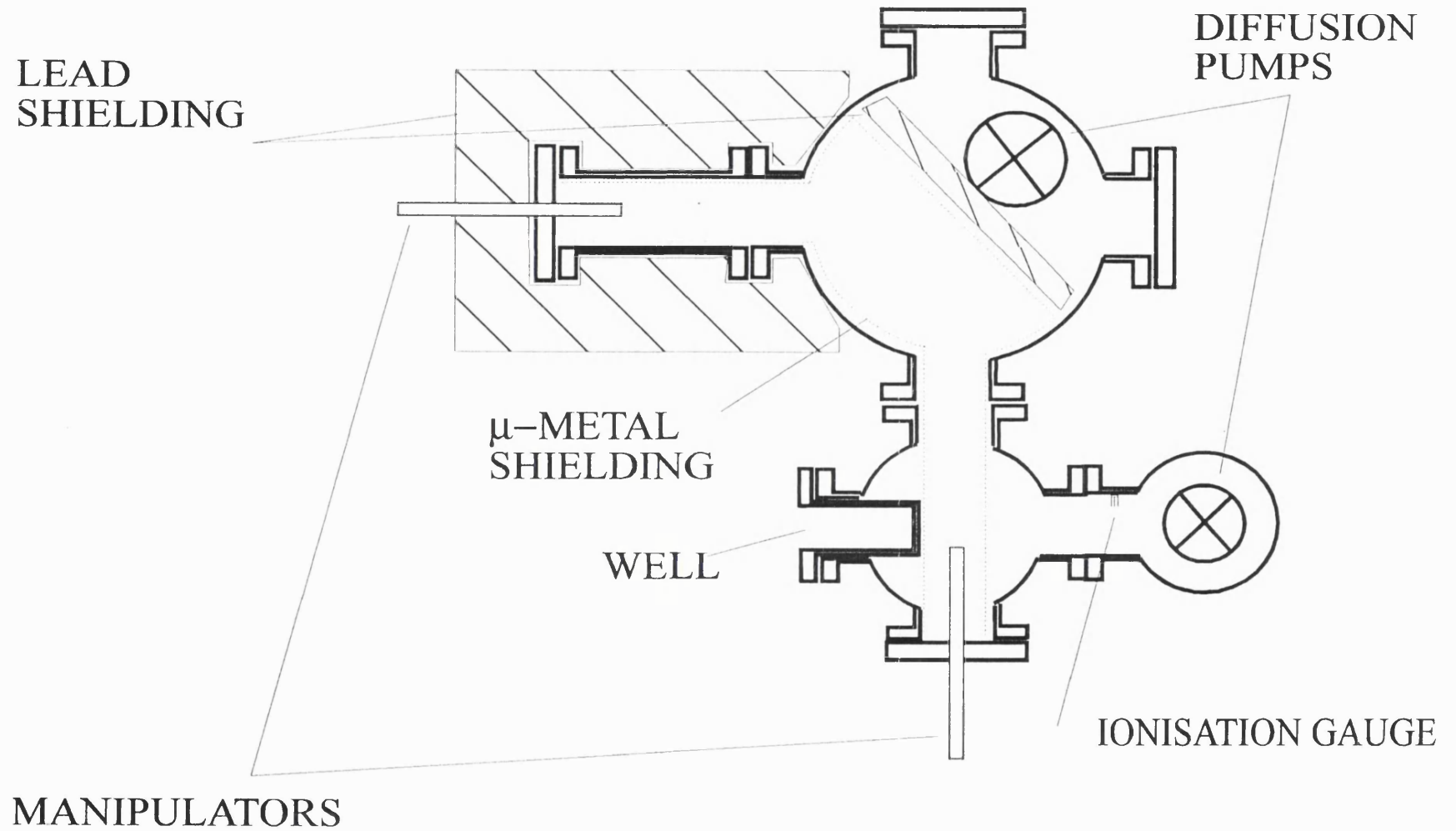
Figure 2.11 A schematic plan view of the vacuum chamber and lead shielding.

channel plate electron multipliers, CEMAs, were positioned. During normal operation a pressure of 1×10^{-6} torr was maintained with further improvement to 2×10^{-7} torr on the introduction of liquid nitrogen to the cold traps.

2.9 The Detectors and Electronics

The positrons were detected by two Varian VUW8946ZS CEMAs which on positron impact produce secondary electrons which are then multiplied and collected thus producing a negative pulse which may then be processed electronically.

The plates were made of Pb glass 25mm in diameter and 0.42mm thick, perforated by an array 18mm in diameter of 9.8μm cylindrical channels, internally coated with a semi-conducting material with a high secondary electron coefficient. The channels were pitched at 10° to the normal to ensure that an incident particle strikes the walls of a channel. One plate on its own with a potential difference of 1kV between its surfaces has a reported gain of 4×10^4. By arranging two such plates with their channels aligned at 180° forming a chevron ensured a gain of $\sim 10^8$ with an overall potential between the plates of 2kV and a further 100V or so was applied between the back of the second plate and the collector. The plates were held in a cylindrical PTFE block as shown in fig.2.12, machined so that they sat on a ridge and were separated from the back of the block by 3mm.

The back of the block was coated with silver-loaded epoxy adhesive and acted as a collector, the potential to the channel plates themselves were effected by thin annular copper electrodes in contact with the front of the first plate and the back of the second. The whole arrangement was mounted on a PTFE frame, shown in fig.2.13, and which could slide along the beam axis to accommodate extra lens elements or devices.

The output was generated across a 10MΩ resistor and extracted through a decoupling capacitor. In the event of a high current occurring, possibly due to a pressure rise in the system and subsequent increase in the strip current or a short to ground, the 10MΩ
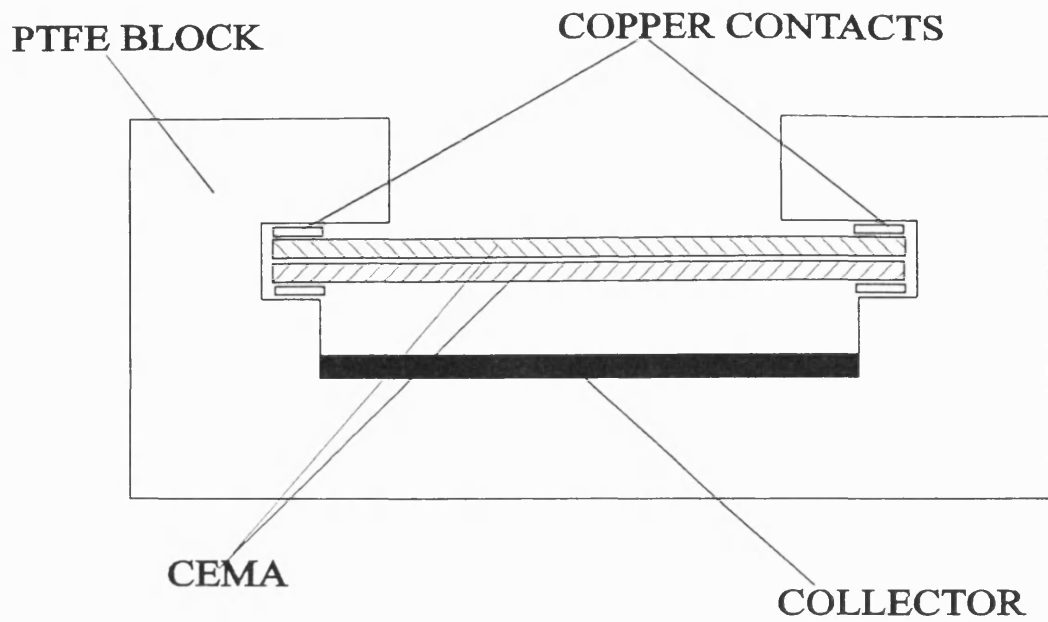
Figure 2.12 A schematic diagram of the CEMA holder.
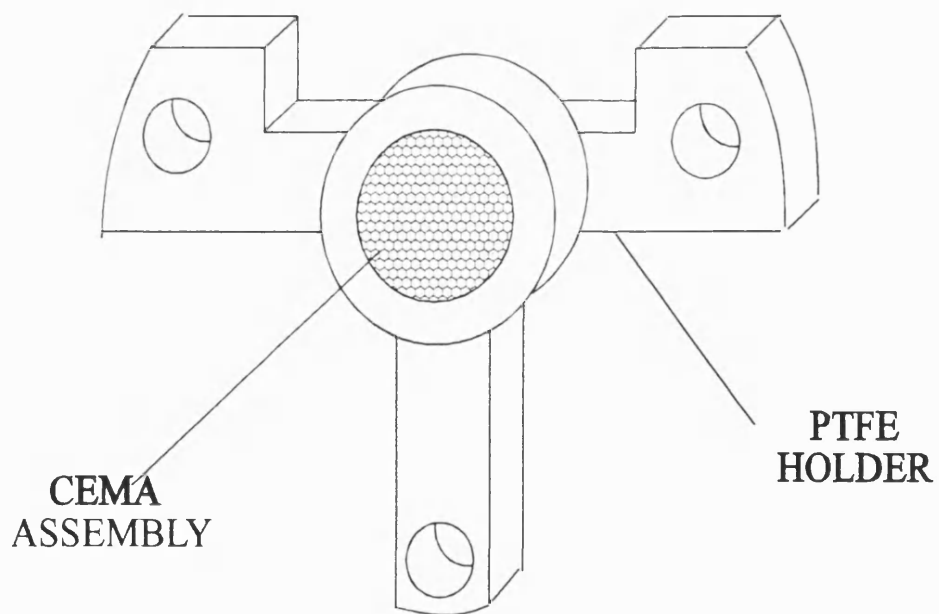
Figure 2.13 The CEMA arrangement and mount.

NaI DECTECTOR

LAST LENS
ELEMENT

CEMA
ASSEMBLY

BEAM AXIS
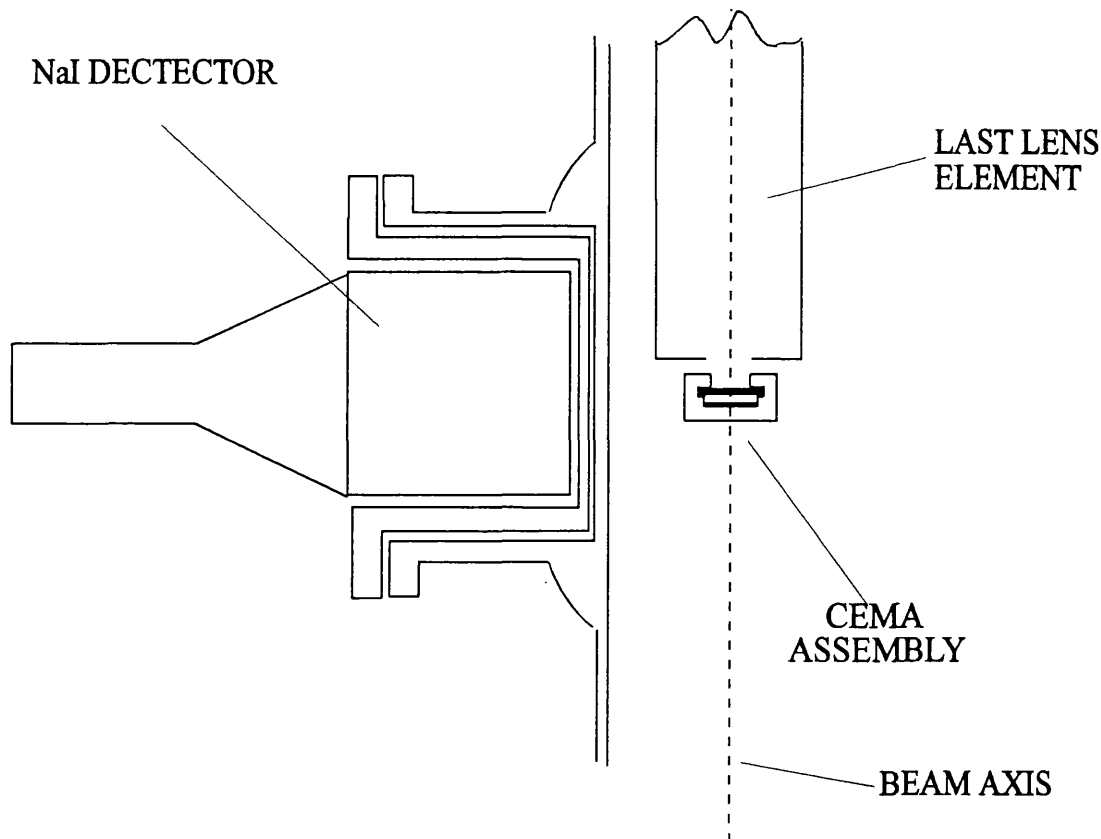
Figure 2.14 A schematic diagram of the detector arrangement used to determine
the CEMA detection efficiency.

resistor would fuse thus protecting the plates and further electronics. In this way, pulses
of -10mV or greater were obtained which after amplification by a ×10 fast pre-amplifier
could be fed into an Ortec 463 Constant Fraction Discriminator and counted using an
Ortec 994 Dual Counter Timer.

The plate detection efficiency for positrons was estimated by monitoring the single count
rates of the CEMA's and a NaI detector placed against the chamber as shown in fig.2.14.
The output signal from the NaI detector was fed through an Ortec 474 Constant Fraction
Discriminator (CFD). Both signals were fed into an Ortec 473A Time to Pulse Height
Converter and the number of coincidences noted with the beam on and off. Fig.2.15 is
a block diagram of the electronics used.

START   STOP

CEMA
(POSITRONS)

NaI
(γ-RAYS)

PRE-AMPLIFIER

TIMING
FILTER
AMPLIFIER

CONSTANT
FRACTION
DISCRIMINATOR

CONSTANT
FRACTION
DISCRIMINATOR

TIME TO
PULSE HEIGHT
CONVERTER

MULTICHANNEL
ANALYSER
AND
COMPUTER
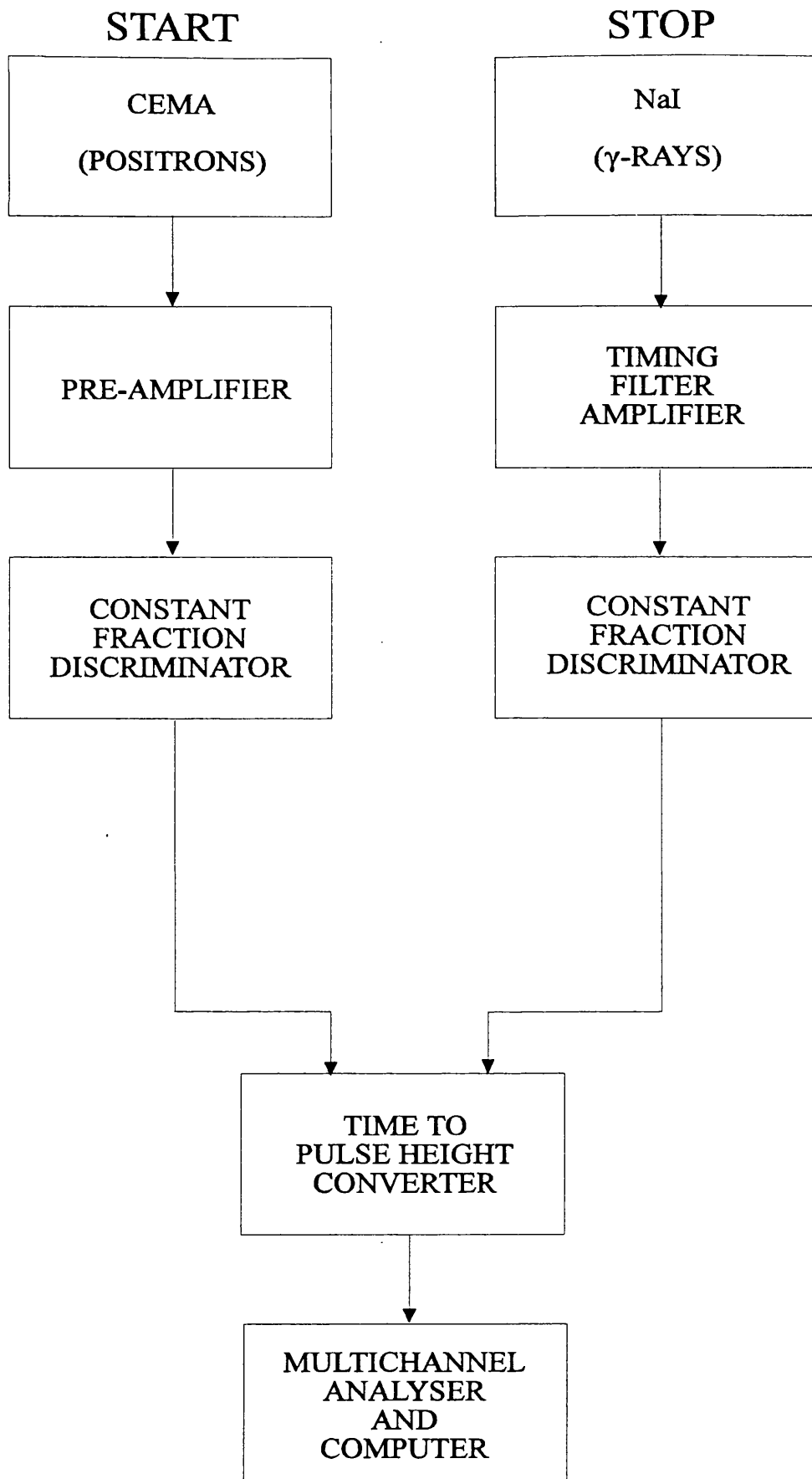
Figure 2.15 A block diagram of the timing electronics used to determine the CEMA detection efficiency.

With this information it is simple matter to calculate the detector efficiency and total beam intensity using

$$N_{plates} = N_{total} \times \epsilon_{plates} \qquad (2.7)$$

$$N_{NaI} = N_{total} \times \epsilon_{NaI} \qquad (2.8)$$

$$N_{coin} = N_{total} \times \epsilon_{NaI} \times \epsilon_{plates} \qquad (2.9)$$

$$\therefore$$

$$N_{total} = \frac{N_{plates} \times N_{NaI}}{N_{coin}} \qquad (2.10)$$

Where N_x is the singles count rate of a given detector or the total number of coincidences and ϵ_x is the detector efficiency. The potential of the first plate was varied to note the effect on the channel plate detection efficiency, which was found to be $\sim 20\%$ for 100eV positrons when the first plate was grounded, and $\sim 50\%$ when held at 100V.

2.10 The Beam Performance

Using the SIMION PC/AT software package as a guide, it was found that to transport positrons at a fixed energy of 100eV with respect to the target the following voltages, shown in table 2.2, were required.

It can be seen that, although there is some discrepancy between the predicted and measured voltages, the simulation does give some assistance in selecting the range in which to start when optimising a beam.

Table 2.2 The predicted and measured voltage values required to optimise the electrostatic beam.

	Source	Mod/Cath	Grid	Wehnelt	Soa Tube	1st 3-el
SIMION	-----------	100V	97.1V	88.1V	87.4V	-200V
EXPT	125V	100V	90.9V	97.1V	84.6V	-125V
	CMA B	CMA50	CMA40	CMA30	1st 4-el	2nd 4-el
SIMION	83.9V	70.0V	52.9V	30.9V	-275V	-450V
EXPT	86.4V	72.1V	54.5V	31.9V	-260V	-500

When optimised it was estimated that at 100eV approximately 170,000e$^+$s^{-1} were delivered to the target region with an assumed energy spread of around 3eV due to moderator. The diameter of the beam was estimated to be 10mm or less, the diameter of the exit aperture in the end-cap of the 4-element lens. The beam may be operated at energies above and below 100eV by simply scaling the lens voltages, ie. the ratios remain the same. Fig.2.16 is the measured relative transport efficiency as a function of energy for positrons from 50eV to 250eV. However, below 50eV, serious losses to beam flux are encountered. At low energies, any transverse component of velocity that the positron acquires at emission becomes significant as the emission angle increases, as Lagrange's law states

$$\theta_{1/2} = \frac{1}{M}\sqrt{\frac{\Delta V}{V}}$$

(2.11)

Where M is the magnification, and ΔV is the kinetic energy transverse to direction of the accelerating potential, V. If one assumes that the average emission angle at the moderator is 45° at a kinetic energy equal to the positron workfunction ($\approx$ 3eV), then for a 100eV beam with M=1, the maximum pencil half angle, $\theta_{1/2}$ at the anode will be of the order of 10°. At 25eV, however, this angle increases to 20° and serious losses occur in the next stage of transport.
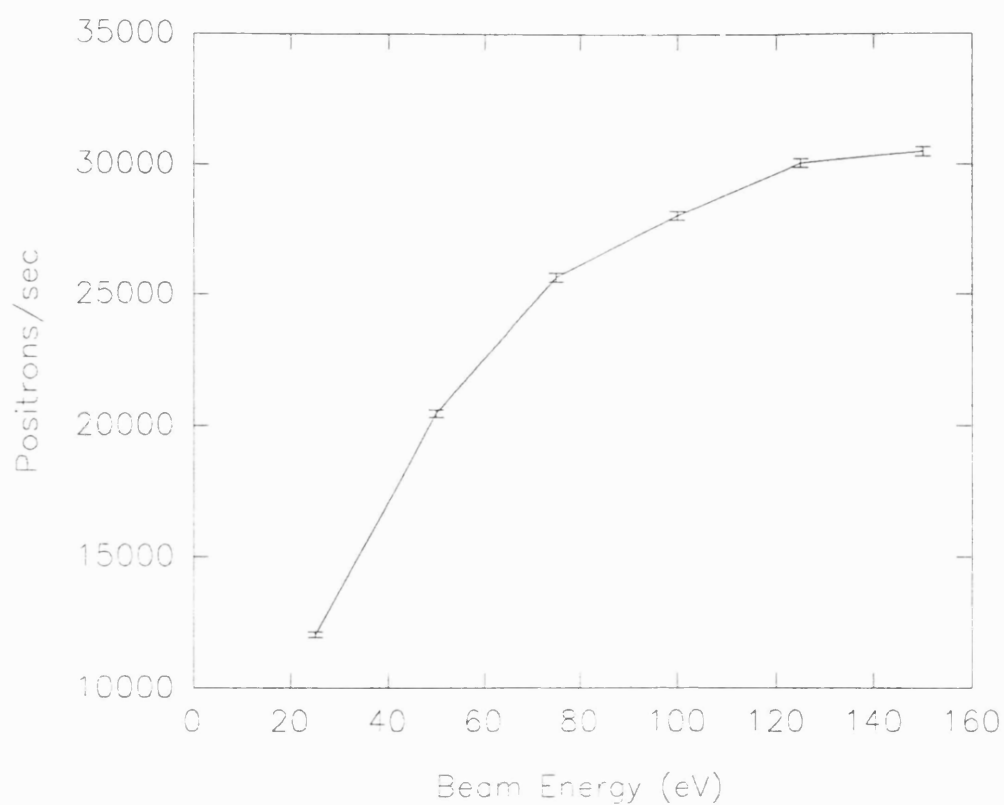
Figure 2.16 The relative intensity of the electrostatic positron beam as a function of transport energy.

For the experiments described in later chapters the electrostatic beam was operated at 100eV, thus ensuring that the positron flux reaching the interaction region was constant, apart from the expected reduction in time due to source decay. Any modification in the incident positron energy was made by biasing the target region itself.

CHAPTER 3

THE PRODUCTION OF EXCITED STATE POSITRONIUM
FROM SURFACES

3.1 Introduction

In this chapter an experiment designed to examine the production of excited postronium from surfaces is described. A resumé of earlier unsuccessful, and later successful experiments, is followed by a description of the experiment itself and a discussion of results. In order to perform this experiment it has been necessary, as described in chapter 2, to construct an electrostatic positron beam operable at suitable energies and with the requirements of relatively low angular divergence and small beam diameter, and further interface this beam with an interaction region containing various targets and detectors.

3.2 An Historical Introduction to Ps^* Formation

Since the first observation of ortho-positronium by Shearer and Deutsch (1949) the search for the first excited state of positronium, Ps^*, became the natural successor for many experimenter's attentions. Deutsch et al (1953) attempted to excite ground state ortho-positronium formed in the gas with the u-v light from an arc lamp. The experiment was discontinued because the population of the 2P levels was thought to be too low to measure. Hughes (1957), using an optical spectrometer and photomultiplier tube, cooled to liquid nitrogen temperatures, failed to see the Lyman-α line when stopping positrons from a 1Ci (37GBq) source in freon and SF_6. It was concluded that less than one Ps^*atom was formed for every 30,000 positrons under these experimental conditions. Brock and Streib (1957) stopped positrons in a gold foil situated at the slit of a cooled optical spectrometer, with the whole arrangement held in vacuum. A uniform spectral distribution from 235-265nm was obtained. The same distribution was also observed when a β^--emitter replaced the positron source, implying that the observed broad band signal was due to the fast particles scintillating in material close to the entrance to the spectrometer.

71

Bennett *et al* (1961) reported that less than 0.6% of the positrons stopping in Ar and Ne resulted in Lyman-α radiation, and suggested that the high kinetic energy of the Ps* so formed may lead to ionisation before de-excitation. Employing a similar approach Duff and Heymann (1962) observed, along with broadband scintillations believed to be due to the Čerenkov radiation of Compton scattered electrons, a peak at 260nm which was present with either β^+ or β^- in emitters in place. They therefore concluded that this peak must be due to gas excitation.

Fagg (1970), again chose argon as the target in which to stop positrons and used mirrors to guide the light produced to a photomultiplier tube (PMT). In an effort to reduce the positron correlated background present in previous experiments, a quadruple coincidence between the Lyman-α photons produced on de-excitation and the three γ-rays from the annihilation of the same atom was invoked. Due to the low signal rates anticipated, interference filters centred on 233nm, 243nm and 253nm were used instead of the customary u-v spectrometer. No signal above background was observed. McCall (1973) attempted to observe the changes in the γ-ray spectrum of Ps in Ar, SF_6, CCl_2F_2 and Xe when optical radiation was used to excite the 1^3S_1 o-Ps into the 2^3P_J levels. A null result was reported. Dahmand Eck (1974) immersed a 135mCi ^{58}Co source in liquid He, and employed a monochromator and PMT to view the Lyman-α line again with a null result. Evidence was obtained for the existence of Ps* by Vargrese *et al* (1973), who after exciting 1^3S_1 positronium into the 2^3P_J states, using a broad band u-v lamp, applied a strong magnetic field to mix the $n=1$ and $n=2$ singlet and triplet levels and observed an increase in the 2γ annihilation rate. Keilkopf and Ouseph (1974) deposited 10mCi of ^{22}Na on one side of a quartz crystal while evaporating a reflecting Al coating on the other side . Single photon counts were measured in 100Å wide wavelength regions using a grating spectrometer. A statistically significant increase in the 243nm region was reported.

All of these attempts to observe the excited state, with the exception of the work of Brock and Strieb (1957), required that the excited atoms were produced by positrons moderated in view of the PMT. By this method a large photon background would always be present, and as excitation and ionisation of the moderating atoms would be part of the slowing
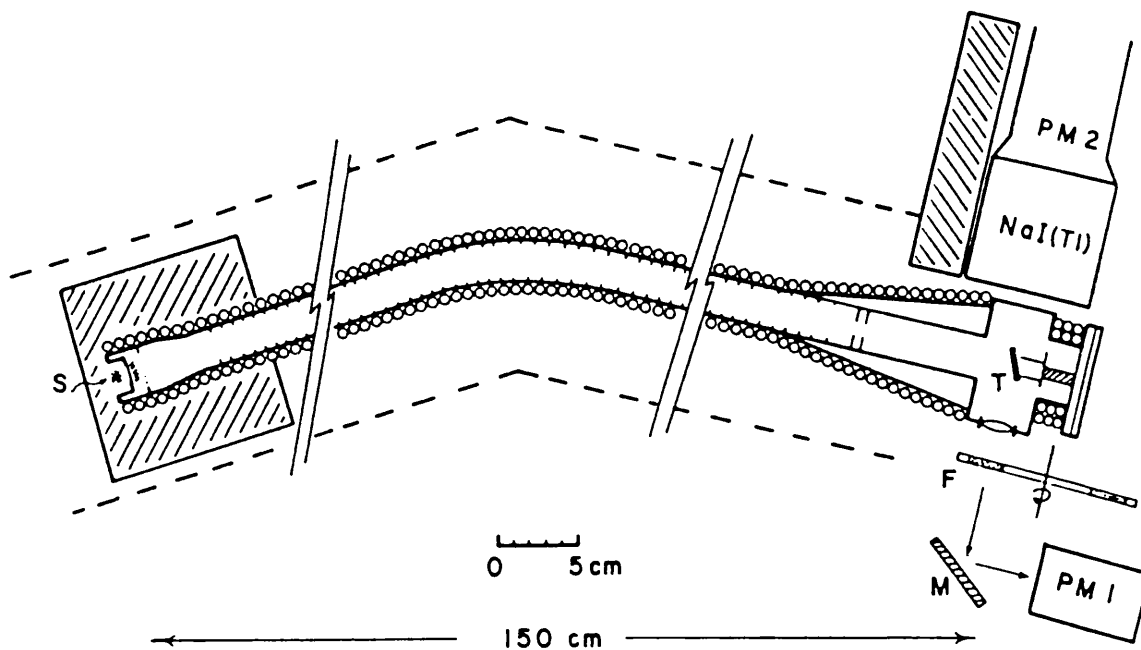
Figure 3.1 A schematic diagram of the experimental arrangement of Canter *et al* (1975).

down process, optical decay and recombination would always follow. Thus, even the imposition of a quadruple coincidence between the Lyman-α photons and the three annihilation quanta, as tried by Fagg (1970) would not have been an unambiguous test for Ps*. The γ-rays from the source and annihilating positrons could also be a source of unwanted background, either by scintillating in the PMT window itself or by scintillating in a material elsewhere in the experiment. Finally, Ps* formed in a dense medium would be subject to collisional de-excitation, possibly where a photon may not be emitted, or collisionally ionised before de-excitation. As a result the observation of Ps* formed in these targets would prove very difficult if not impossible.

The first clear evidence of Ps* formation was demonstrated by Canter *et al* (1975), using a low energy e$^+$-beam where the fast β^+ particles from a 180mCi ^{58}Co were moderated in a Au-MgO converter, and magnetically transported to an interaction region 1.5m away

from the primary positron source, as shown in the schematic of the apparatus, fig.3.1. At 25eV, a beam of $10^4 e^+ sec^{-1}$ was incident on a variety of targets. Any light produced at the target, which was tilted with respect to the beam axis, was focused with a Suprasil lens, which interfaced with the vacuum chamber, on to a mirror which in turn reflected the photons onto the window of a PMT. Between the lens and the mirror, a number of different filters centred on the 243nm Lyman-α line and 30Å either side could be inserted to intercept the photons, thus allowing the spectral profile of the light in that wavelength regime to be determined. It can be seen from fig.3.2 that indeed an enhancement in the Lyman-α/γ-ray coincidences for the filter centred on 243nm can be seen. Fig.3.3 shows the full coincidence spectra and the o-Ps delayed component is clearly seen, though in this case the fitted lifetime is 50nsec, shorter than the expected 142nsec, but which can be understood if effects such as premature quenching of the o-Ps at the walls of the chamber, or the o-Ps moving out of the view of the NaI detector, are considered. Given the beam intensity and efficiencies of the detectors used, it was estimated that in the 2^3P_J states at least, an efficiency of approximately 10^{-4} Ps*per incident positron was achieved.

The success of this experiment, where so many previous attempts had failed, is due to two main differences in approach. Namely, the use of a slow positron beam as opposed to a positron swarm, and because of this, instead of a combined moderator/Ps* converter, a separate solid target was used. Employing a positron beam eliminated much of the background produced by γ-rays and fast particles from the source scintillating in the quartz window of the PMT, though 511keV γ-rays from positron annihilation in the target area could still lead to unwanted scintillations. As the positrons were all at low energies the problem of light resulting from target excitation was much reduced. By using interference filters accidental coincidences, ie. an incoming positron produces a photon by Coulomb excitation of the target and then goes on to form o-Ps, could be eliminated. Finally by requiring that the Lyman-α photon produced on de-excitation occurred in coincidence with one of the γ-rays from the subsequent annihilation of the same atom, as opposed to all three in the experiment performed by Fagg (1970), the overall detection efficiency of the experiment was sufficiently high to allow the signal to be unambiguously observed. It is for these reasons that this technique of Ps* production and detection has been utilised in almost all subsequent studies of Ps in the excited state.

74
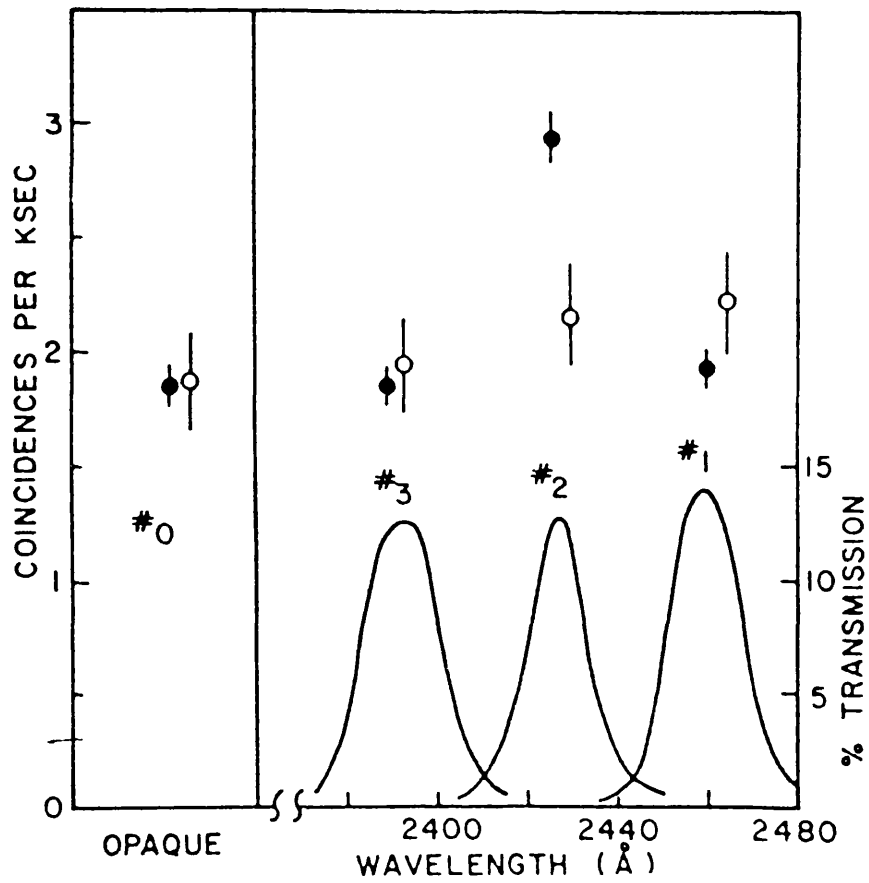
Figure 3.2 The total Lyman-α/γ-ray coincidence rate for filters centred on 200nm, 240nm, and 280nm (Canter *et al* (1975)).
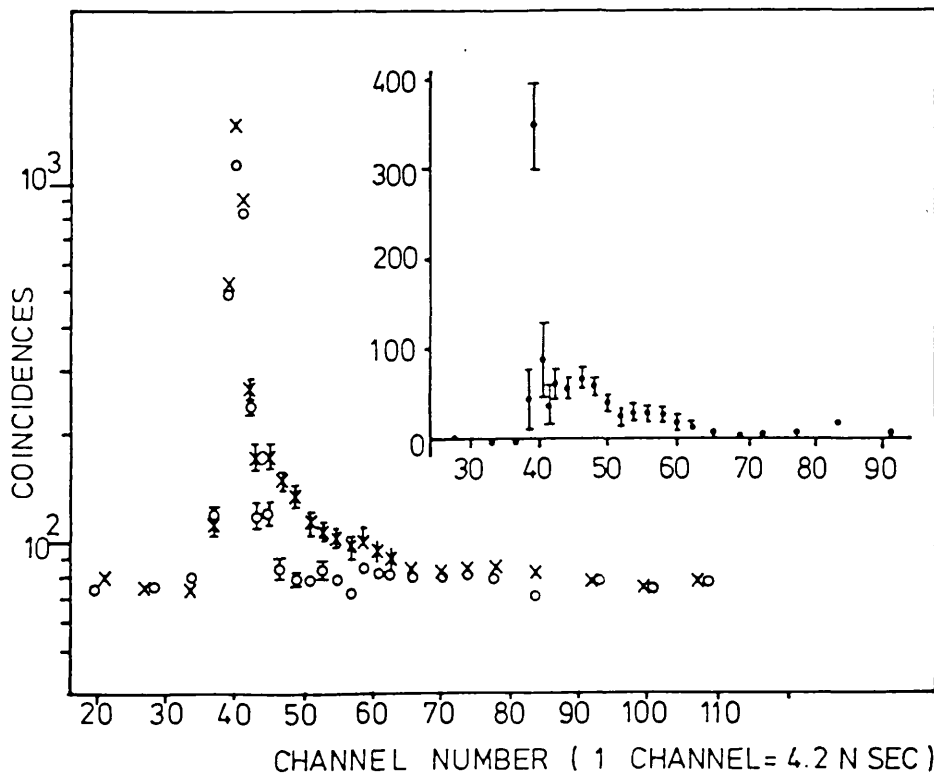
Figure 3.3 Timing spectra obtained by placing a Lyman-α detector in coincidence with a γ-ray detector (Canter *et al* (1975)).

75

3.3 Models of Ps Formation

3.3.1 Introduction

Before discussing Ps* formation in particular we must first consider the processes by which positronium in any state is formed when a positron encounters a given media. The moderation process is described in chapter.1 §.1.4.2 so let us assume that in all cases the positron has been moderated and is thus at an energy of the order of several keV or less.

3.3.2 The 'Ore' Model

The simplest case of Ps formation occurs in diffuse gases and may be described by the 'Ore' model (Ore (1949)) which assumes production via the charge transfer process.

$$e^+ + A \rightarrow Ps(n) + A^+ \tag{3.1}$$

Here an electron is picked-up by an incoming positron from the target atom/molecule, A, to leave a positive ion, A^+, and a positronium atom. The kinetic energy of the Ps atom, E_{Ps}, produced in this manner is dependent on the kinetic energy of the incoming positron, the first ionisation potential of the target, E_I, assumed to be in the ground state, and the n-state of the Ps atom formed, since the binding energies, $E_B(n)$, of the excited Ps atoms are given by

$$E_B(n) = \frac{6.8}{n^2} \ (eV) \tag{3.2}$$

E_{Ps}, therefore, will be

$$E_{Ps} = E_+ - E_I + E_B(n) \tag{3.3}$$

where n is the Ps principal quantum number. It can also be seen, therefore, that the threshold for Ps formation in any state is given by

$$E_{e^+} = E_I - E_B(n) \qquad\qquad (3.4)$$

Ps formed with a residual kinetic energy in excess of its own binding energy is likely to be rapidly ionised in a collision with a third body. This then sets an upper and lower limit on the effective energy range of Ps formation by positron-atom/molecule interactions, known as the 'Extended Ore Gap', which can be written thus

$$E_I - E_B(n) \leq E_{e^+} \leq E_I \qquad\qquad (3.5)$$

It can be seen that the width of the 'Extended Ore gap' will be $E_B(n)$ in all cases.

The 'Ore' model has also had some success when applied to more complex systems such as rare gas solids (Gullikson and Mills (1986)) and ionic crystals (Lynn and Nielsen (1987)). The solid state Ore condition will be given by

$$\phi_- + E_g - (E_B^* + \epsilon_{Ps}) \leq \omega_+ \leq E_g - \phi_+ \qquad\qquad (3.6)$$

where E_g is the band gap of the solid, E_B^* is the binding energy of the Ps in the bulk, ϵ_{Ps} is the positronium formation potential, given by eqn.3.10, (see §.3.5.2 for a further explanation of these parameters) and ω_+ is the ground state energy of the positron in the crystal which is simply equal to $-\phi_+$.

3.3.3 The 'Spur' Model

While the 'Ore' model has proved to be satisfactory in describing Ps formation in gases, it should be noted that testing the validity of the model as applied to condensed matter is extremely difficult, principally as the bulk affinities for positrons, electrons and positronium are unknown. In an attempt to address these and other shortcomings a second formation process was proposed by Mogensen (1974) which has become known as the 'spur' model. Here a positron implanted into a dense medium will leave in its wake, among other things, a spur of ions and free electrons produced in the final stages of the slowing down process. In this environment the cooled positron may then combine with a spur electron left in the conduction band and form positronium. Opportunities exist to
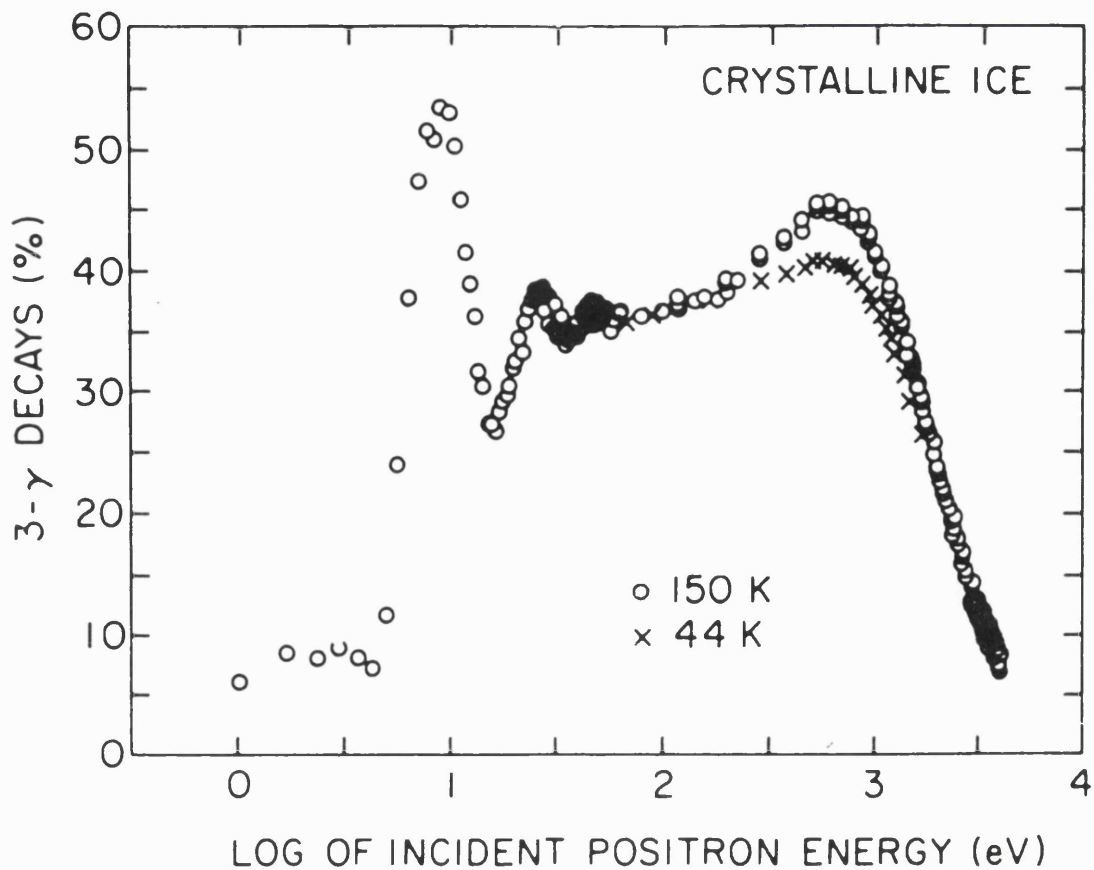
Figure 3.4 The positronium yield from positrons implanted into ice as a function of positron energy (Eldrup *et al* (1983)).

test such a model, eg. by introducing electron scavengers to reduce the free electrons in the spur and then note the effect on the Ps formation probability (Mogensen and Shantarovich (1974)). For a fuller discussion of the relative merits of each model in a given environment, see the review of Dupasquier (1981). Evidence supporting both the Ore and spur models is given by fig.3.4 from the work of Eldrup *et al* (1983), which shows the Ps yield as a function of e$^+$ energy for positrons implanted into ice. At high energies, the Ps yield increases indicating a spur type process, as the high energy positrons produce large numbers of free electrons as they slow down. At low implantation energies, an Ore type process is responsible for the peak at 6-10eV, where valence electrons are promoted into the conduction band while correlated to a positron . A second peak corresponding to the second ionisation potential can be seen at around 25eV.

3.4 Positronium Formation in Gases

The production of ground state positronium by positron impact in gases is well documented. Formation cross-sections for many gases at various energies have been determined experimentally, for example Fornari *et al* (1983), Fromme *et al* (1986), and more recently Stein *et al* (1992). Comparison to theory however, may only be made for simple gases such as hydrogen and helium. Fig.3.5 shows the measured Ps formation cross-section for hydrogen of Sperber *et al* (1992) which perhaps surprisingly shows close agreement to the relatively unsophisticated first Born approximation calculation of Massey and Mohr (1954) and second Born calculation of Igarashi and Toshima (1993). The close coupling calculation of Hewitt *et al* (1990), the most advanced theoretical method currently used can be seen to produce maxima 30-40% lower than the experimental data and the symmetrised Fock-Tani transformation method used by Lo and Girardeau (1990) is lower still.

Experimental results for helium also exhibit some deviation from theory. Fig.3.6 shows the most recent Ps formation cross-section measurements of Fromme *et al* (1986) along with the theoretical treatments of Mandal *et al* (1979), Khan *et al* (1985) and McDowell and Peach (1985). Although there would appear to be some agreement at low energies, the discrepancies at higher energies have led the authors to believe that this may be fortuitous. However, new data has recently been obtained by Overton *et al* (1993) which exhibits much better accord with theory at all energies.

Despite the disagreement with theory, measured cross-sections do allow the relative yields of Ps from positron-gas collisions at particular pressures and impact energies to be estimated. By considering these data and following the verification of the forward-peaked nature of the formation process (Laricchia *et al* (1987)) in accordance with theoretical predictions (Mandal *et al* (1986)), the first naturally collimated Ps beam was developed by Laricchia *et al* (1988). Here timed slow positrons were passed through a cell containing He or Ar. The forward going Ps atoms exited the cell and were detected with a CEMA biased to reflect positrons. It is interesting to note that, by examining the energy spectra of the Ps in the beam, it was possible, when corrected for
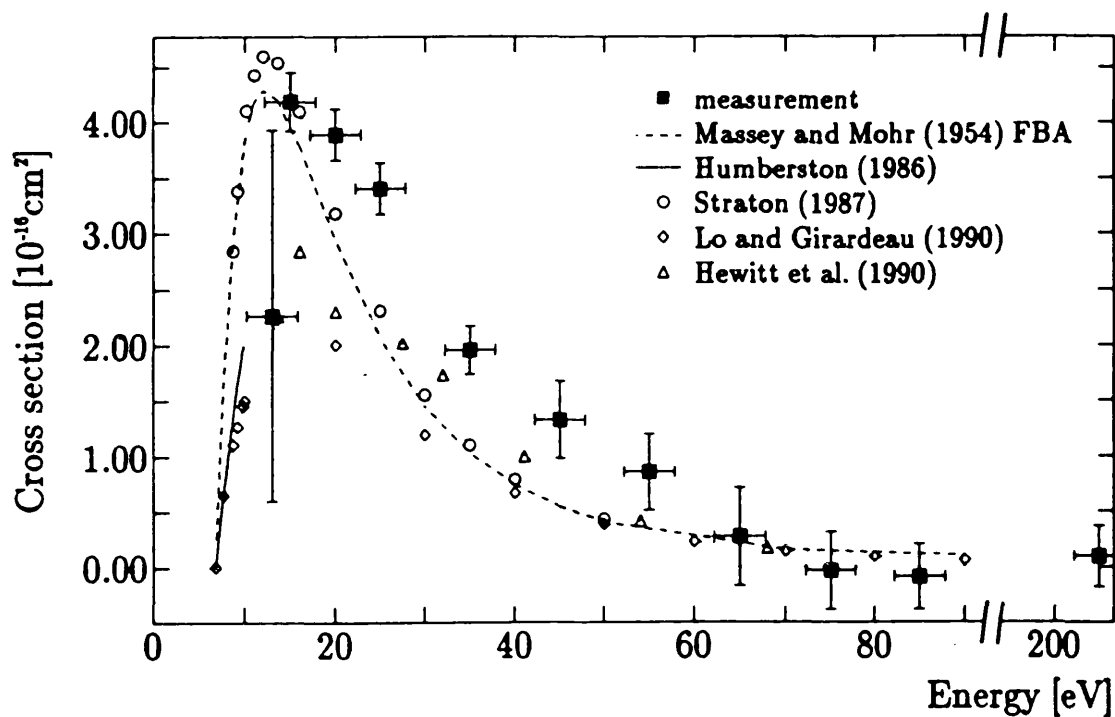
Figure 3.5 The Ps formation by positron impact with atomic hydrogen measurements of Sperber *et al* (1992), along with the theoretical treatments of Massey and Mohr (1959), Humberston (1986), Straton (1987), Lo and Girardeau (1990) and Hewitt *et al* (1990).
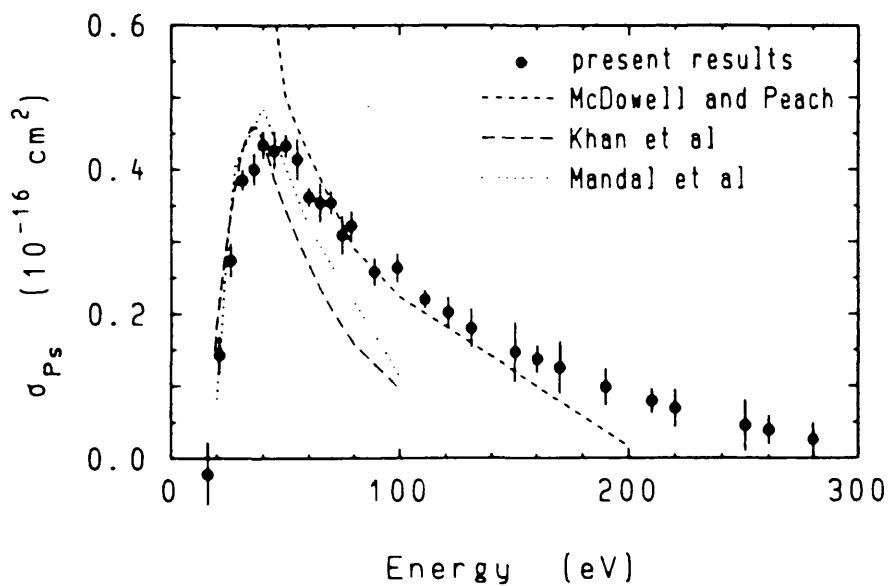
Figure 3.6 The Ps formation by positron impact with helium measurements of Fromme *et al* (1986) along with the theoretical treatments of Mandal *et al* (1979), Khan *et al* (1985) and McDowell and Peach (1985).
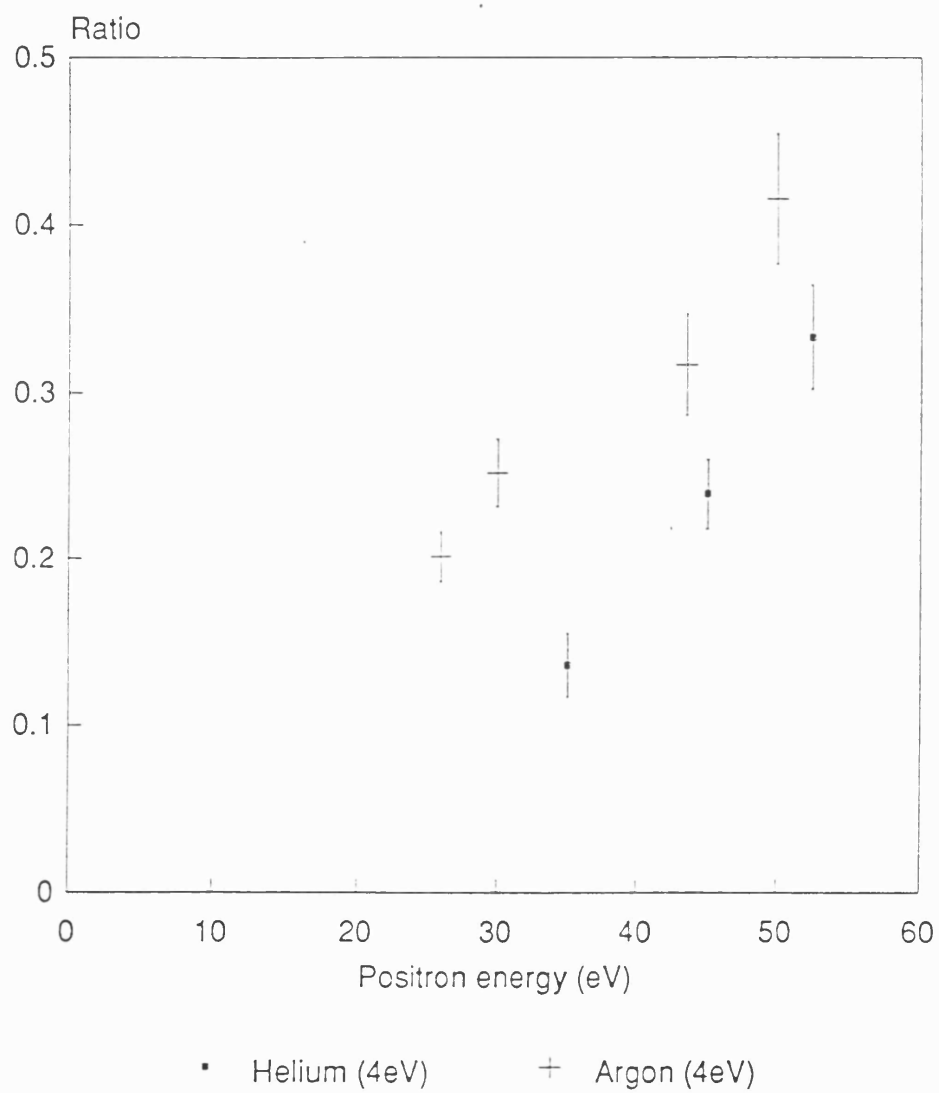
Figure 3.7 The ratio of measured n=2 to n=1 Ps yield by positron impact with helium (■) and argon (+) for Ps in the 4eV kinetic energy region (Zafar *et al* (1991)).

decay in flight, to estimate the ratio of that formed in all excited states to that in the ground state (Zafar *et al* (1991)). Fig.3.7 shows this ratio for He (between 14-33%) and for Ar (between 20-42%), as a function of positron impact energy, along with the theoretical calculation for He of Mandal *et al* (1980). These yields were consistent with the earlier Ps* formation measurements of Laricchia *et al* (1985) where it was estimated that up to 5.7×10^{-2} Ps*/e$^+$ were formed for positrons at 16eV. Early Born approximation calculations by Massey and Mohr (1954) had indicated that the formation proportions would be roughly proportional to $1/n^3$, and so such high yields were not totally unexpected.

3.5 Positronium Formation and Solids

3.5.1 In the Bulk

One of the early experiments to observe positronium formation in a solid was that of Paulin and Ambrosino (1968) who looked for Ps in powdered insulators. Curry and Schawlow (1971) detected Ps emerging from MgO powder into vacuum and the potential of solids as sources of low energy positronium was realised.

Ps formation within the bulk cannot occur in metals and semi-conductors, with the possible exception of materials containing concentrations of large voids, as the free-electron density is so high that a positron entering the bulk is immediately screened and thus correlation with a single electron may not occur. In contrast, materials in which free-electron densities are low, such as insulators and ionic and molecular crystals, permit bulk Ps formation to take place by the promotion of, and correlation with, an electron from the valence band. This excitonic or quasi-positronium, qPs, is then free to diffuse through the bulk in a delocalised Bloch state.

The character of this qPs is similar to that of Ps in vacuum, eg. the existence of singlet and triplet qPs was first demonstrated in magnetic quenching experiments by Bisi *et al* (1971). In practice however it is often the material that dictates the lifetime against annihilation of qPs. This is because polarisable materials will act to reduce the Coulomb

field between the positron and electron thus leading to large radial separations and a reduced binding energy. As a result the overlap between the e^+ and e^- wavefunctions will be small. Typical decay rates for ortho-qPs are of the order of hundreds of picoseconds and reflect the electron density of the solid.

3.5.2 Ps Emission from Solids

For many non-metallic solids, Ps emission is characterised by the positronium workfunction. This relates to the potential energy difference that exists between Ps just inside, and just outside the surface, as given by

$$\phi_{Ps} = -\mu_{Ps} + E_B^* - \frac{6.8}{n^2}(eV) \qquad (3.7)$$

where ϕ_{Ps} is the positronium workfunction, μ_{Ps} is the Ps bulk chemical potential and E_B^* is the Ps binding energy within the solid (after Schultz and Lynn, 1988.). If it is assumed that the Ps chemical potential is in equilibrium with that of the positron and the electron when considered individually, ie.

$$\mu_{Ps} = \mu_+ + \mu_- \qquad (3.8)$$

Then eqn.3.7 may be restated thus,

$$\phi_{Ps} = E_B^* + \phi_+ + \phi_- - \frac{6.8}{n^2}(eV) \qquad (3.9)$$

where all the variables have been previously defined. Energetic positronium emitted as a result of favourable bulk characteristics, ie workfunctions, is sometimes known as 'promptly emitted' Ps. To date all materials examined (with the possible exception of diamond, Brandes *et al* (1992)) have $\phi_{Ps} > 0$ for $n > 1$.

In the case of metals, Ps formation may not occur in the bulk. However, not all thermalised e^+s reaching the surface of a metal into which they have been implanted are re-emitted as slow positrons. A thermalised positron leaving the bulk and passing through

the surface enters a region of decreasing electron density and if the energy constraints implied by eqn.3.10 are satisfied, positronium may be formed.

$$\epsilon_{Ps} = \phi_+ + \phi_- - \frac{0.8}{n^2}(eV)$$ (3.10)

It can be seen that Ps will only be formed where ϵ_{Ps} is negative. It may also be readily seen that the maximum kinetic energy of the resultant Ps will be $-\epsilon_{Ps}$. For all metals the combination of electron and positron workfunctions is insufficiently small to permit the formation of Ps (by a thermalised positron) in any state other than $n=1$.

3.5.3 Thermally Desorbed Ps

The fate of those thermalised positrons which have reached a metal surface does not only lie in emission to vacuum of a bare positron or the formation of 'promptly' emitted positronium. It is also possible for the positron to become trapped at the surface in its own image potential, with typical binding energies of the order of several eV. A positron in this state is subject to the alternative description of a Ps atom bound to the surface by Van der Waals forces, with a binding energy E_a, also known as the activation energy, and given by

$$E_a = \epsilon_+^s + \phi_- - \frac{6.8}{n^2}(eV)$$ (3.11)

where ϵ_+^s is the positron binding energy to the surface state. For $n=1$ Ps, E_a is less than 1eV for most metals. Fig.3.8 is a schematic diagram of the surface potential as seen by this surface bound Ps. For those materials studied it has proved possible to desorb such Ps by heating the solid. The desorption process may be understood by considering the thermal fluctuations in the positrons' kinetic energy within the surface trap. The high energy tail of the presumed Maxwellian distribution allows the surface bound Ps to overcome E_a and thus escape the surface well. Fig.3.9 is a typical example of the temperature dependence of the Ps formation fraction from a clean metal surface, as measured by Mills and Pfieiffer (1985). Here an Al(111) surface was heated and the Ps
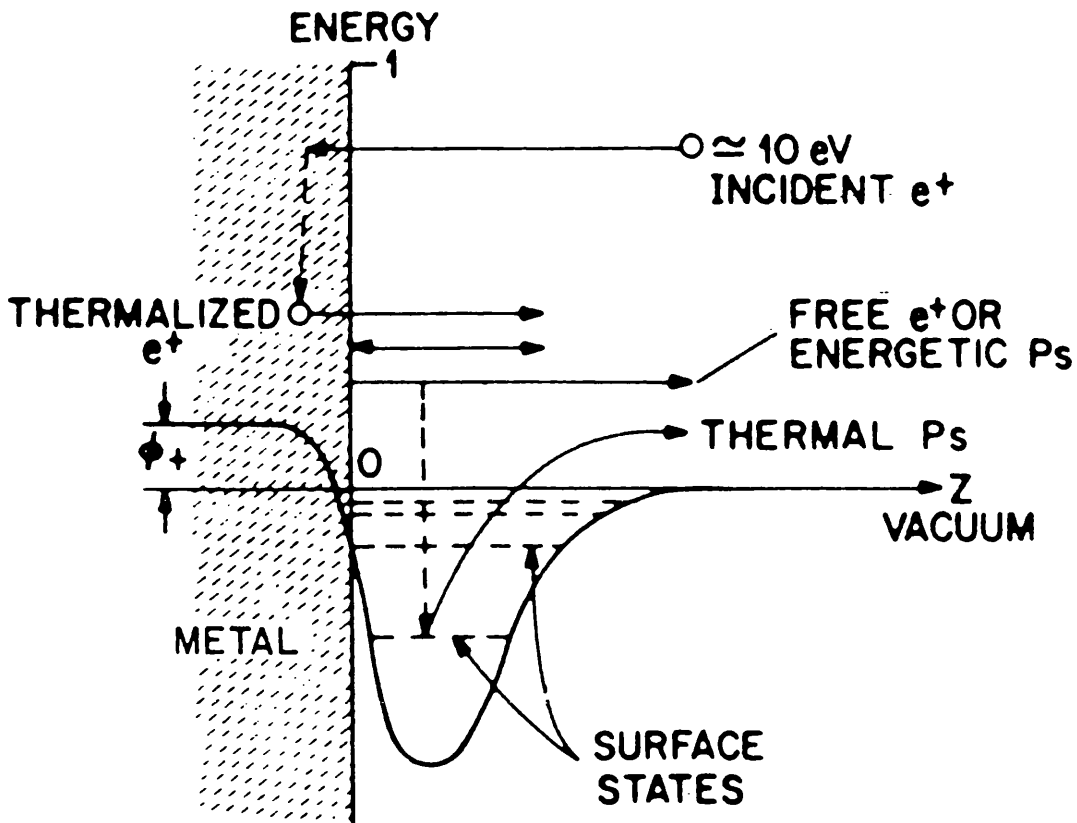
Figure 3.8 A schematic diagram of the surface potential as seen by a surface bound Ps atom.
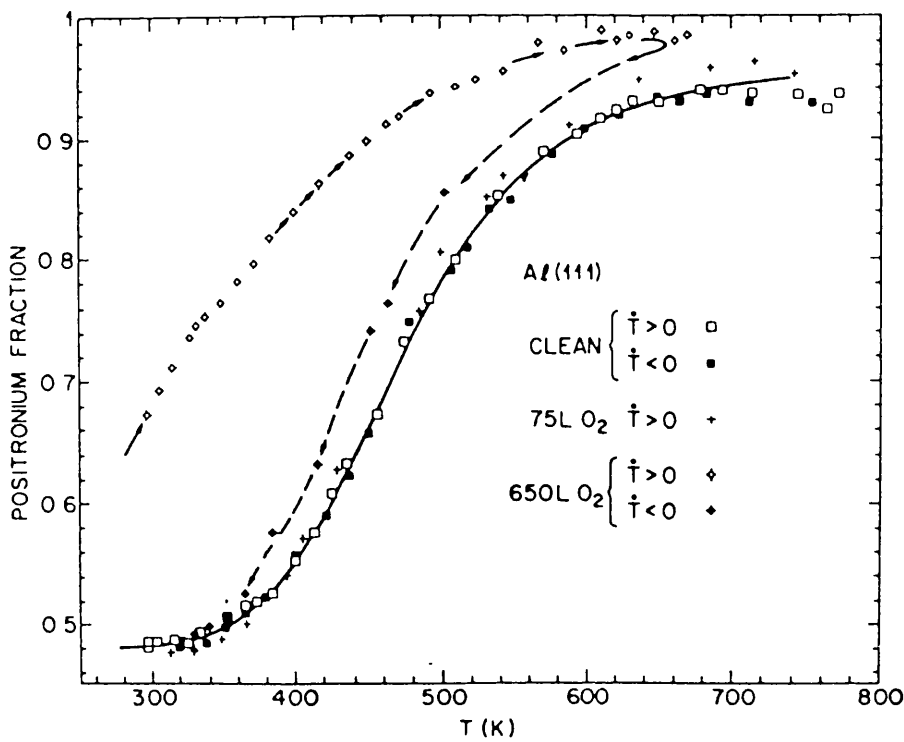
Figure 3.9 The temperature dependence of the Ps formation fraction from a clean aluminium surface (□,■) (Mills & Pfieffer (1985)).

fraction measured. Note that the Ps fraction follows the same curve when heated and cooled, thus indicating that the surface is truly clean.

3.5.4 Epithermal Positronium

The formation of Ps* by any of the above processes does not usually occur as most materials have electron workfunctions of the order of 4eV, and positron workfunctions are insufficiently negative to render Ps* formation possible. Positronium produced by thermal desorption also cannot provide a source of Ps* because the thermal fluctuations are small and the activation energy large for excited states. Thus the only candidate for useful Ps* production is epithermal positronium, ie. Ps formed by non-thermalised positrons, for it is only here that the energy balance restrictions of eqn.3.9, eqn.3.10 and eqn.3.11 do not apply.

On implantation, not all positrons remain in the bulk for sufficient time to thermalise. This is because some positrons may undergo an elastic collision with an atomic core and are scattered back towards the surface of entry. As the mean free path of a positron is dependent on energy, some positrons may travel considerable distances within the bulk with little or no further energy loss. Fig.3.10 shows the mean free path of positrons in aluminium (Nieminen and Oliva (1980)). It can be seen from their calculations that a positron of 50eV would have a mean free path of the order of 5Å. Using Eqn.3.12 (Schultz and Lynn (1988)), normally applied to higher positron energies, one may make a crude comparison with the implantation depth of such a low energy positron. Here $\bar{z}$ is the implantation depth (in Å), ρ is the sample density (in gram/cm^3), E is the positron energy (in keV) and n is empirically determined and found to be 1.6 for most materials.

$$\bar{Z} = \frac{400}{\rho} E^n \qquad (3.12)$$

One finds that for low positron energies the implantation depth is comparable or in many cases less than the mean free path, and as such the escape probability for these positrons
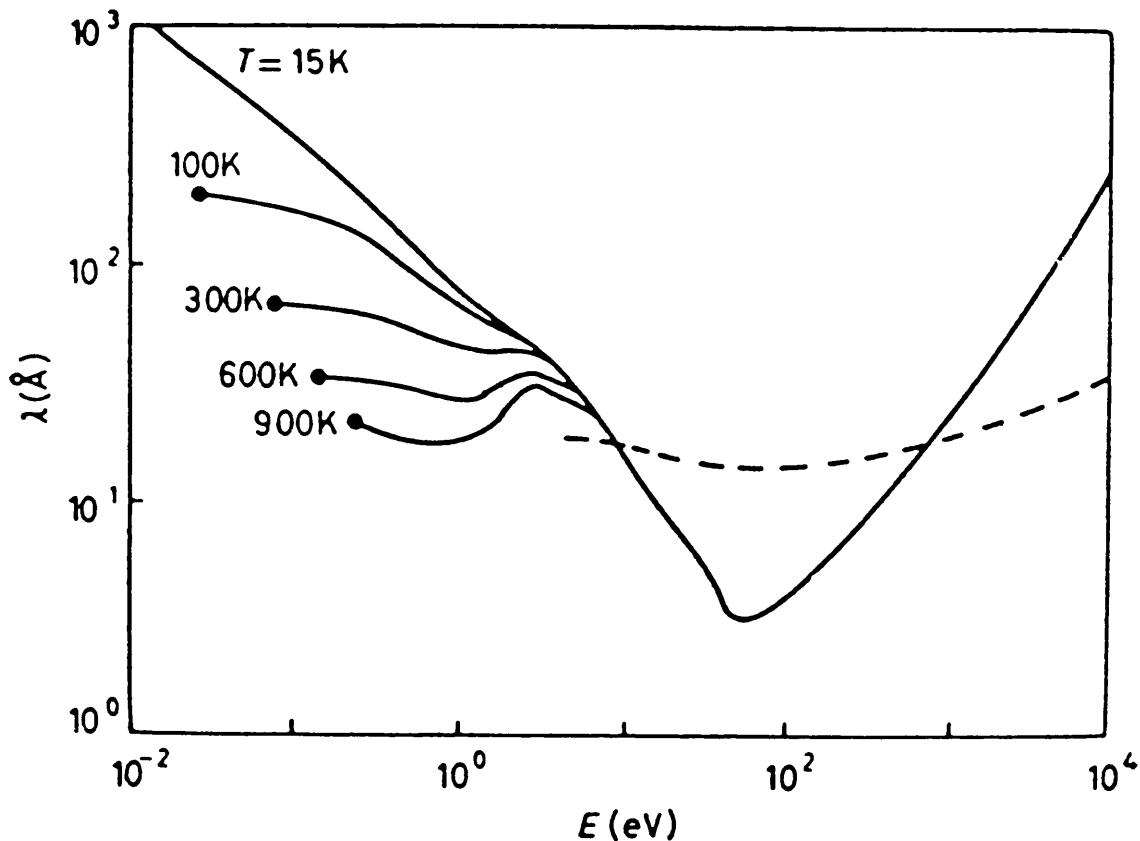
Figure 3.10 The positron mean free path in aluminium as a function of positron energy (Nieminen and Oliva (1980)).

will be high. This source of epithermal positrons passing through the surface is then available to form high velocity Ps by electron capture on exit.

Mills *et al* identified a source of energetic Ps in their work of 1984, where a several keV beam of positrons impinged on a thin carbon foil. Later work by Howell *et al* (1986) discovered that, in terms of velocity, two populations of positronium could be obtained from a number of clean metal surfaces when bombarded with positrons at 50eV-3000eV. Fig.3.11, taken from the work of Howell *et al* (1986), shows positronium time-of-flight spectra for a number of materials subject to positron bombardment at 50eV. A prompt peak corresponding to time zero can be seen to the left of the figure and close to this two distinct distributions. The more delayed component was the familiar formation potential contribution with energies typically of a few eV. The second component corresponded to Ps with a higher kinetic energies, ~ 10eV, a broad distribution and a high degree of Z dependence at low energies, as shown in fig.3.12. This component was attributed to positronium formed by positrons backscattered through the surface. It can be seen that,
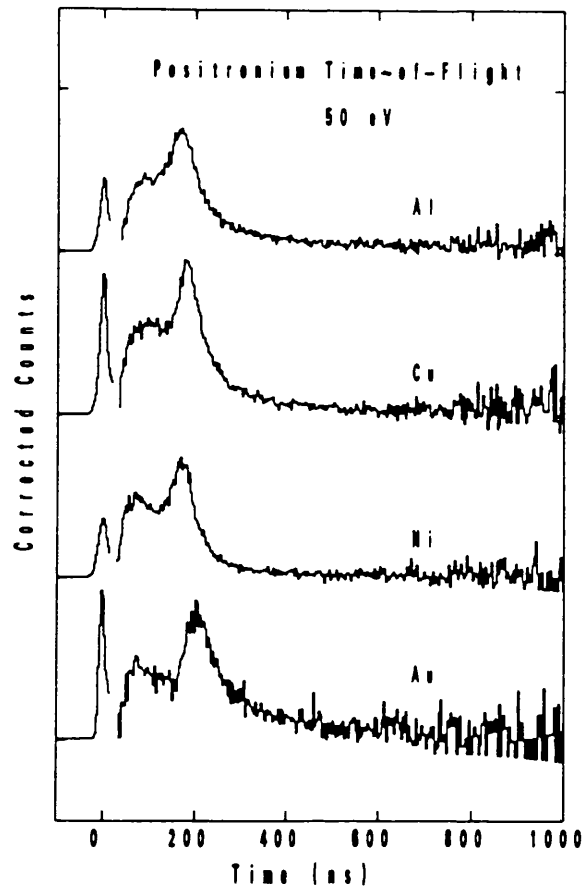
Figure 3.11 Positron time of flight spectra for a number of materials subject to positron bombardment at 50eV (Howell *et al* (1986)).
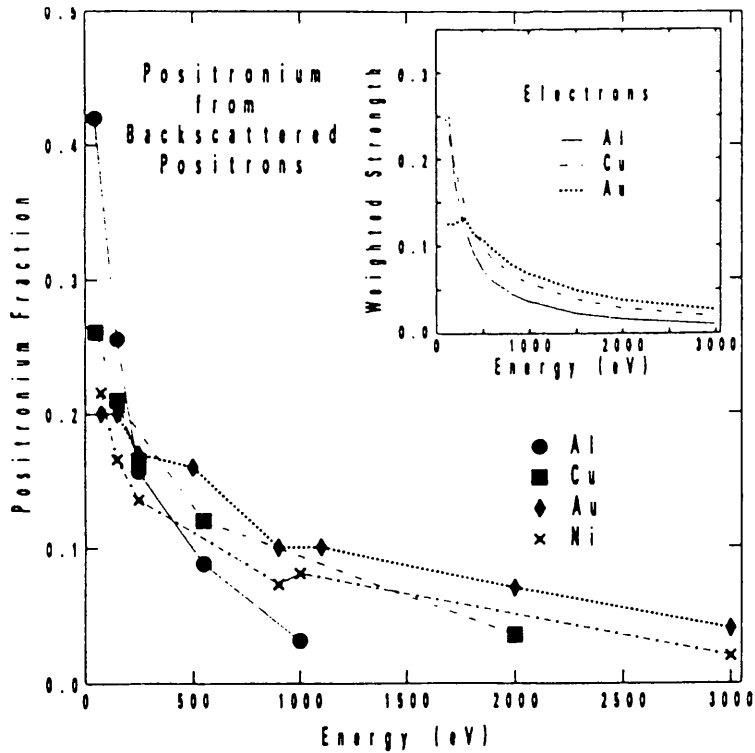
Figure 3.12 The backscattered positronium yield from a number of materials as a function of incident positron energy. Also inset, backscattered electron yields from the same materials after correcting for the 1/E positronium formation cross-section (Howell *et al* (1986)).

88

for aluminium, this fast Ps fraction is more than 40%, a larger Ps fraction than would be expected from a workfunction process, and greater than the yield from the higher Z materials. It is interesting to note that at 100eV, electron backscatter coefficients are also higher for low Z materials (Fitting (1974)) as shown in the inset of fig.3.12. As the incident beam energy increases the backscatter contribution becomes higher for the higher Z materials. This may be understood by considering the large angle elastic scattering of the positrons, which increases with increasing Z, and corresponding reduction in implantation depth. The net result of which is an increased escape probability, and thus higher Ps fraction.

As there is a kinetic energy excess, Ps* production could be expected as there will be sufficient residual energy to liberate the positron and an electron from the bulk, without the benefit of the 6.8eV binding energy gained by formation in the ground state. The minimum residual kinetic energy required to form Ps* in the first excited state (n=2) is given by

$$E_{Kin} = \phi_+ + \phi_- - 1.7(eV) \qquad (3.13)$$

The first experimenters to produce Ps*, see §.3.1, capitalised on this phenomena.

3.6 Recent Ps* Formation Studies

Since the first observation of Ps* much effort has been expended by various groups examining the fine structure of the n=2 level in order to test quantum electrodynamics, QED, as applied to a purely leptonic atom. A discussion of Ps atomic structure, the measurements that have been made and their significance is reserved for the next chapter, as that work is of particular interest in the light of the observed discrepancies between theory and experiment of o-Ps vacuum lifetime measurements (Nico et al (1992)-see chapter.4 §.4.2). It is only in relatively recent years that Ps* production itself is coming under closer scrutiny, albeit only in attempts to enhance yields for improved measurements.

The first Ps* yield measurements were made by Canter et al (1975) in the experiment

described in §.3.2; here Ge, C, MgO, Au, Ti and SiO_2 targets were used. All targets produced yields within 50% of the 10^{-4} Ps^*/e^+ observed from Ge, with the exception of the carbon target from which no Ps^* was detected at all. Raising the temperature of the targets from 30°C to 450°C led to no difference in Ps^* yields, yet ground state o-Ps production rose by as much as a factor of three, thus indicating that the formation process was different for each of the populations. This original experiment was performed in a relatively low vacuum and so UHV experiments were expected to shed some light on the formation process.

The effects of surface contamination were first examined by Schoepf et al (1982) for a sputtered tungsten target in a 10^{-9} torr vacuum. Yields were measured before and after cleaning and are shown in fig.3.13. It was concluded that Ps^* formation was not sensitive to surface conditions, however a threshold for formation of 8eV was observed. It should be noted that the 'untreated' target had in fact been chemically etched and then annealed to 2000°C in a 10^{-5} torr vacuum before being placed in UHV. This work did however give a higher value for the Ps^* yield from a metal, a maximum from W of $3.93(60) \times 10^3$ Ps^*/e^+ at 10eV. More recently the work of Ley et al (1990) has found similar yields from Mo. As this work was performed in a 100G magnetic field, the microwave power used to induce the $2^3S_1 \rightarrow 2^3P_J$ transitions was frequency shifted due to the motional Stark effect. From the magnitude of the shift it was possible to calculate the Ps^* kinetic energy, and an average of 4.9eV was estimated. In addition Ps^* yields as a function of energy were measured as shown in fig.3.14 and a maximum at 50eV can be seen.

In 1992, Schoepf et al presented additional data on clean tungsten and copper in a UHV environment, utilising the apparatus of the 1982 experiments, as shown in fig.3.15. This work reported maximum Ps^* yields of $(3.70\pm0.53) \times 10^3$ Ps^*/e^+ for polycrystalline tungsten at 12eV and $(2.73\pm0.13) \times 10^3 Ps^*/e^+$ from Cu(100). Fig.3.16 shows the Ps^* fraction from W and Cu as a function of energy. Both samples exhibit thresholds for Ps^* formation in reasonable agreement with the energy balance of eqn.3.13. It is also interesting to note that the higher yield from tungsten indicates a trend in Z opposite to the ground state backscattered yields observed by Howell et al (1986) and discussed in §.3.5.4. Also reported were two components in the lifetime spectra. Though individual
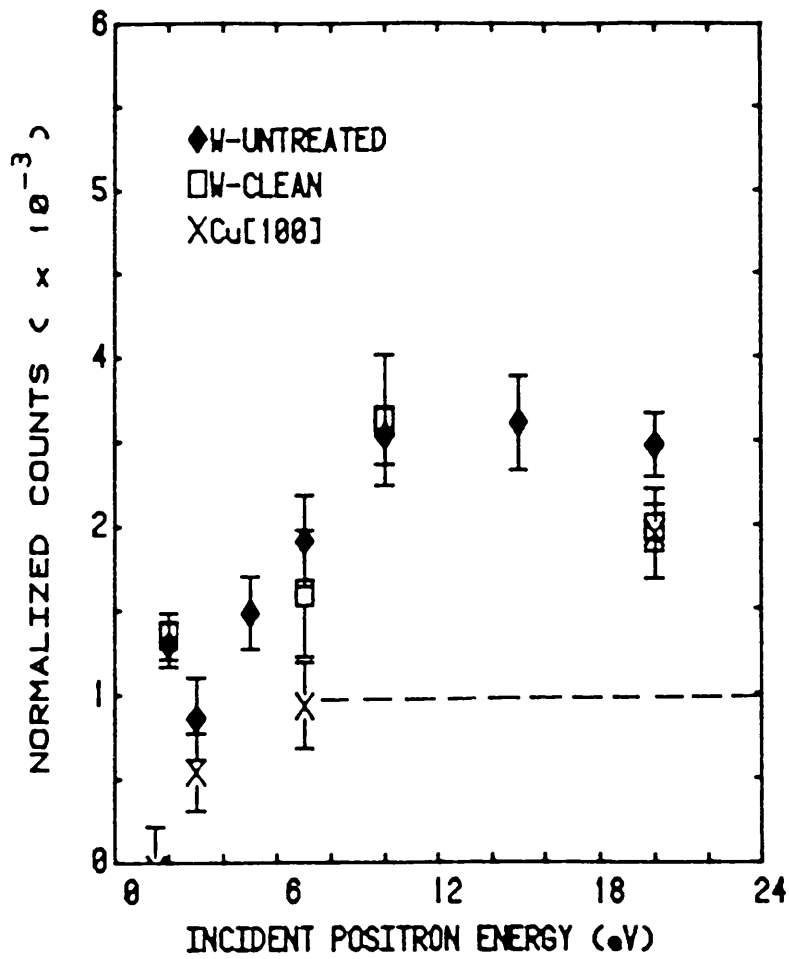
Figure 3.13 The Ps* yield from a W target before and after cleaning, and from an untreated Cu(100) target (Schoepf et al (1982)).
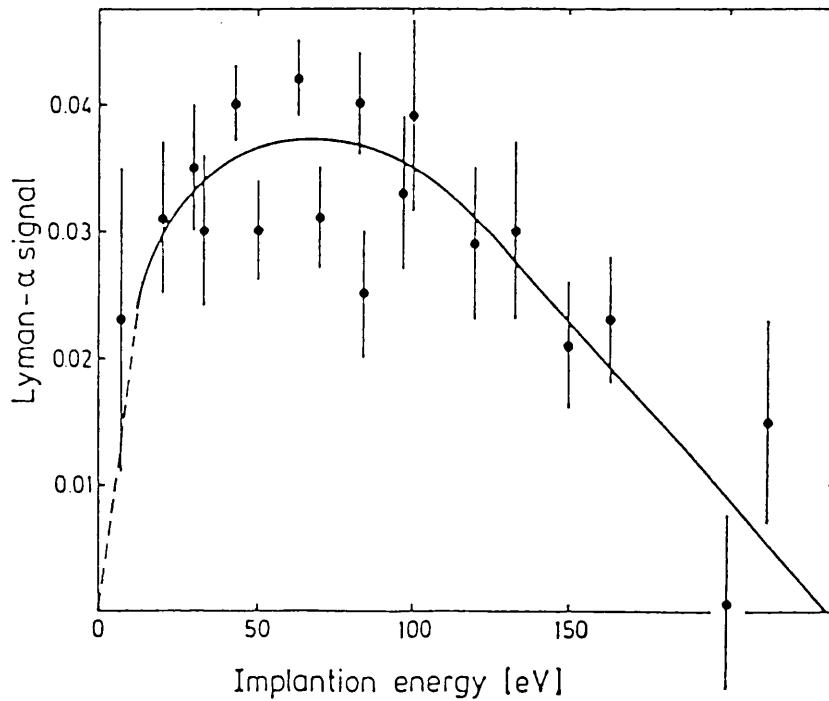
Figure 3.14 The Lyman-α count rate, as a function of energy, for positrons incident on a molybdenum target (Ley et al (1990)).
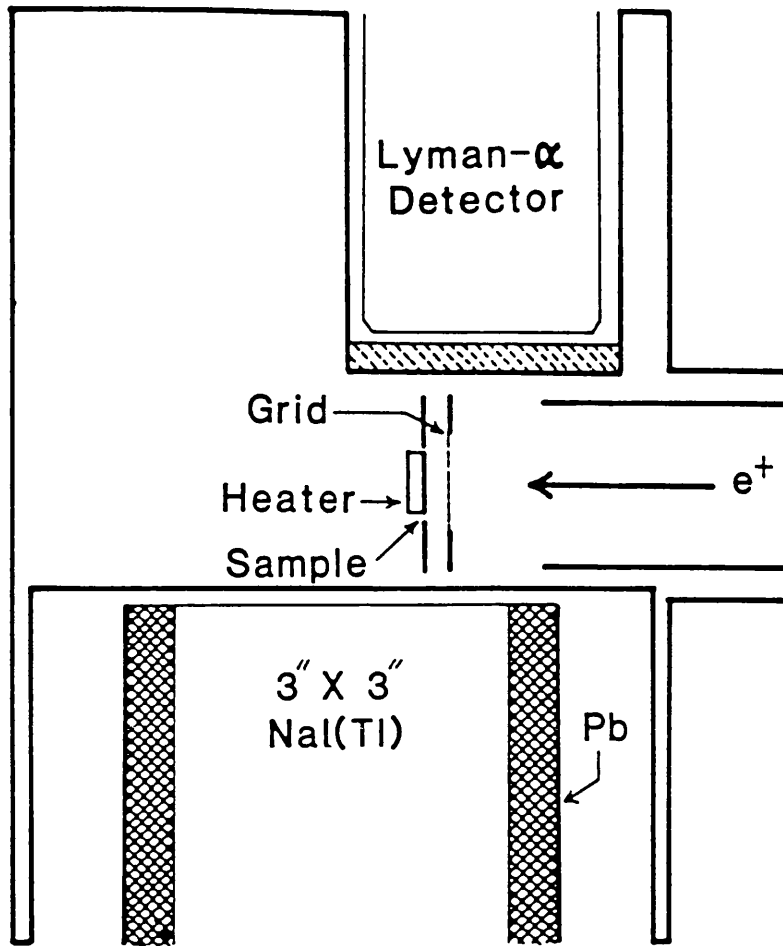
Figure 3.15 A schematic diagram of the experimental arrangement used by (Schoepf *et al* (1982 & 1992)).
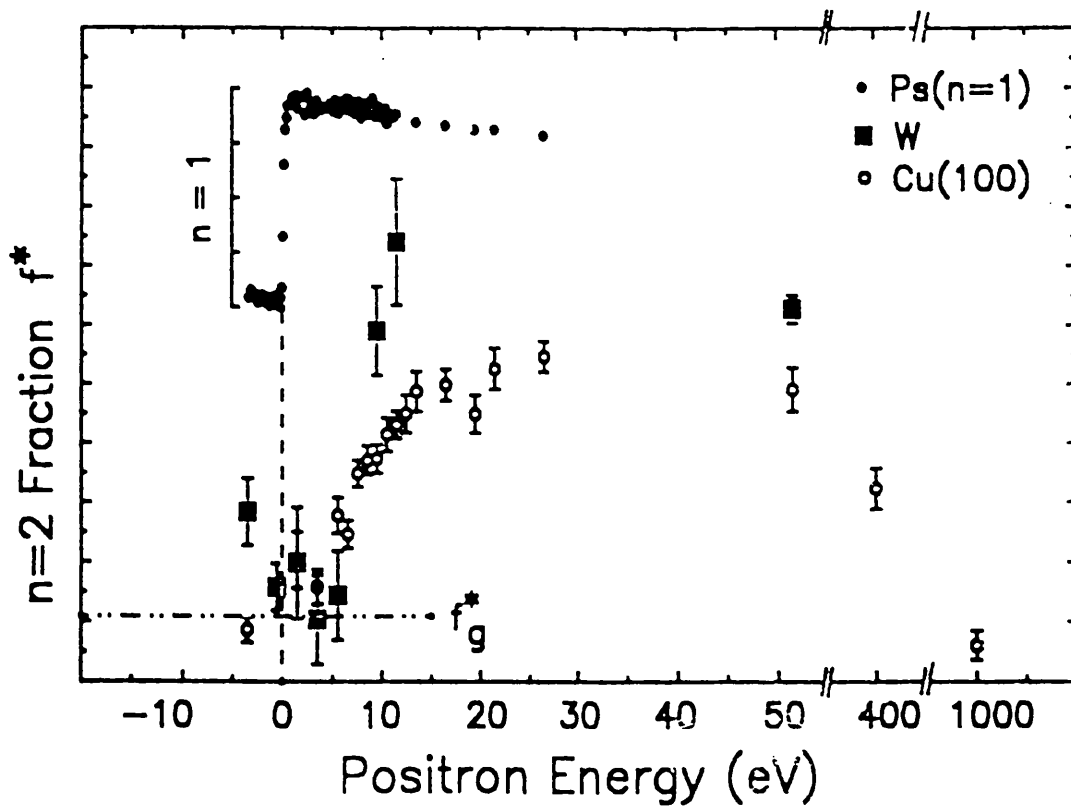
Figure 3.16 Measured Ps* fractions as a function of incident positron energy, from clean Cu and W surfaces (Schoepf *et al* (1992)).

spectra contained insufficient data to allow meaningful fits, by summing all spectra with positron impact energies in the range of 10-50eV, intensities and decay constants could be obtained. A long-lived component of 126.8 ± 8.0 nsec, close to the 142 nsec decay rate of o-Ps, and another at 17.4 ± 2.3 nsec were returned. It was suggested that the short-lived component was "possibly due to a higher velocity non-thermal Ps component that is collisionally quenched in the target chamber". By forcing fits to the individual spectra using the decay constants of the composite, the ratios of the fast to slow Ps* intensities for all the spectra in this energy range were estimated to be 0.75 ± 0.19.

The first evidence of Ps* yields in excess of those found by other researchers was made by Steiger et al (1992), utilising a similar experimental arrangement as Schoepf et al (1992) as shown in fig.3.17. Here they obtained yields of at least 2% from 'dirty' targets after allowing for systematics such as quantum efficiencies, discriminator thresholds and solid angle effects. In this context 'dirty' means surfaces that have not been subject to annealing or sputtering. It was also found that the yield did not vary with target Z contrary to findings in the UHV work of Schoepf et al. Fig.3.18 shows the total Ps* fractions for a wide range of targets at 100eV e^+ energy, the additional separation into fast and slow Ps* fractions are discussed below. It was concluded that surface contaminants, such as residual hydrocarbons from cleaning prior to placement in vacuum, provided a larger area of low electron density surface through which epithermal positrons could pass, thus enhancing the Ps* production probability for low energy positrons, and since the contaminants would be the same in all cases, no Z effect would be expected. In addition to the high yields observed, again the spectra were believed to consist of two components, and again the fit was made to a composite spectrum, in this case the range summed over was 10-200eV. Values of 113.3 ± 6.7 nsec and 18.5 ± 1.7 nsec were found for the slow and fast components respectively. The relative intensities of the fast and slow components however were found to quite different than that of the Schoepf et al (1992) work, as shown in fig.3.19, where it can be seen that far from being constant the fast to slow ratio varies considerably, particularly at low energies where the fast component decreases and the slow component continues to increase, quite unlike the threshold effect observed by Schoepf et al (1992). The suggested origins of the two components implies that the two processes are in some way distinguishable, as the slow

93

Pilot B
Scintillator

Window →

Sample →

Window →   Sample → e^+ Beam ←

Iron
Pole
Piece

|← 5 cm →|

L - α
PMT
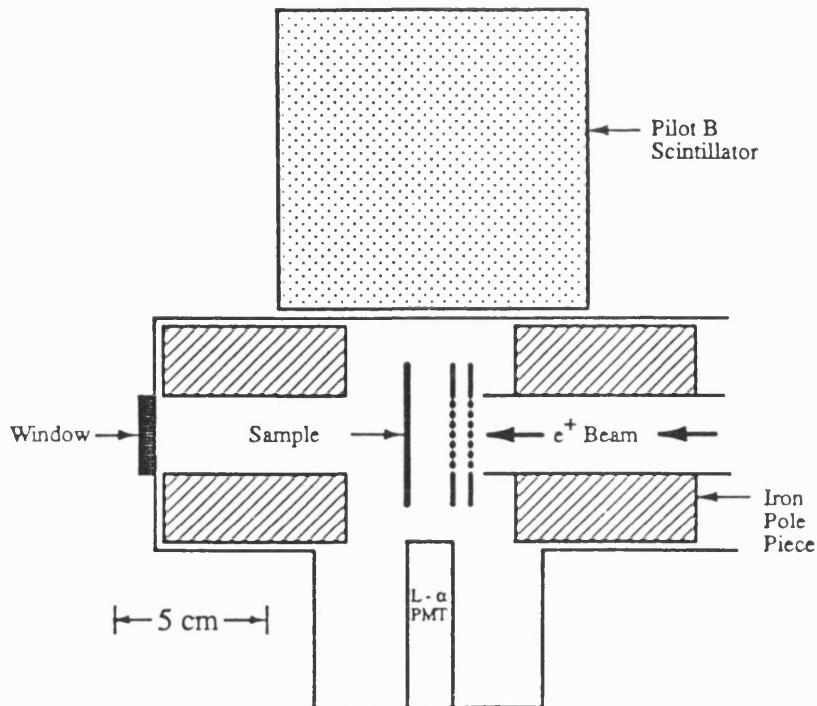
Figure 3.17 A schematic diagram of the experimental arrangement used by Steiger et al (1992).

component is attributed to Ps* formation by epithermal positrons and the fast component to formation by backscattered positrons. It is assumed that backscattered positrons are those that are ejected from the sample at energies close to that with which they were implanted, whereas epithermal positrons are those which have had their initial kinetic energy degraded in collisions within the sample, though have exited the target before thermalisation. Fig.3.20 is a composite curve depicting thermalised positrons (1), epithermal positrons (2) and backscattered positrons (3). The bold line relates to 1keV incident positrons and draws on the work of Fischer et al (1986) for regions (1) and (2), and Valkealahti and Nieminen (1983) for region (3). The dotted line is the assumed distribution for positrons incident at 50eV.

At low energies the distinction between epithermal and backscattered positrons is somewhat questionable as the epithermal distribution would be expected to extend almost to the implantation energy as here the mean free path is high and implantation depth small. In addition, most of the experimental and theoretical work concerning positron and electron backscattering has been restricted to the keV regime and above, where energy discrimination between components may be made without ambiguity, and so it may not
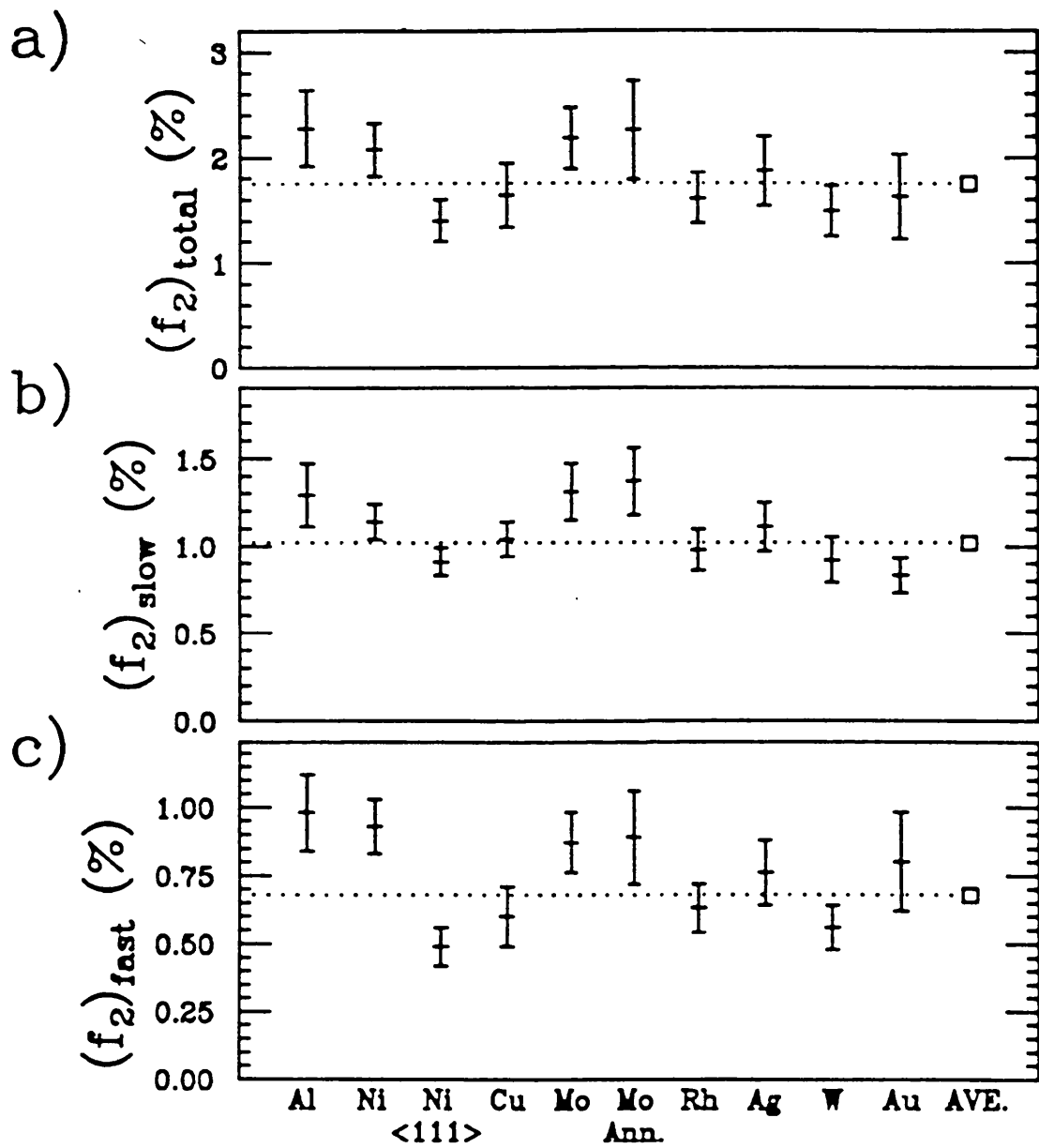
Figure 3.18 Total (a), slow (b) and fast (c) Ps* yields from a range of targets subject to positron impact at 100eV (Steiger *et al* (1992)).
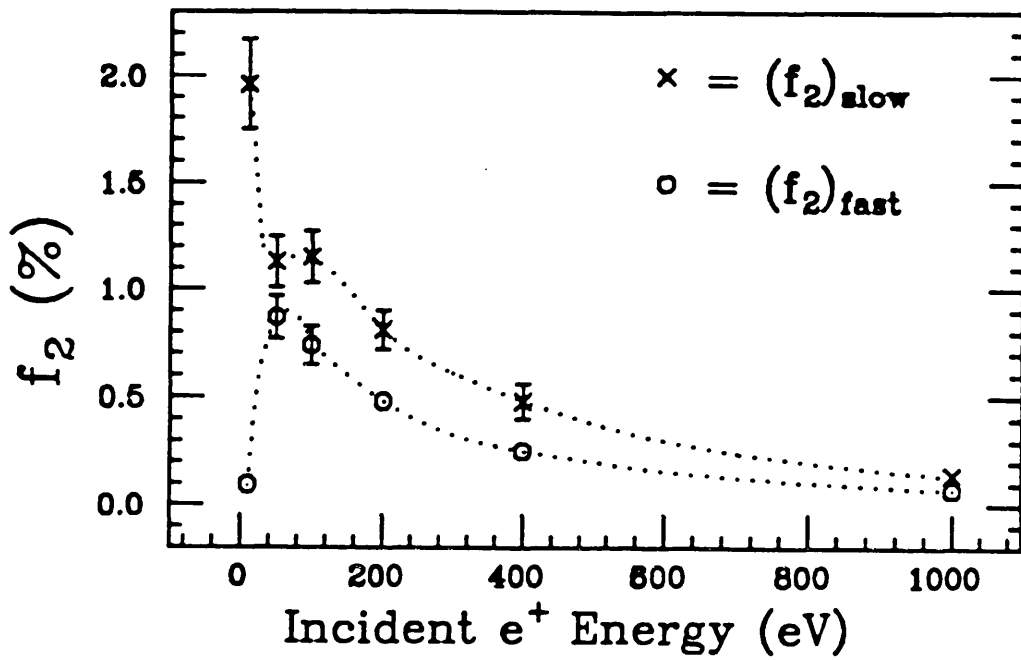
Figure 3.19 The summed fast and slow Ps* components for all targets, plotted against positron impact energy (Steiger *et al* (1992)).
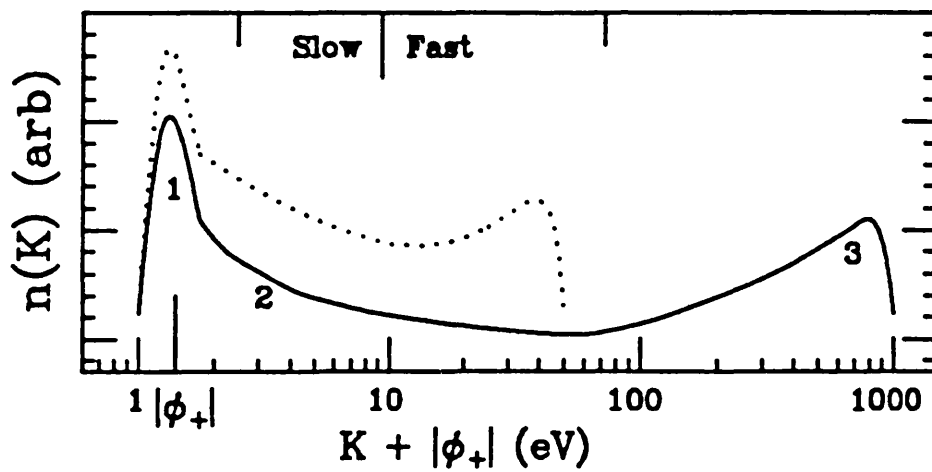
Figure 3.20 A composite curve showing the calculated energy distribution of positrons incident on a metal target at 1keV (———) and 50eV (········) and subsequently re-emitted, after Fischer *et al* (1986).

be safe to use the composite curve of fig.3.20 to extrapolate to low energies. A fuller critique of these most recent results is given in §.3.7 where they are discussed in relation to the findings of the work presented in this thesis.

3.7 The Experiment- General Layout and Principles of Operation

3.7.1 Introduction

The production of excited positronium here is achieved by transporting slow positrons electrostatically, utilising the beam as described in chapter 2, and colliding those positrons with a solid target. The Ps* is detected in the usual manner, by monitoring the Lyman-α de-excitation of the 2^3P_J-1^3S_1 transition by a suitable detector, in coincidence with a γ-ray produced on subsequent ortho-positronium decay, monitored by another dedicated device. By using the signal from the Lyman-α detector as the start signal and a detected γ-ray as the stop, a timing spectrum is obtained from which the decay rate of the de-excited Ps* may be deduced. For this work a number of targets have been used at a range of impact energies to ascertain if any Z or energy dependence may be observed in the Ps* yield. An electrostatic beam was chosen for this work to ensure that the detection efficiency and temporal response of the photomultiplier tube were not impaired by magnetic fields and also that the Ps* would be formed in a field free environment.

It has therefore been necessary to couple an electrostatic positron beam with an interaction region containing a target assembly about which are arranged u-v photon and γ-ray detectors and a facility to introduce various filters without breaking vacuum. This system is then interfaced with suitable electronics to produce the timing spectra required.

3.7.2 The Interaction Region

The target and detectors were mounted in a stainless-steel six-way spherical cross (fig.3.21), the tubular diameter of which was 150mm and spherical radius, 125mm. The target was situated close to the centre of the cross inside a 145mm diameter μ-metal tube which also acted to screen the four-element lens. The Lyman-α detector was mounted in
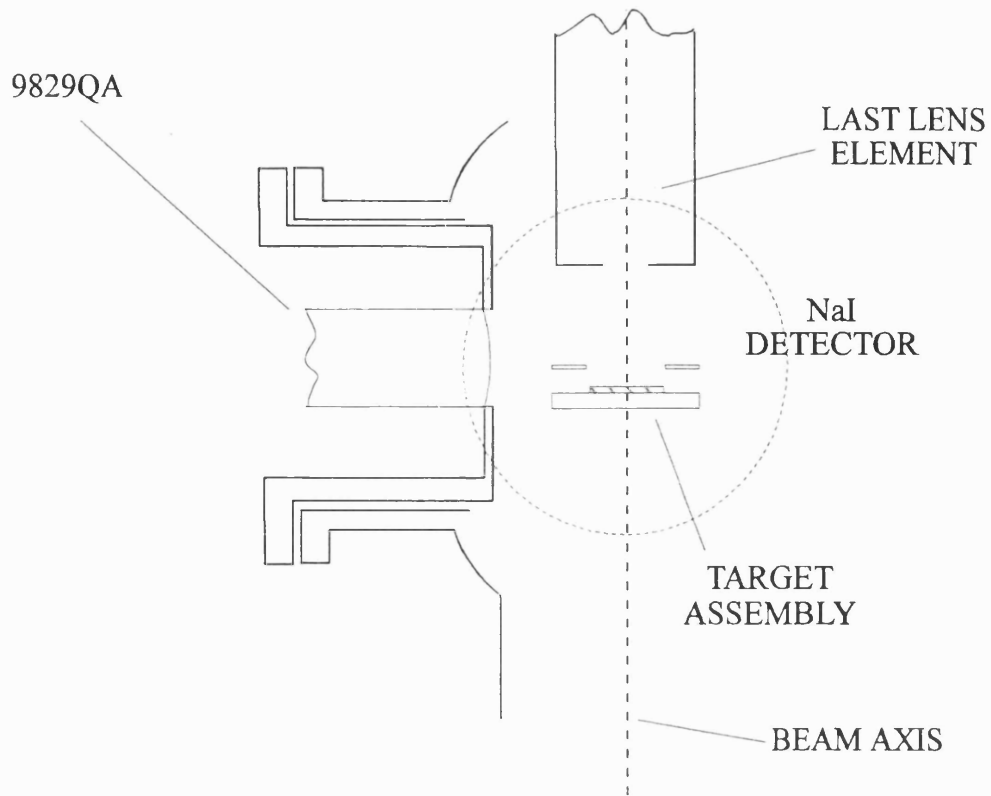
Figure 3.21 A schematic diagram of the interaction region in the Ps* production experiments.
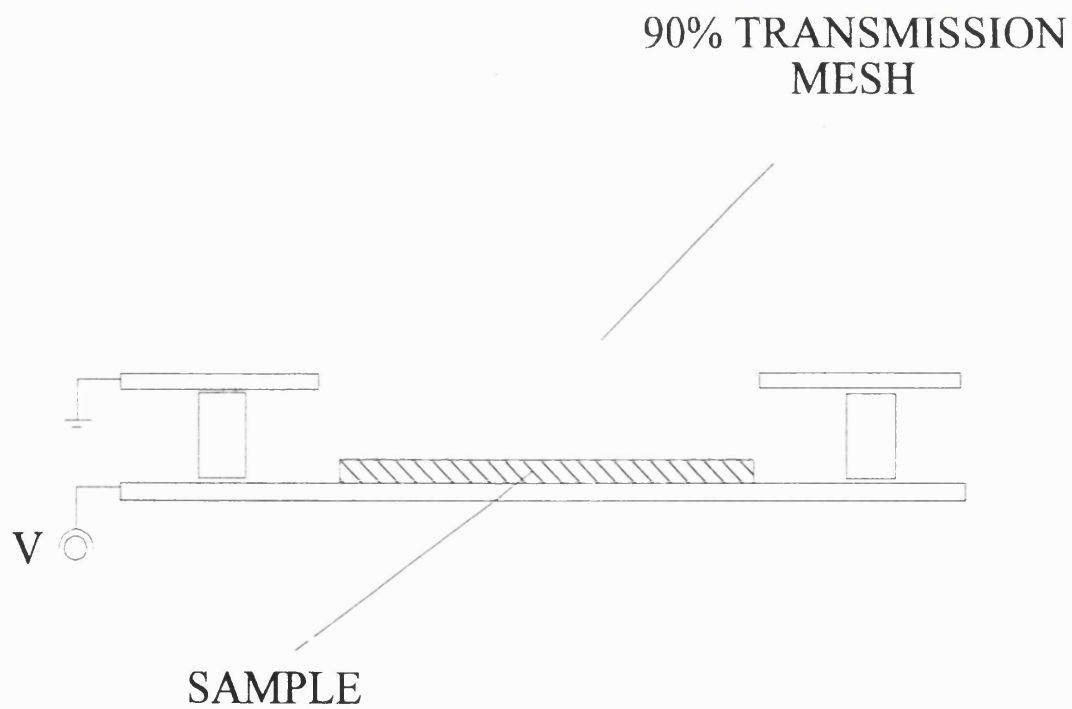
Figure 3.22 A schematic diagram of the target holder.

a stainless steel well, the base of which formed the front of a PMT housing. The PMT window interfaced with the vacuum in the chamber via a Viton O-ring. A section of the μ-metal tube was removed to allow the housing of the Lyman-α detector to be introduced close to the target from above at 90° to, and 75mm from, the beam axis. An aluminium 'top hat' fitted to one of the side ports permitted a γ-ray detector to be placed several millimetres from the μ-metal shielding, thus 75mm from the beam axis, and the opposite port was connected to a cold trap and diffusion pump to facilitate evacuation. Two linear manipulators, one off and one on axis, were mounted on the flange behind the target, and allowed various filters and slides to be introduced between the target and the Lyman-α detector without breaking the vacuum. All feedthroughs to the target and other devices to be used later were mounted on the underside flange.

3.7.3 The Target

As a number of different materials were used for this experiment the target holder, shown in fig.3.22, was designed to allow the removal and replacement of samples quickly and simply. It consisted of two discs, 80mm in diameter, one of stainless steel, 4.5mm thick, and one of copper, 1mm thick, and a 0.25mm thick stainless steel annulus with an 80mm outer and 43mm inner diameter, the open area of which was covered with a 90% transmitting copper mesh. Samples of 25mm square and up to several millimetres thick could be attached to the centre of the copper disc by copper wires which passed through four holes drilled 12.5mm from the centre in the shape of a square. Four 2.5mm threaded rods were situated at regular intervals on the perimeter of the stainless steel disc over which could be placed the copper disc and the annulus separated by ceramic bushes. The annulus was positioned 9mm in front of the copper disc, which in turn was mounted 15mm in front of the stainless steel disc. The whole arrangement was attached by a 6mm stainless steel bolt to a PTFE mounting which, by using the lens supporting rods, would allow the target to be slid to and fro along the beam axis under the Lyman-α detector.

As all three elements were electrically isolated each could be floated at different potentials. The stainless steel annulus and disc were both kept grounded at all times so as not to interfere with the incoming beam optics and the potential on the target disc was

varied depending on the required impact energy. This method was simpler than changing the transport energy which could lead to changes in the beam intensity and possibly geometry at the target.

3.7.4 The Detectors and Timing Electronics

The 243nm Lyman-α photons were detected by a Thorn EMI 9829QA photomultiplier tube. The tube was especially selected for high sensitivity at 243nm, and low dark count rate of less than 100Hz at room temperature. It had a 52mm diameter photocathode to provide a large solid angle at the target and a thin Suprasil (quartz) window which was transparent to u-v. It should be noted that using an O-ring to interface the tube with vacuum reduced the effective cathode diameter to 45mm.

The basic principle underlying PMT's is that of electron multiplication. A photon may be incident on the photocathode either in transmission, as in the 9829QA, in which case the photocathode is very thin or in reflection. In the 9829QA, the photocathode consists of a thin substrate of semiconductor grown on the inside of the quartz window upon which is deposited an overlayer of caesium and potassium. This layer reduces the electron work function of the surface and allows electrons promoted out of the valence band of the semiconductor by the absorption of a photon to escape. These electrons are then accelerated and focused onto the first in a series of dynodes by applying a fixed potential between the dynode and the cathode. The cathode may be held at ground or at a negative potential. In this case, ground was chosen to avoid perturbing the beam which was not shielded from the cathode. The dynodes are made or coated with materials which have a high secondary electron emission coefficient and each impacting electron is multiplied on average by a factor of between 4-7 depending on the interdynode potential difference. Each dynode potential is determined by a potential divider network designed for the tube and its function (fig.3.23). The cathode-first dynode potential difference is chosen for optimum focusing of the photoelectrons and so must be fixed despite the overall potential difference across the tube. This is often achieved by using Zener diodes between these electrodes. The gain of a particular tube is therefore determined by the potential difference between the first and last dynodes and the number of dynodes in the series.

100

Electrode Pin No.

k d_1 d_2 d_3 d_4 d_5 d_6 d_7 d_8 d_9 d_{10} a

3R R R R R R R R R 2R R R3 C

C_1 C_2 C_3 C_4

+HV in R2 Signal out
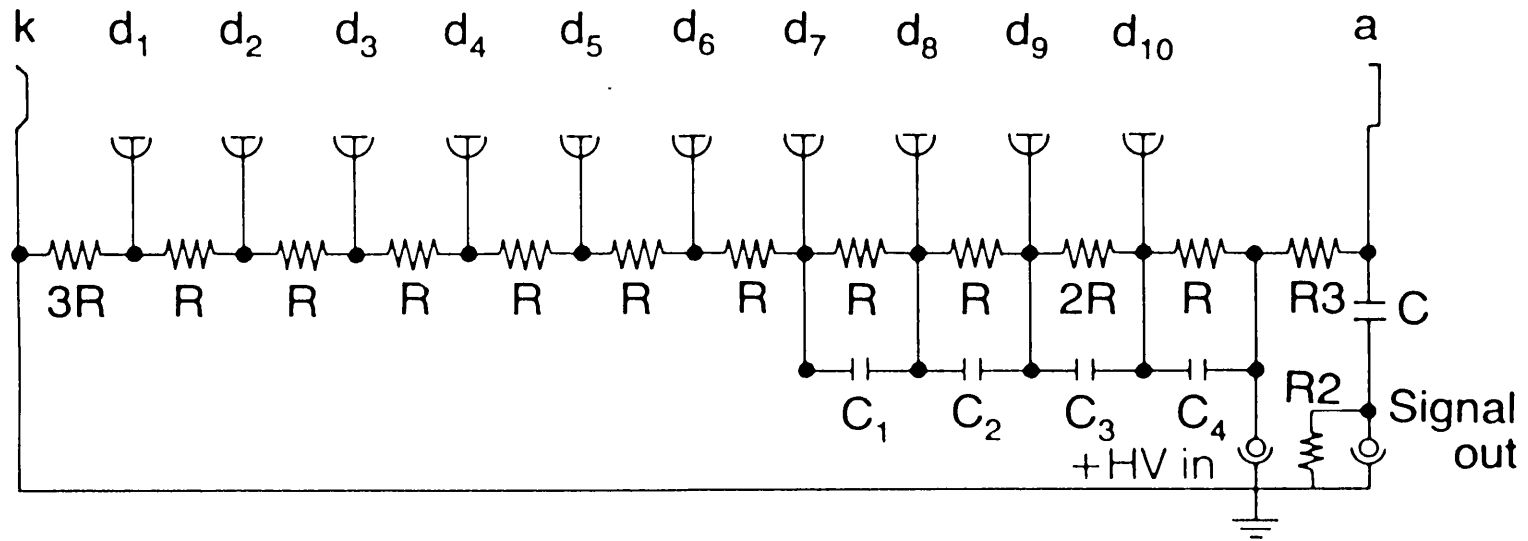
R = 470 kΩ
R2 = 10 MΩ safety resistor
R3 = 100 kΩ load resistor

C = 1000 pF (1kVW)
C_1 = 15 pF (provided by stray capacitance)
C_2 = 47 pF (100 VW)
C_3 = 150 pF (200 VW)
C_4 = 470 pF (100 VW)

Figure 3.33 A schematic diagram of the potential divider used with the EMI 9829QA photomultiplier tube.

101

START   STOP

| 9829QA (LYMAN-α) | NaI (γ-RAYS) |

TIMING FILTER AMPLIFIER

| CONSTANT FRACTION DISCRIMINATOR | CONSTANT FRACTION DISCRIMINATOR |

TIME TO PULSE HEIGHT CONVERTER

MULTICHANNEL ANALYSER AND COMPUTER
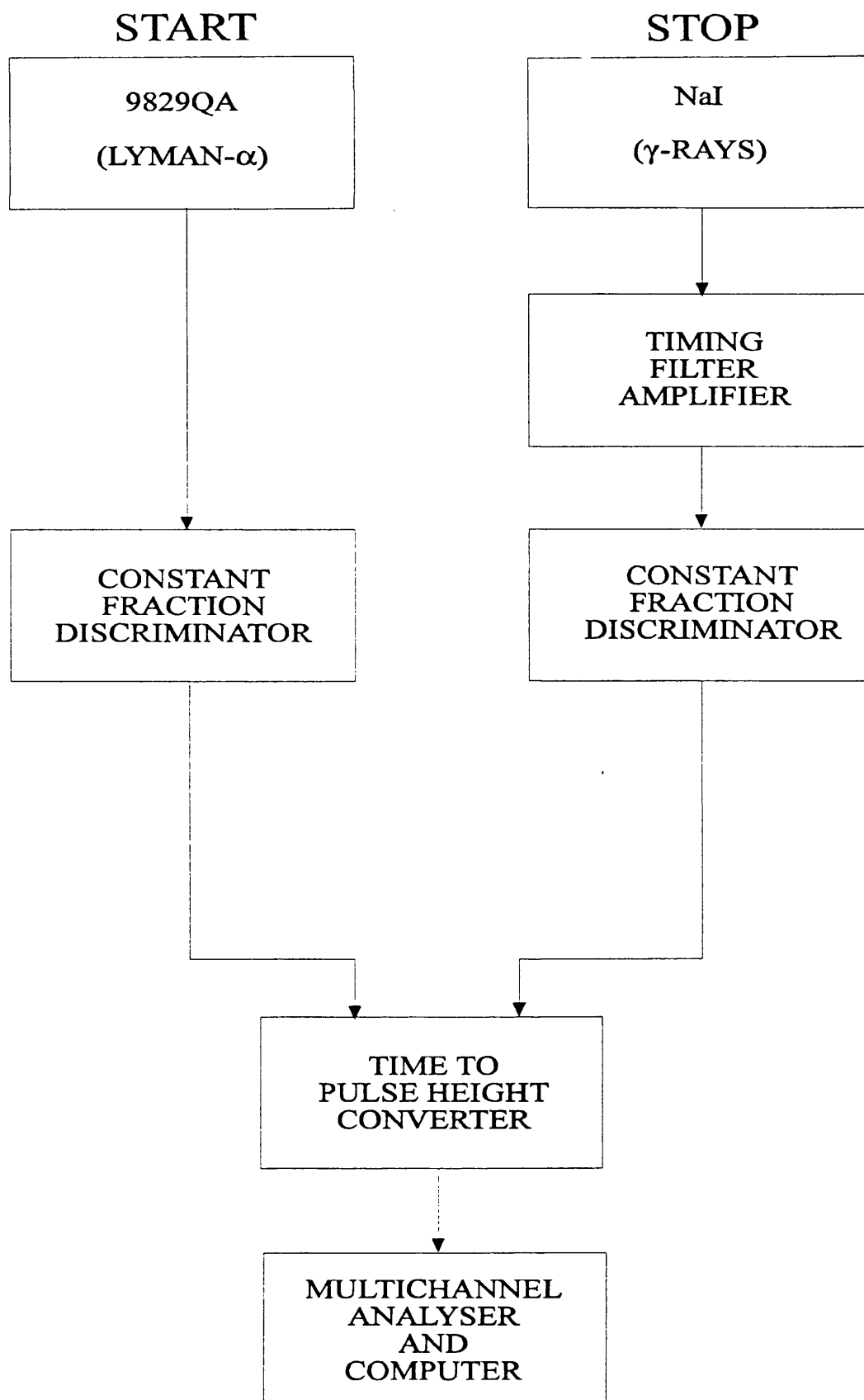
Figure 3.24 A block diagram of the timing electronics used in the Ps* production experiments.

102

The voltage applied across the PMT used in this experiment was 1900V, resulting in pulses between 10-20mV high, corresponding to pulses initiated by single photoelectrons. By coiling a copper tube around the PMT housing and passing cold water through from the mains supply, the housing and thus the cathode could be cooled to 9°C resulting in a dark count rate of 4-6Hz. The majority of the remaining counts were probably due to cosmic rays or residual radioactivity in the PMT's glass envelope.

The γ-rays were detected by using a 135mm diameter, 100mm deep, NaI crystal coupled to a RCA4522 photomultiplier tube. This crystal was used for its large solid angle and high intrinsic detection efficiency for γ-rays in the 100keV to 1MeV energy regime. The typical height of the NaI pulses was of the order of 1V though the pulses had a rather slow rise time due to the nature of the scintillation process and the large crystal size. To improve the timing resolution it was therefore necessary to pass the NaI output through a timing filter amplifier before being placed in coincidence with the Lyman-α tube. When shielded from the source, the general background the residual count rate was ~ 500Hz. The electronics used in this experiment are depicted in the block diagram shown in fig.3.24. The Lyman-α tube output was fed into an Ortec 584 Constant Fraction Discriminator, chosen for its low threshold of 5mV, thus it was unnecessary to introduce any further amplification and possibly jitter. This was then chosen as the start input to an Ortec 473A Time to Pulse Height Converter (TPHC). The NaI detector was routed through an Ortec 474 Timing Filter Amplifier to an Ortec 463 Constant Fraction Discriminator, the output of which was then fed to the stop input of the TPHC. The output of the TPHC was fed into an Ortec Maestro II Multichannel Analyser interfaced with a DECpc 222 microcomputer.

3.7.5 The Timing Spectra

The PMT was not only sensitive to visible and u-v light, γ-rays could also be detected probably by inducing scintillations in the quartz of the PMT's window. This leads to complications in the observed timing spectra as the PMT may detect light arising from events before and after positronium decay.

The timing spectra will consist of three distinct regions.

1) A prompt annihilation peak. Corresponding to the time zero of the coincidence spectra occuring:

i. when both detectors view a γ-ray or rays from the same annihilation event (o-Ps or p-Ps).

ii. when the PMT detects a true Lyman-α event, but from a de-exciting p-Ps atom. Hence the NaI will detect a γ-ray almost simultaneously due to the 125psec ground state lifetime.

2) A distribution corresponding to negative times (to the left of the prompt peak). These events are initiated by a γ-ray detected by the NaI in coincidence with a delayed scintillation induced by that same γ-ray, or positron that led to it, in some part of the apparatus. It should be noted here that many materials have very long decay times when excited in this way (Marshall (1988)).

3) A distribution at positive times (to the right of the prompt peak) produced by:

i. A true Lyman-α event detected in coincidence with a delayed γ-ray from o-Ps decay. In an ideal situation, ie where no pick-off or geometrical losses occur, this true Ps* signal should consist of a single exponential with a 142nsec decay constant. However, due to the loss mechanisms cited, this is not normally the situation.

ii. A target scintillation on particle impact in coincidence with a delayed γ-ray from o-Ps decay by an atom formed by the same scintillating particle.

To unambiguously confirm Ps* production, it was necessary to perform a number of tests. The observed timing spectra are rather complicated. The open circles in fig.3.25, a typical example, is the coincidence spectrum for positrons incident on copper at 100eV. Only the t > 0 regime is of any interest and by avoiding the prompt peak, only 3)ii. may lead to ambiguities in Ps* detection. At low impact energies, target scintillations
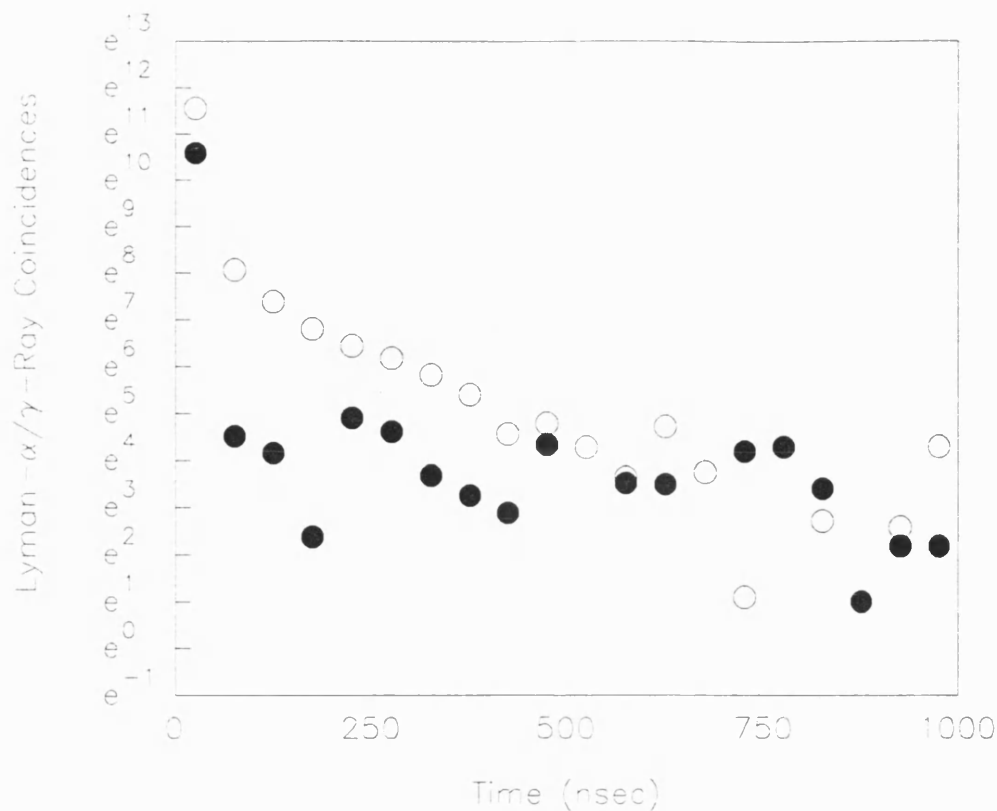
Figure 3.25 Lyman-α/γ-ray coincidence spectra for 100eV positrons incident on a Cu target with borosilicate slide in ($\bullet$) and out ($\bigcirc$).

would not be expected to present a serious problem. To test this assumption a borosilicate slide, which was opaque to wavelengths less than 290nm, was placed in front of the photocathode of the PMT in order to confirm that the signal in the $t > 0$ was in the u-v region. The closed circles in fig.3.25 is another copper run at 100eV though this time with the borosilicate slide in place. The delayed signal has clearly disappeared, thus confirming that visible light was not responsible for any of the delayed signal. Note, however, the increased coincidences in the $t < 0$ region due to γ-rays scintillating in the glass. Finally, introducing filters at the Lyman-α wavelength and at a wavelength somewhat longer, the contribution from scintillations in the u-v region to the delayed signal, which would be expected to be similar at both wavelengths, could be examined.

The two filters used were Andover Corporation 50mm diameter interference filters centred on the wavelengths of 240nm and 280nm. Their transmission as a function of wavelength is shown in fig.3.26, where it can be seen that peak transmissions are at best only 15% with a FWHM of $\approx$ 11nm in both cases. Interference filters are sensitive to the

angle of incidence, θ_i, of the light, given by eqn.3.14,

$$\lambda_{\theta_i} = \lambda_0 \left[1 - \left(\frac{1}{N^*} \right)^2 \sin^2\theta_i \right]^{\frac{1}{2}}$$ (3.14)

where λ_0 and λ_θ are the wavelength at normal incidence and the effective wavelength at an angle θ_i respectively and N^* is the effective refractive index of the filter. Using fig.3.26 and eqn.3.14, it can be seen that a significant fraction of the available Lyman-α signal will be undetectable, particularly for light with an angle of incidence above $10°$ at which the transmission is reduced to less than 7%, and for any angle above $15°$, a 243nm photon would not be transmitted at all. The filters subtend an angle of approximately $30°$ at the target, therefore it is possible that a significant fraction of the Ps^* will be undetectable above that due to the 85% attenuation at normal incidence.

Using eqn.3.15, the Doppler wavelength shift may also be considered,

$$\Delta\lambda = \lambda_0 \left(1 - \sqrt{\frac{c \pm \left(\frac{E_{kin}}{m_0} \right)^{\frac{1}{2}}}{c \mp \left(\frac{E_{kin}}{m_0} \right)^{\frac{1}{2}}}} \right)$$ (3.15)

where $\Delta\lambda$ is the wavelength shift, λ_0 is the wavelength in the rest frame, E_{kin} is the positronium kinetic energy, m_e is the electron/positron mass and c is the speed of light. At 10eV, the wavelength shift is $\sim \pm 1$nm and at 50eV, $\sim \pm 2$nm, and with reference to fig.3.26, it can be seen that some signal, up to 3%, could indeed be lost to Doppler shifting.

From the discussion above, one may conclude that the overall efficiencies of the filters would be considerably lower than the peak values quoted in the data sheets, though an absolute figure is difficult to calculate without a more complete knowledge of the position, velocity and angular distribution of the Ps^* as it de-excites.
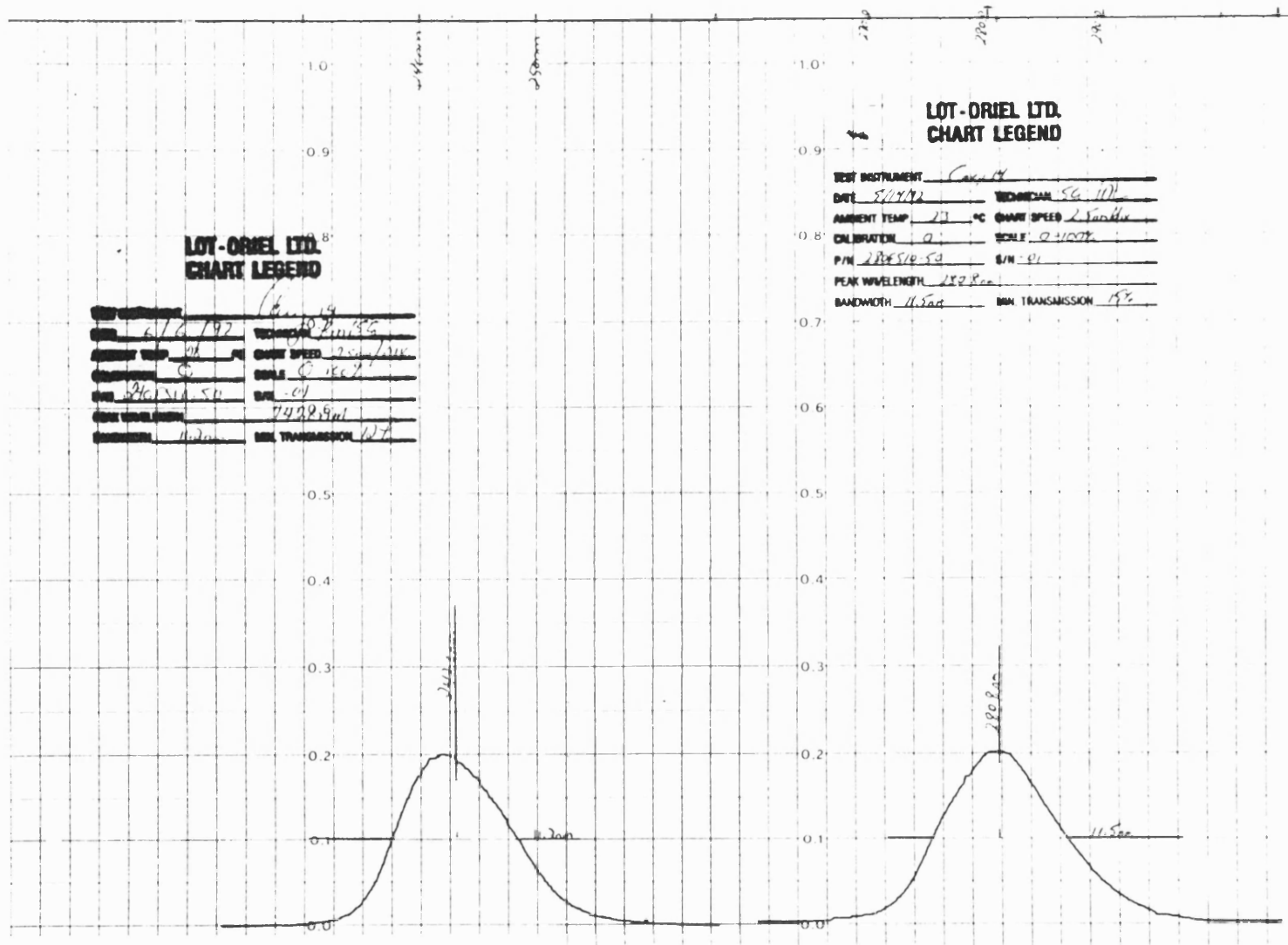
Figure 3.26 The measured optical properties of the 240nm filter (left) and the 280nm filter (right).
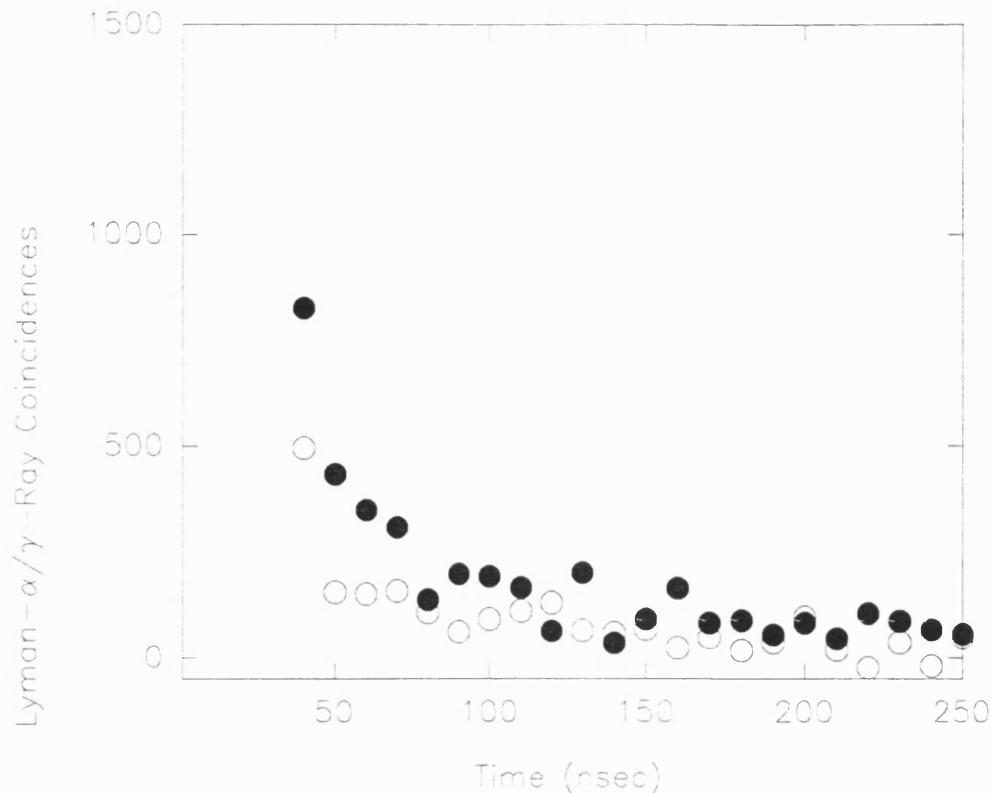
Figure 3.27 Lyman-α/γ-ray coincidence spectra for 100eV positrons incident on a Cu target with 240nm filter in position ($\bullet$), and replaced with 280nm filter ($\bigcirc$).

Fig.3.27 shows two copper target runs where a different filter was used in each case. One can clearly see the enhanced region to the right of the prompt peak in the 243nm filter case, although the signal was reduced by at least an order of magnitude by the limited transmission of the 243nm filter. As a result of these tests it was proved conclusively that Ps* was responsible for the delayed coincidences, and all subsequent runs were performed without the filters in place to avoid unnecessary signal loss.

3.7 Results & Discussion

Once the production of Ps* was confirmed, a series of targets were subjected to positron bombardment at energies ranging from 10-500eV. The targets selected were beryllium, copper and gold. These metals were chosen for their range of atomic number. A disused plate from a channel-plate electron multiplier was also used to determine its effectiveness as a target.
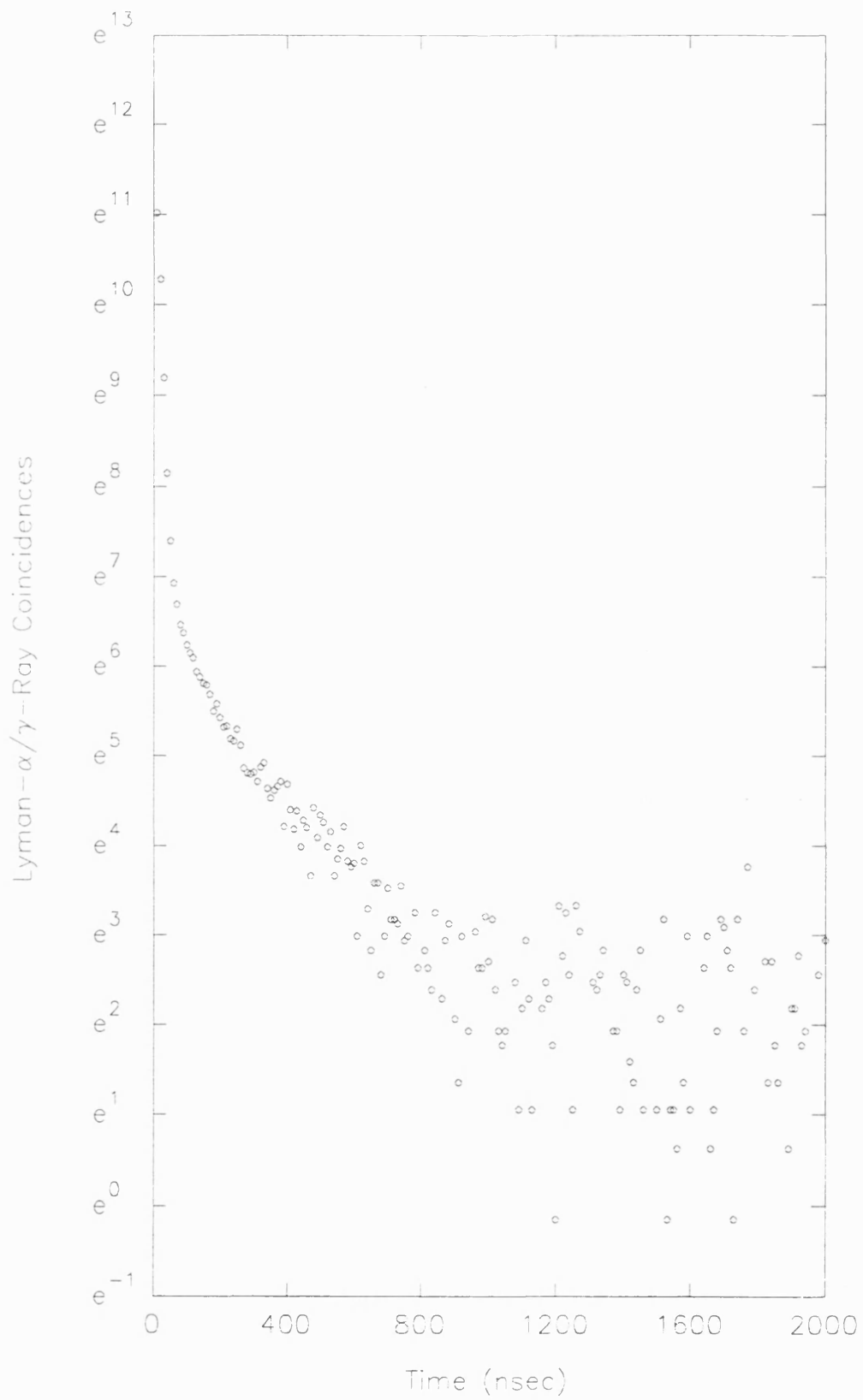
Figure 3.28 An example of a typical coincidence spectrum, in this case 100eV positrons incident on Be. The data have been summed into ten channel bins and the background has been removed.
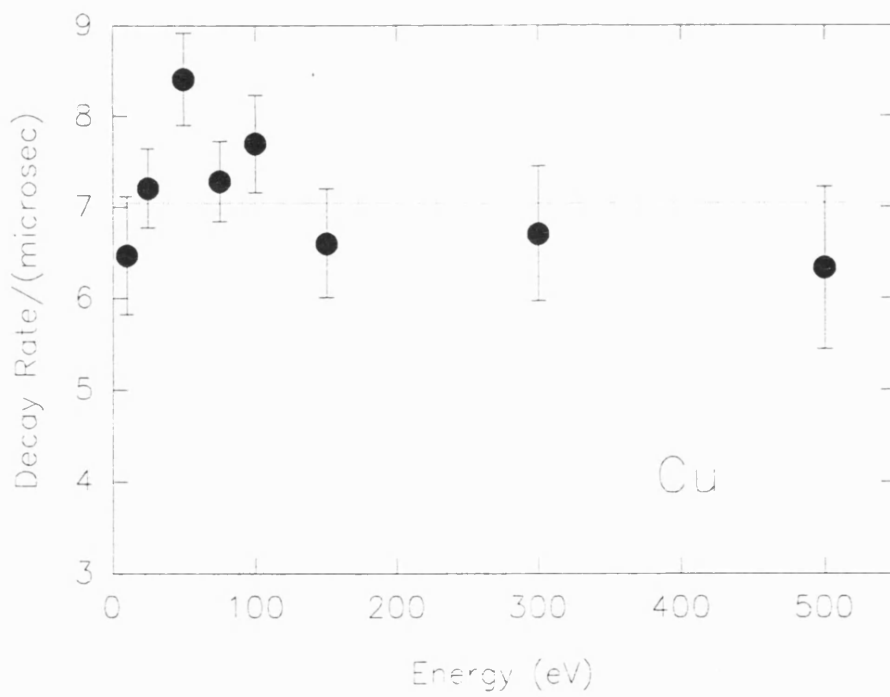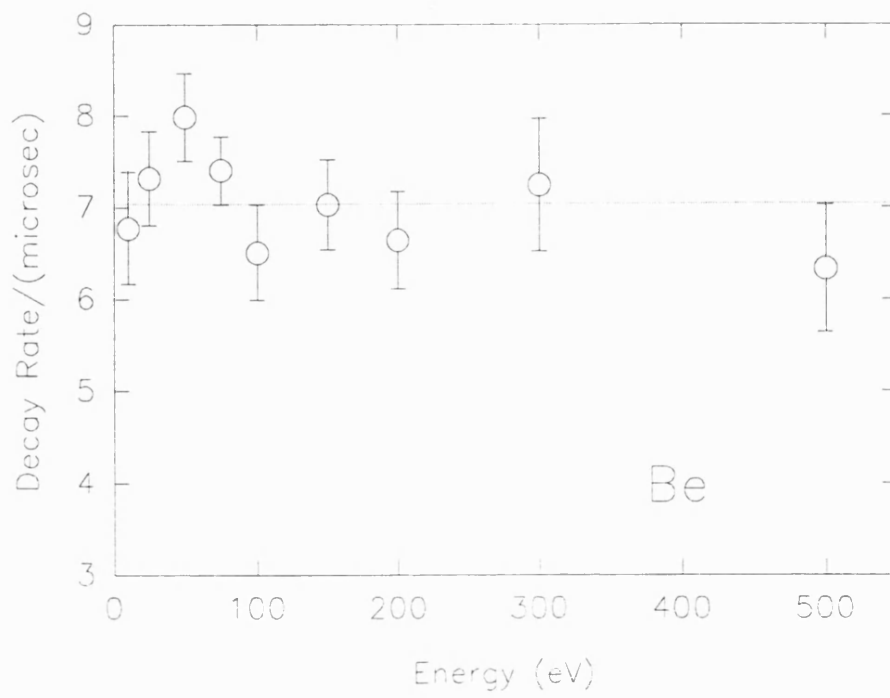
Figure 3.29 A plot of the fitted decay rates against energy for positrons incident on a Be target (top) and a Cu target (bottom). The dotted line represents the $7.04\mu sec^{-1}$ o-Ps vacuum decay rate.

110

The spectra, once collected, were imported into the spreadsheet software program, Sigmaplot (Microsoft, 1991). Here the background could be removed and, using the program's in-built fitting routines, decay-rates estimated. Fig.3.28 is an example of the spectra with the background removed. Due to the broad nature of the prompt peak, the fit was started 150nsec from time zero. Fig.3.29 is a plot of the fitted decay rates against energy for both targets. In all cases the delayed regions were composed of an exponential with a decay rate close to the accepted o-Ps vacuum lifetime against annihilation of $(7.0482\pm0.0016)\mu\mathrm{sec}^{-1}$ (Nico et al (1992)), indicated by the horizontal dotted line. When this 'slow' component was subtracted a non-exponential, 'fast' component at shorter times was revealed, close to the prompt peak.

Two possible explanations for the fast component are suggested. Firstly, that a portion of the Ps* formed had a kinetic energy in excess of 6.8eV and was being ionised, in collisions with the walls or lens elements and the resulting free positrons rapidly annihilating. The second explanation is that of disappearance. After de-excitation, Ps will continue moving with close to its original velocity, as momentum transfer is small, until the Ps undergoes natural decay or is quenched in a wall collision.

$$d\approx0.06(\mathrm{E}_{kin})^{\frac{1}{2}} \qquad\qquad (3.16)$$

Eqn.3.16 gives the relationship between the distance travelled by a Ps atom, d (in metres), for a Ps atom with kinetic energy E_{kin} (in eV). Ps atoms with a kinetic energy below 6.8eV may experience many wall collisions (Hasbach et al (1987)), and thus in the open geometry used in this experiment it is possible that the Ps once in the ground state, may move into a region of low detection efficiency before decaying.

Two components were found in all spectra, and, indeed, the shape of the spectra was found to be the same regardless of impact energy, as can be seen in fig.3.30. This is a composite plot of Be target runs at 25eV and 300eV, although the overall number of counts changed. Fig.3.31 is a plot of the ratio of Ps* counts in the 50-
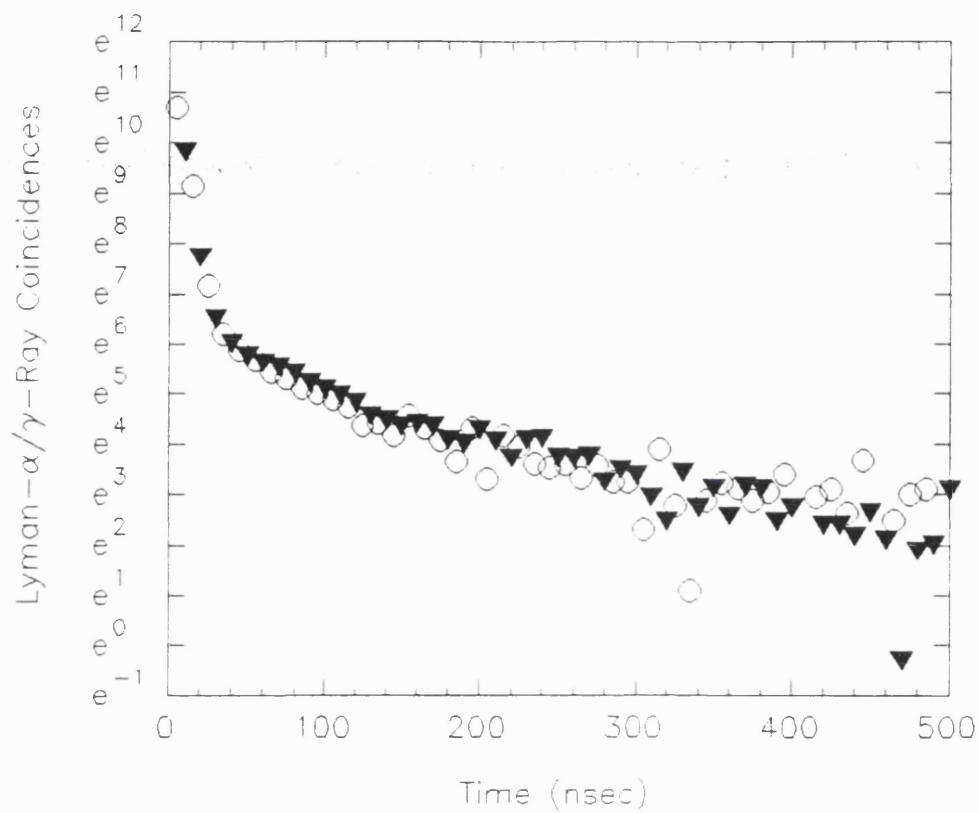
Figure 3.30 A composite plot of the coincidence spectra obtained from positrons incident on Be at 25eV (O) and 300eV (▼).
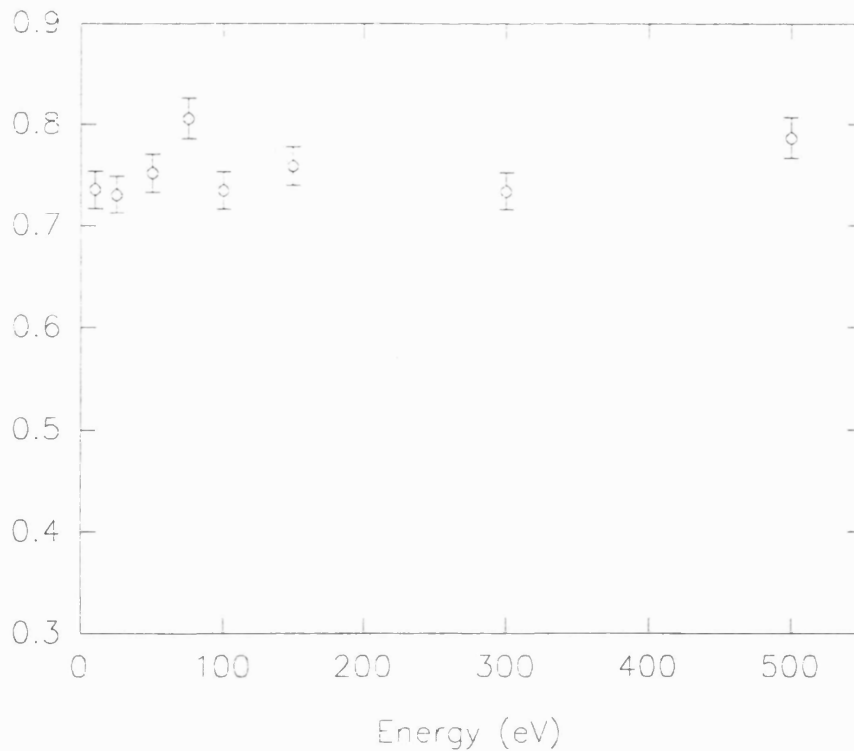
Figure 3.31 The ratio of integrated counts in the 50-100nsec to the 100-1000nsec time regions, as a function of energy for positrons incident on the Be target.

100nsec to 100-1000nsec time regions as a function of incident positron energy on the beryllium target. If the relative strengths of these components were to change, it would indicate an energy dependence in the formation of each component. However, the ratio can be seen to be constant and it is therefore believed that the origin of these two components lies not in distinct populations of fast and slow Ps*, but is related to a geometrical dependence in the NaI detection efficiency.

It was not possible to fit to this fast component as it could not be sufficiently separated from the prompt peak, however the yield of Ps* in this component has been estimated to give a total yield for each target. These relative Ps* yields were found by integrating over the delayed signal, normalising for runtimes and correcting for source decay as the experiment was performed over a period commensurate with the 71 day half-life of the ^{58}Co positron source.

To obtain absolute values for the Ps* yield, it was necessary to account for the solid angles of the detectors and intrinsic detector efficiencies. The NaI total detection efficiency for 2-γ decay was measured by placing it in coincidence with a pair of channel plates as in the method described in chapter 2 §.2.10, and was found to be 13%. It was assumed that the detection efficiency of 3-γ decay was simply 3/2 times that for 2-γ decay, allowing for the wide discriminator window used and the average photon energy of 330keV from 3-γ annihilation (Ore and Powell (1949)). The PMT's intrinsic detection efficiency, or quantum efficiency, at the 243nm wavelength was given by the manufacturer as 22.5%. Assuming that the Ps* radiatively decays close to the target and beam axis, not unrealistic as Ps* with a kinetic energy of even 100eV would travel only 1cm in the 3nsec lifetime of the transition, the solid angle of the PMT window to the target is dependent on the distance of the tube from the beam axis and the window diameter and estimated to be 3.4%. Finally, as the 2^3P_J represent only 9/16 of the possible n=2 states and assuming that the Ps* is equally distributed among all states, the inverse of the product of these efficiencies must be multiplied by 16/9, giving a correction factor of 1.2×10^3 which, when applied to the data, results in the absolute efficiencies shown in fig.3.32.
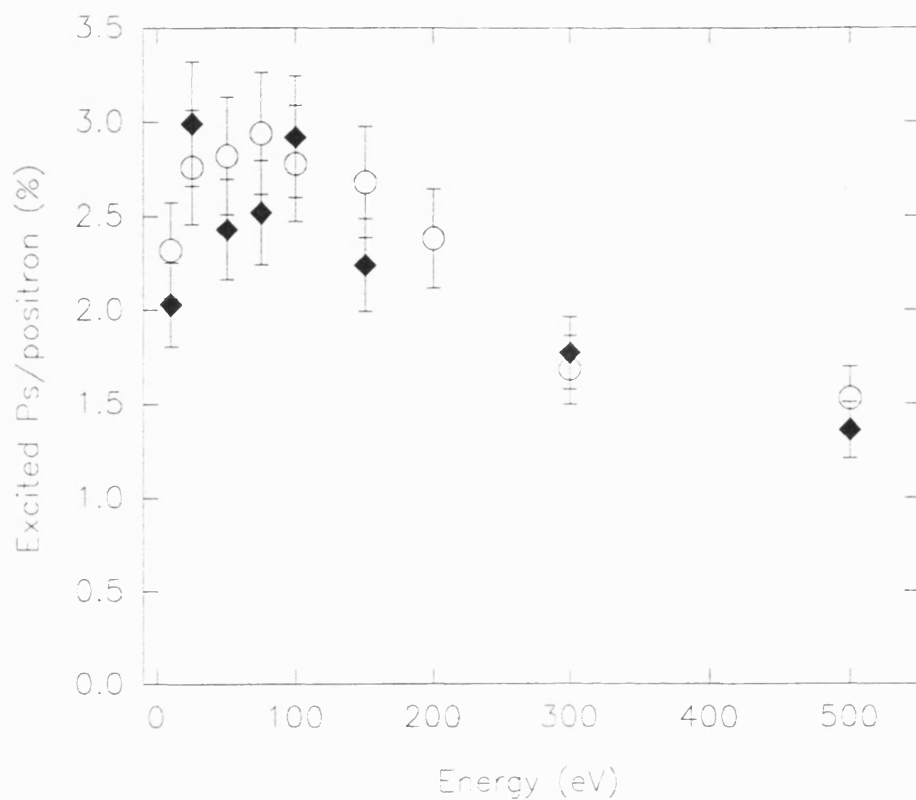
Figure 3.32 Absolute Ps* yields as a function of energy for positrons incident on Be (◆) and Cu (○) targets. The error bars are statistical only.
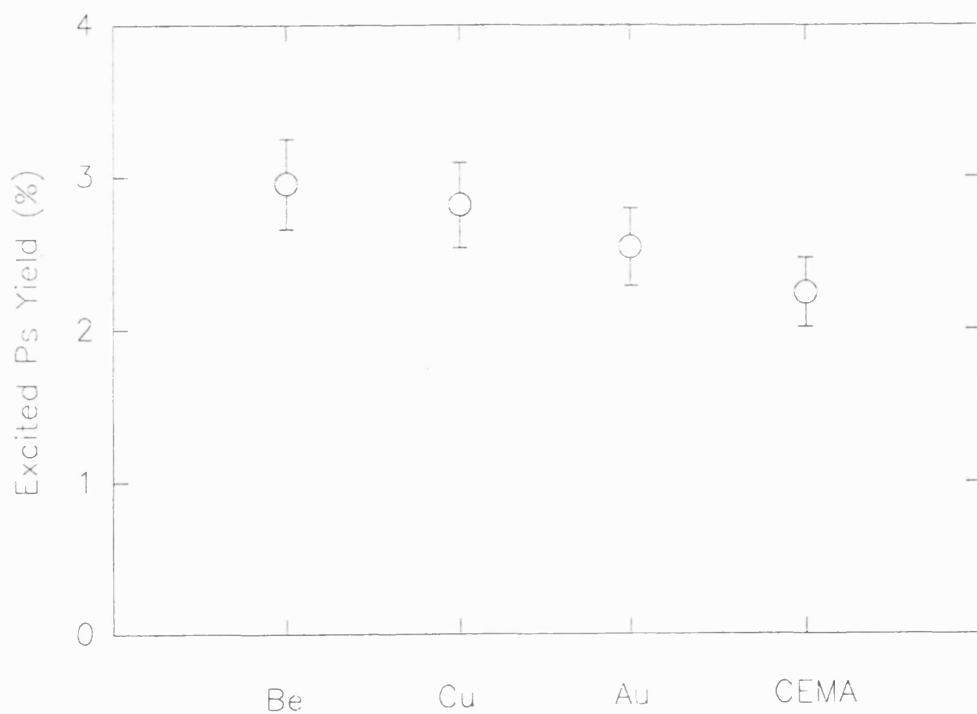
Figure 3.33 Relative Ps* yields for 100eV positrons incident on: Be, Cu, Au and a channel plate.

114

As can be seen from fig.3.32, there is a clear dependence of the Ps* yield with energy, the highest yield being $\sim 3\%$ at around 75eV. The Ps* yield drops rapidly as the e^+ input energy decreases in accordance with the measurements of Schoepf *et al* (1992), but at odds with the findings of Steiger *et al* (1992) who find no fall off in yield at low energies. There is no evidence of a Z effect in the Be and Cu data. To further test this result a gold target was used and subjected to 100eV positron bombardment. Fig.3.33 is a plot of the relative Ps* yield from Be, Cu and Au targets all for positrons with an impact energy of 100eV. In addition, the yield from a disused plate from a CEMA is also shown. With the exception of the channel-plate, there is little appreciable difference in yield between the samples, thus confirming the Be and Cu results. The low yield from the channel-plate may be understood when one considers the surface presented by such a target to an incoming positron. As the plate largely consists of pitched channels, a positron is likely to enter one of these channels whereupon it may form Ps*. However, to be detected, the atom must then make its way back out of the channel and then de-excite within the field of view of the Lyman-α detector, without first quenching at the channel walls. It can be seen, therefore, that in order to do this, the Ps* must be formed outside or close to the entrance of a channel and that its subsequent motion will take it in the required direction. The net result being a reduced Ps* yield from such targets.

As discussed above recent studies of sputtered targets in UHV conditions have yielded a Z dependence similar to that exhibited in ground-state Ps formation by backscattered positrons, though it should be stressed that only two materials were examined. For untreated samples however, this and recent work suggests little or no Z dependence at all. The difference observed can be understood if one considers the Ps* formation process. For a clean surface, an incoming low energy positron (50eV) may penetrate a few Å, be backscattered out of the material, and on passing through the surface liberate an electron and thus form Ps*. At these low energies the fraction of Ps* would be expected to rise with a reduction in Z as the likelihood of escape from the bulk would be higher in lower density materials. As the incident energy is increased, the implantation depth increases and the likelihood of escape decreases, thus the Ps*

115

would also be expected to decrease. As the implantation depth is inversely proportional to Z, this decrease in yield will be more pronounced for low Z materials.

For untreated samples, low energy positrons do not penetrate through the overlayer of contaminants, and thus the target acts as a substrate for the overlayer. As a result any change in Z will have little or no effect on Ps* yield. As the incident energy is increased the positrons will just be implanted deeper into the overlayer. Possibly at some energy positrons will pass through the overlayer and into the material below and thus experience the character of that target, though the effect, if any, on Ps* yields requires more knowledge of the thickness and composition of contaminants before one may speculate on such processes.

In order to test these hypotheses, the gold sample was again subjected to positron bombardment, but this time in a magnetically guided system. The fraction of re-emitted positrons returned to the surface by a retarding potential was measured as a function of beam energy and retarding voltage. Fig.3.34 shows positrons incident at 25eV, 100eV and 250eV. In all cases all positrons would appear to be returned by a maximum voltage of 10eV, thus implying that the majority of the epithermal positrons have a energy of 10eV or lower. Finally the yield of positrons with an energy of 15eV or lower was measured as a function of energy. Fig.3.35 shows this data, superimposed on the measured Ps* from Be yield as a function of energy. It is interesting to note the reasonable agreement of the two curves, particularly the position of the peak in both sets of data between 50eV and 100eV. Such an agreement would be expected if these positrons are the source of the Ps*.

In this work, as in that of Steiger *et al* (1992) and Schoepf *et al* (1992), two components were observed in all spectra. In this work however, it is believed that the second component does not necessarily imply a distinct velocity regime, but rather reflects the dependence of the detection efficiency of the NaI detector on the geometry of the experiment. The Schoepf *et al* (1992) experiment, in particular, would appear
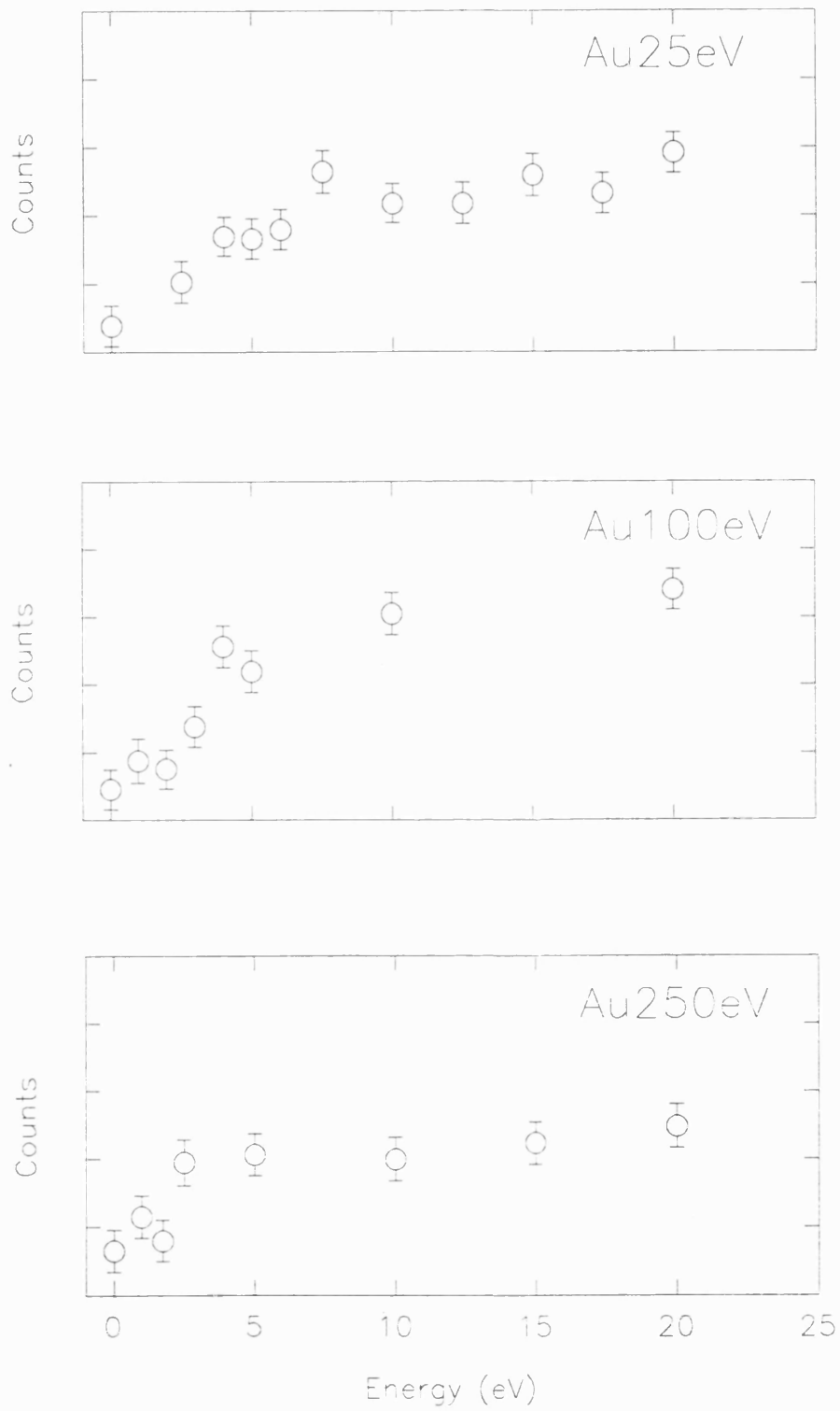
Figure 3.34 Re-emitted positron retardation spectra for positrons incident on a Au target at 25eV, 100eV and 250eV.

117
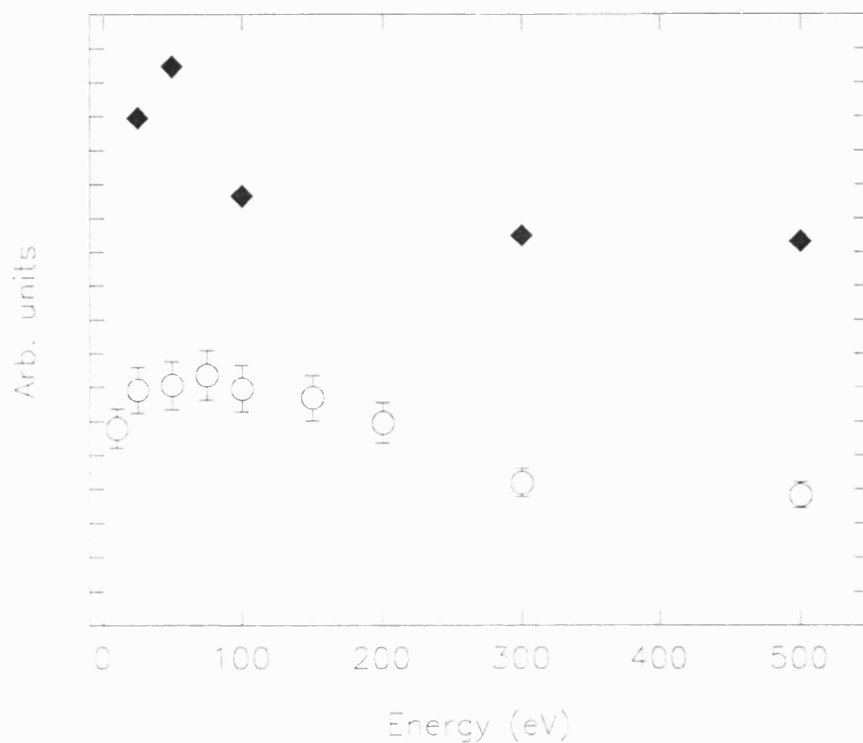
Figure 3.35 The relative yield of positrons re-emitted from a Au target with energies $\leq 15\text{eV}$, as a function of incident positron energy ($\blacklozenge$). The relative Ps* yield as a function of energy, for positrons incident on a Cu target ($\bigcirc$).

to have a geometry in which the detection of the Ps* may be highly dependent on the positronium velocity, thus possibly explaining why the measured Ps* yields are so much lower than those of Steiger *et al* (1992). It is also the case that extreme care is necessary when using retarding analysers for positron selection in purely electrostatic fields, as any angular divergence in the beam will be exaggerated. Fig.3.36 is a computer simulation of positrons with an initial energy of 100eV and divergence of $10°$ being subjected to retardation to 10eV at the target while in a purely electrostatic field. Distortion of a beam profile to this extent will clearly have an effect on the effective solid angle of both the NaI and Lyman-α detectors. In addition, if bare positrons are re-emitted, they may be accelerated away by the retarding potential to strike another part of the target mount, and possibly form Ps*. The effect on the disappearance rate and thus the spectrum shape, would depend on exactly where the positronium was formed and the geometry of the experiment. Such an effect may go some way to explain the behaviour at low energies of the Ps* fractions in the work of Steiger *et al* (1992), in particular the sharp rise in the slow Ps* yield as the positron

118
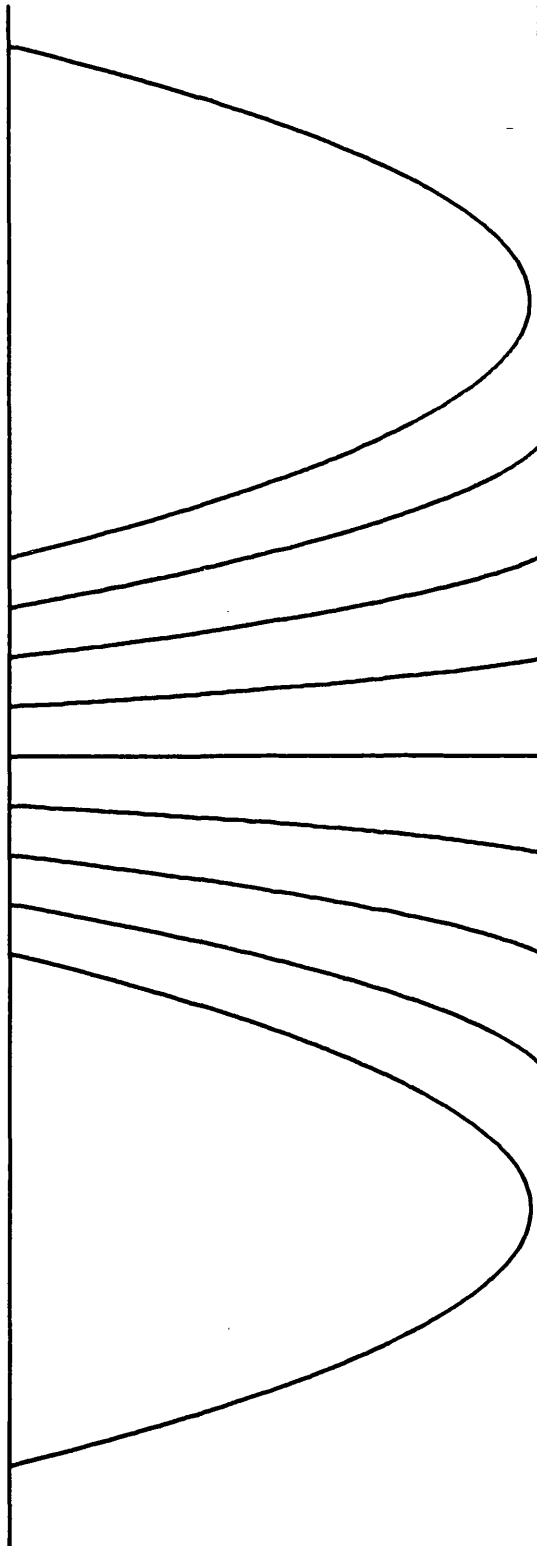
Figure 3.36 SIMION simulation of 100eV positrons with angular deviations of up to 20° (in steps of 5°), subject to retardation to 10eV at a target.

119

energy decreases, which is contrary to the results of Schoepf *et al* (1992), the yields observed in this work and the low energy positron backscattering results given above. Finally it is interesting to note that these discrepancies in the behaviour of the fast to slow ratio in the work of Steiger *et al* (1992) and Schoepf *et al* (1992) disappear when the beam is not subject to retardation.

CHAPTER 4

THE RADIATIVE LIFETIME OF THE 2P-1S TRANSITION
IN POSITRONIUM

4.1 Introduction-The Atomic Structure of Positronium

Positronium, as a purely leptonic atom provides an ideal subject for study, along with muonium (μ^+e^-), of the two-body formalism of Schwinger (1951) and Salpeter and Bethe (1951). Measurements also hold implications for non-leptonic systems as the relativistic bound-state formalism used in calculating the $n=2$ Ps fine structure, bears similarities to QCD calculations of quark-antiquark bound states.

Using non-relativistic atomic theory, the gross structure of Ps may be simply deduced by first considering the energy levels of atomic hydrogen given by eqn.4.1,

$$E_n(H) = - \frac{\pi e^4}{2\epsilon_0^2 n^2 \hbar^2} \cdot \frac{m_0 m_p}{m_0 + m_p} \qquad (4.1)$$

where m_p is the proton rest mass of 1.673×10^{-27}kg, and e is the electronic charge, 1.602×10^{-19}C. The reduced mass in hydrogen is $\simeq m_0$, and as the proton is so massive in comparison to the electron it may be considered to be at rest with the electron orbiting around it. In the case of positronium however, both the electron and positron masses are equal and thus the particles orbit about their mutual centre of mass with a reduced mass of $m_0/2$. This leads to a reduction in the Ps energy levels by a factor of 2, and so the Ps gross structure is given by,

$$E_n(Ps) = \frac{E_n(H)}{2} \simeq \frac{6.8}{n^2} eV \qquad (4.2)$$

As the binding energies in Ps are half those in H, it follows that the Bohr orbits of

121

positronium will be twice those of hydrogen. The radiative lifetimes, τ, of the excited states of positronium will therefore also be twice those of hydrogen since,

$$\tau \propto E_n^{-3} \cdot r_n^{-2} \qquad (4.3)$$

for dipole transitions, where E is the binding energy and r is the Bohr radius.

While the gross structure of the positronium atom is much like that of hydrogen, apart from simple scaling, major changes to the hyperfine and fine structure occur as a result of the differences between the proton and positron, namely:

(1) the large magnetic moment of the positron, equal to that of the electron, is approximately 657 times larger than that of the proton, μ_p;

(2) a relativistic orbit-orbit interaction not significant in the case of a slow moving proton;

(3) a spin dependent interaction arising from virtual pair annihilation and creation, not possible for a bound electron-proton pair.

Fig.4.1 shows the energy levels of hydrogen and positronium in the ground and first excited states. It can be seen that the clear distinction between fine and hyperfine levels, as seen in hydrogen, are not applicable to positronium. For example the Ps hyperfine splittings are two orders of magnitude greater than those of hydrogen, largely due to the positron magnetic moment. There are also more available sub-states as the possible spin arrangements of the positron and electron lead to additional values of the total angular momentum. While positronium shares some of the nomenclature of a two electron atom, its structure cannot be directly compared with an atom such as helium. All positronium states can either be triplets where the total spin is equal to one, or singlets where the total spin is zero. Either the positron or electron may be considered to be the nucleus and so in positronium physics the prefixes ortho and para refer to the electron/positron spin relative to the 'nucleus'. In any other atom this would be a hyperfine effect. By comparison, in helium the ortho and para states refer to the spins of the two electrons
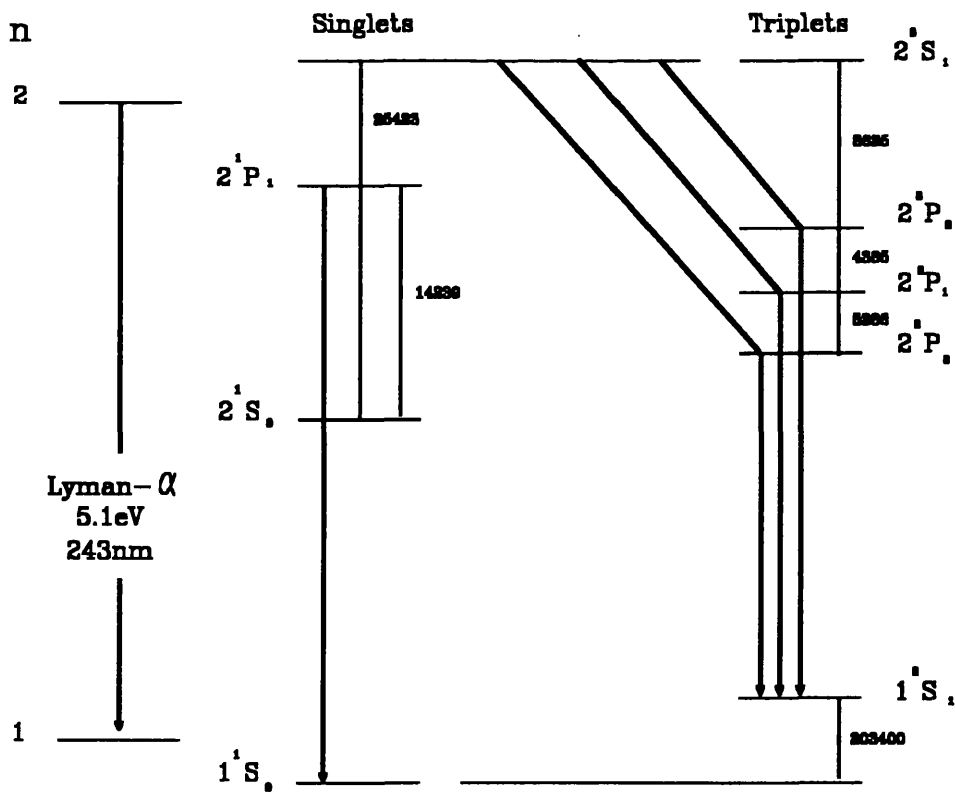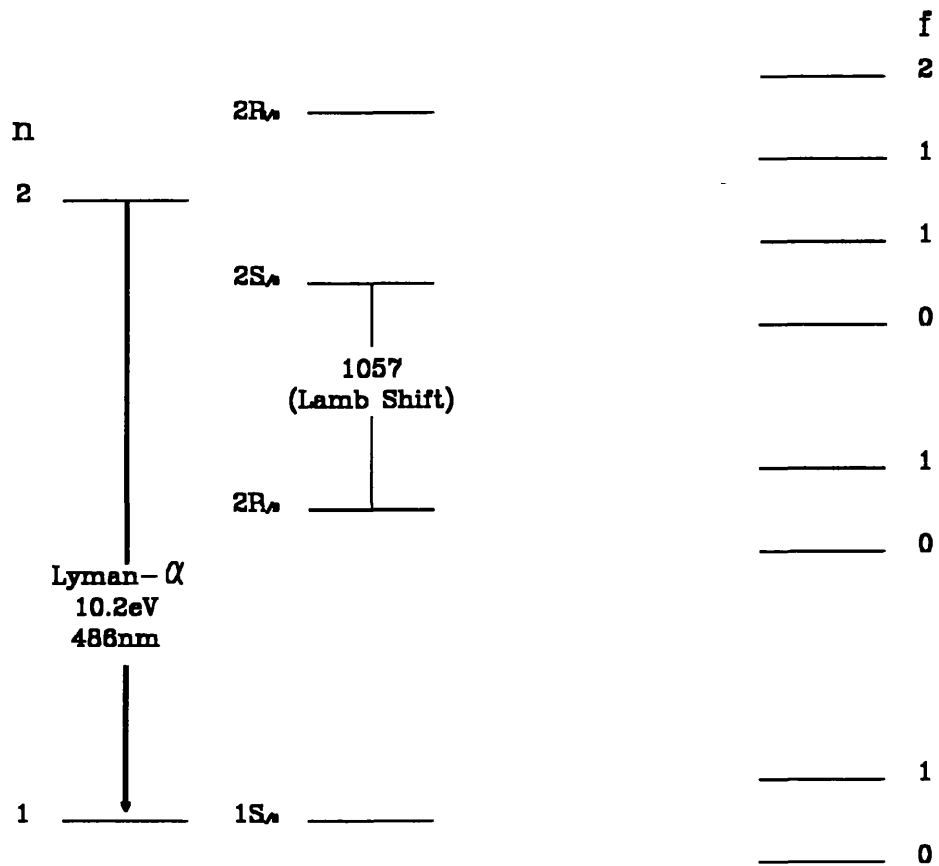
Figure 4.1 The n=1 and n=2 energy levels of hydrogen (top) and positronium (bottom). All intervals in MHz.

123

relative to each other, not the nucleus, and thus contribute to the fine structure of the atom.

4.2 Ground State Positronium as a Testing Ground for QED

When the magnitude of the recoil and radiative correction terms necessary for a complete description of positronuim became known, it was realised that studies of Ps atomic structure could offer many opportunities to test the validity of QED not previously realisable by studies of conventional atoms, particularly those dependent on virtual annihilation. The ground state hyperfine splitting of Ps, $\Delta \nu_{hfs}$ is given by

$$\Delta \nu_{hfs} = \frac{\alpha^4 m_0 c^2}{4} \left[\frac{7}{3} - \frac{\alpha}{\pi} \left(\frac{32}{9} + 2\ln 2 \right) + \frac{5}{6} \alpha^2 \ln \alpha^{-1} + O(\alpha^2) \right] \approx 203.4 \, GHz \quad (4.4)$$

where $O(\alpha^2)$ is the sum of those terms of order α^2, and offers the most sensitive test of QED. This is because the recoil terms and radiative corrections involving annihilation are large, $\sim 10^3$ ppm, in comparison to the uncertainty in the fundamental constants composing the Coulombic (α^4) term which contributes a total uncertainty of 0.22 ppm. By comparison, $\Delta \nu_{hfs}$ for hydrogen is limited to 3 ppm due to uncertainties in the nuclear polarisability. The large corrections in the positronium case, allow researchers to probe the interval as the shifts are much greater than the resolution of such experiments.

Measurement of the G.S. hyperfine interval by direct excitation of the transition is not possible due to the high microwave power that would be needed. However, by immersing the Ps production region in a magnetic field of ~ 8-10kG, the m=0 sub-states are split as shown in fig.4.2. The m=± 1 sub-states are not themselves split by magnetic fields because of the symmetry of the Ps atom, and mixing occurs only between the triplet and singlet m=0 sub-states. This mixing is manifested by a decrease in the observed 3γ events. By monitoring this decrease as a function of the applied magnetic field, the hyperfine splitting may be determined. Deutsch (1951) made the first measurements of the interval to $\pm 15\%$. More recently, researchers (eg. Egan *et al* (1977)) have refined the 'magnetic quenching' method, by inducing a 2GHz Zeeman transition between the magnetically split m=0 and m=± 1 triplet sub-states. A resonance was observed by
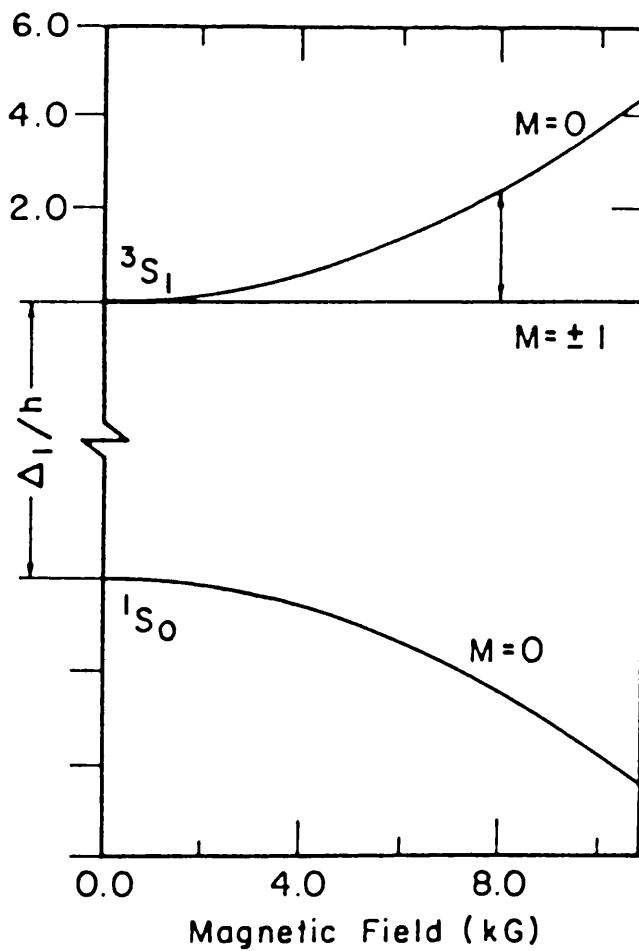
Figure 4.2 The splitting of the m=0 ground state energy levels of positronium, as a function of applied magnetic field

monitoring the 2γ decay rate while keeping the r.f. constant and varying the magnetic field strength. With a knowledge of the r.f. exciting the transition and the magnetic field strength, $\Delta\nu$(hfs) may be deduced. Using the above method $\Delta\nu$(hfs) has been measured to 3ppm (Hughes (1982)) though at this time theory lags experiment as calculations of all of the $O(\alpha^2)$ terms are still outstanding.

Measurements of ground state Ps properties are not restricted to the hyperfine interval, much work has been dedicated to the singlet, 1^1S_0, and triplet, 1^3S_1, lifetimes against annihilation. The first triplet decay rate measurements were made by Deutsch (1951) and singlet by Theriot *et al* (1967). The triplet measurement has received particular attention, initially as it is the easier of the two to measure for it is three orders of magnitude longer, but also as the most sophisticated measurements (Nico *et al* (1992)) differ from theory by more than six standard deviations. Fig.4.3 is a schematic of the system used by Nico *et al* (1992). A lifetime spectrum is obtained using a timed beam of positrons focussed through an aperture into a cylindrical cavity, internally fumed with MgO.
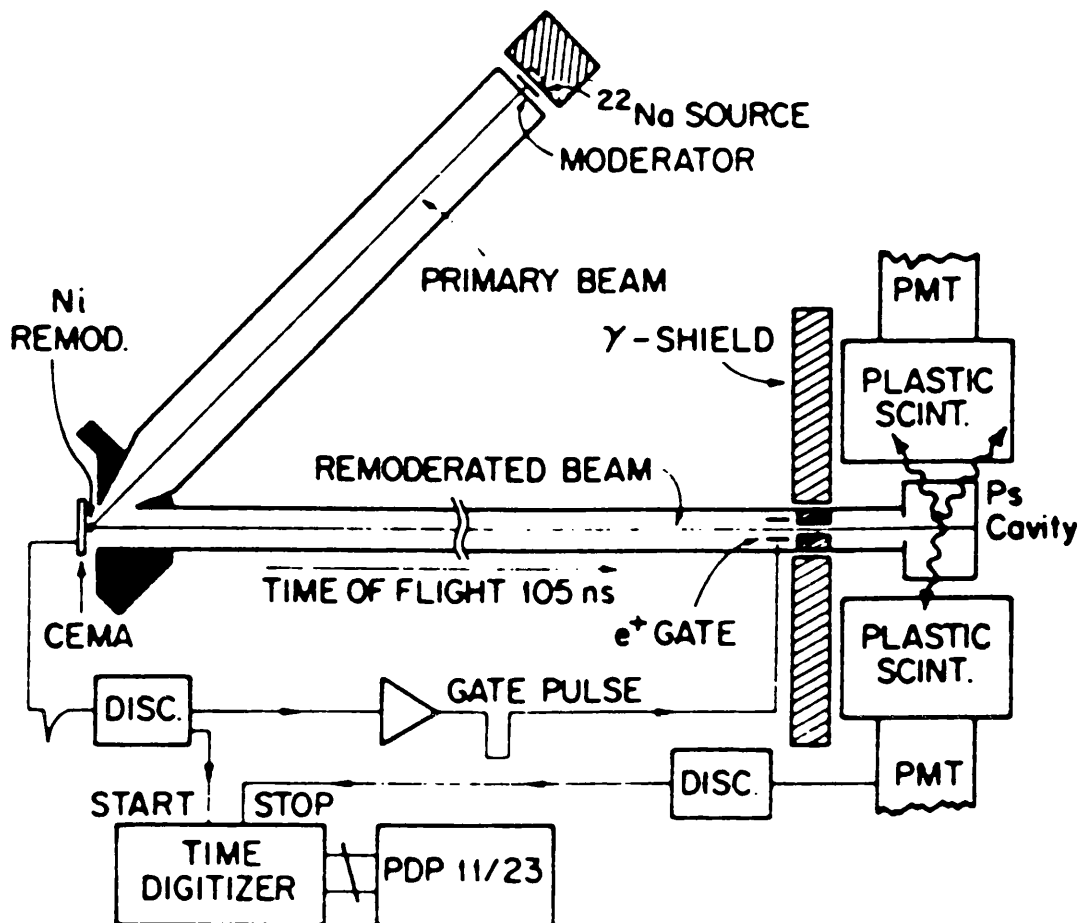
Figure 4.3 A schematic diagram of the apparatus used by Nico *et al* (1992) to measure the positronium 1^3S_1 vacuum decay rate.

At 700eV, 25% of these positrons form ortho-positronium. The MgO coating minimises collisional quenching of the o-Ps which subsequently decays in vacuum by 3γ annihilation, detected by plastic scintillators suitably arranged about the cavity. The cavity itself is necessary to prevent the positronium leaving the field of view of the detectors, as this will lead to disappearance and a shortening of the lifetime. The authors believe that the current discrepancy is not due to systematics and may possibly be resolved when the magnitudes of the higher order corrections are known. Table 4.1 consists of the most recent ground state measurements and calculations.

Table 4.1 Recent experimental and theoretical results for the ground state hyperfine interval, and singlet and triplet decay rates.

	H.F.S	λ_S (n=1) -	λ_T (n=1)
Theory	203400MHz Caswell & Lepage (1979)	7.9852nsec^{-1} Caswell & Lepage (1979)	7.03830(7)μsec^{-1} Adkins (1983)
Experiment	203384.9$\pm$1.2MHz Egan *et al* (1977)	7.994$\pm$0.011nsec^{-1} Gidley *et al* (1982)	7.0482$\pm$0.0016μsec^{-1} Nico *et al* (1992)

4.3 The Excited State

Fulton and Martin (1954) calculated the 2S and 2P energy levels of positronium to order α^3, in which processes not included in the hyperfine splitting were considered. It was concluded that a comparison of these calculations with experiment could provide another highly sensitive test of the two-body formalism.

The annihilation rate of positronium depends on the principal quantum number, the total spin of the atom and angular momentum considerations. When in p-states, annihilation of p-Ps by 2γ-rays and o-Ps by 3γ-rays is forbidden. Alekseev (1958 and 1959) calculated the 2γ-annihilation rate of o-Ps and also the 3γ-annihilation rate of p-Ps, for p-states. For the n=2 states these rates were found to be $\sim 10^4$sec^{-1} and $\sim 10^3$sec^{-1} respectively. This may be compared with the allowed 2P-1S mean transition rate, $\Gamma_{n=2}$, given to the lowest order in α by,

$$\Gamma_{n=2} = \frac{5\pi}{32}\alpha^3\frac{R_{Ps}}{h} = 313.8 \ \mu\text{sec}^{-1} \tag{4.5}$$

where R_{Ps} is the positronium Rydberg energy in Joules (1.089×10^{18}J).

Thus it can be seen that the 2P-states are at least 10^5 times more likely to undergo the optical transition to the ground state than to directly annihilate. Therefore any 2P Ps* produced has a high probability of de-exciting and produce a photon before subsequent annihilation.
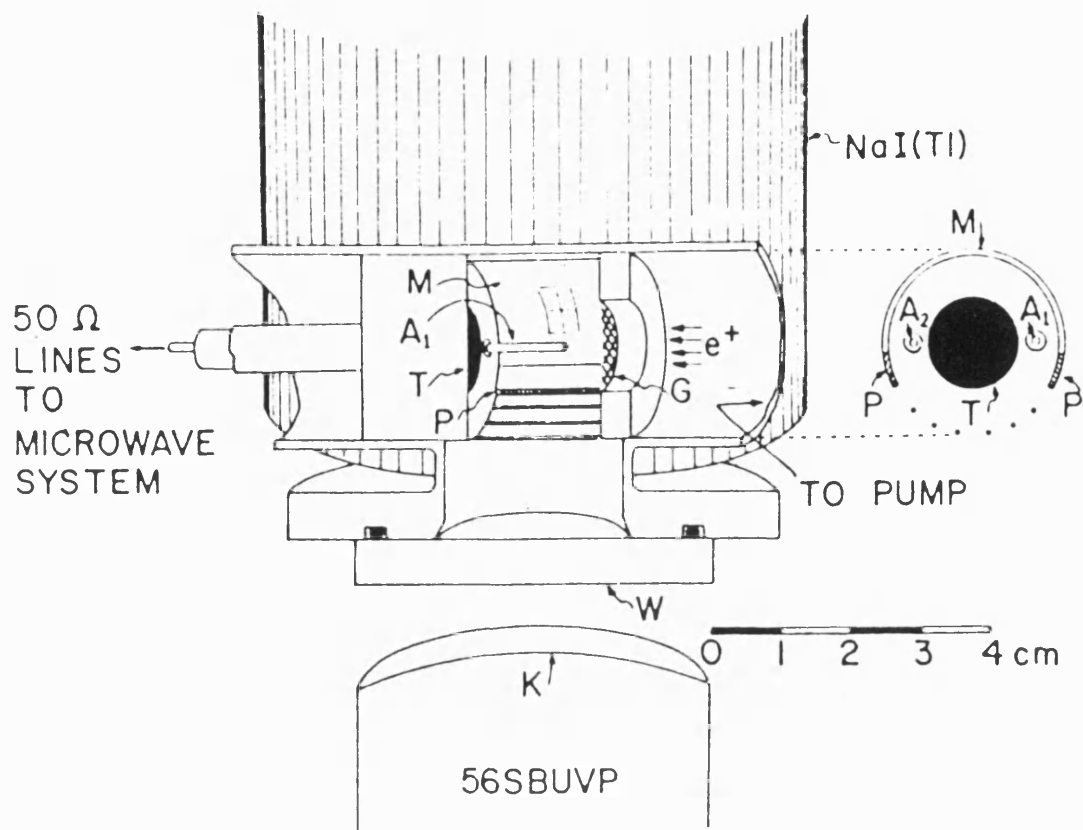
Figure 4.4 A schematic diagram of the apparatus used by Mills *et al* (1975) to measure the positronium 2^3P_2-1^3S_1 fine structure interval.

The 2^3P_J-1^3S_1 fine structure splitting has attracted a great deal of interest since the first observation of Ps* by Canter *et al* in 1975. The first fine structure measurements were made by Mills *et al* (1975). Fig.4.4 is a schematic of the apparatus used. Ps* was formed by slow positrons entering a copper waveguide through a high transmission mesh, and impinging on the opposite wall. A small fraction of these positrons (10^{-3}-10^{-4}) formed Ps*. Assuming an equal distribution in all sixteen available states, 3/16 of this Ps* would be expected to be in the 2^3S_1 level. By using a low magnetic field, approximately 50G, and a positron kinetic energy of 30eV, Zeeman splitting and motional Stark shifts were minimised. Radio frequency power was introduced into the waveguide in the TE_{010} mode so that the electric field in the waveguide was parallel to the positron beam axis. The 2^3S_1-2^3P_2 transition was excited by scanning through with the r.f. and the line centre and linewidth were estimated by observing the increase in the Lyman-α/γ coincidences initiated by the optical decay of the 2^3P_2 positronium and subsequent annihilation of the

ground state. Using this method, the other 2^3S_1-2^3P_J intervals have also been measured and the most recent experimental and theoretical results are given in table 4.2.

Table 4.2 Recent experimental and theoretical results for the 2^3S_1-2^3P_J fine structure intervals.

	2^3S_1-2^3P_2	2^3S_1-2^3P_1	2^3S_1-2^3P_0
Experiment	8617 ± 2MHZ Hagena *et al* (1993)	13010 ± 3MHZ Hagena *et al* (1993)	18494 ± 2MHZ Hagena *et al* (1993)
Theory	8626.21MHz Fell (1992)	13011.86MHz Fell (1992)	18497.10MHz Fell (1992)

In addition to the work on fine structure intervals other work has included measurements of the 1^3S_1-2^3S_1 interval by Doppler free two photon excitation, Chu and Mills (1982) and Chu *et al* (1985), and two photon resonant excitation of postronium high n-states, up to n = 19, by Ziock *et al* (1990). Despite the ever increasing interest in the first and other excited states, to date there has yet to be a direct measurement of the radiative lifetime of any excited state, and it is an attempt to perform such an experiment which is the subject of the rest of this chapter.

4.4 An Experiment to Measure the Radiative Lifetime of the 2P-1S Interval

4.4.1 Introduction

Two experimental arrangements were used for this work as modifications became necessary as a result of the findings of the first experiments and equipment performance. To measure the radiative lifetime, a method of timing Ps* creation was developed. The resulting signal was processed in coincidence with a Lyman-α photon produced on de-excitation of one of the 2P states, and thus from the resulting timing spectrum information regarding the radiative transition obtained. The electrostatic beam introduced in chapter 2 was interfaced with a target for Ps* production and the detectors described below. This beam was used so that in addition to the improved PMT performance the Zeeman splitting and motional Stark shifts which would otherwise occur in a magnetic

field, could be avoided.

4.4.2 Ps* Production and Timing

In order to time the Ps* production a set of CuBe vanes from a disused PMT were situated in front of the CEMA arrangement as described in chapter 2 §.2.9. Fig.4.5 is a schematic showing the principle of operation. A positron incident on the vanes liberates several secondary electrons, their function in a PMT. The geometry of the vanes ensured that around 50% of those secondary electrons were further scattered in the direction of the primary beam, and if a suitable potential difference (100V) was held between the vanes and the first channel-plate electron multiplier array these secondary electrons were detected. The timing resolution of this system was determined by placing the channel plates in coincidence with a plastic scintillator, considered to be the faster detector. The FWHM of the resulting prompt peak was found to be ~2nsec and assumed to reflect the vanes/CEMA resolution though the true resolution of the system was difficult to ascertain because of the processes occurring, such as positron backscattering and subsequent annihilation, and Ps formation. The advantage of tagging in this way is that the vanes intercepted 100% of the beam and difficulties due to stray fields from the high potentials applied to the CEMA's were avoided. In practice, 50% of the primary beam was timed using this method.

As is clear from the results presented in chapter 3, virtually any metallic target in whatever condition may produce copious Ps* on positron bombardment, however in the first experiments the vanes were fumed with MgO, a known Ps converter. Keeping the vanes grounded ensured that the Ps* was emitted into a field free environment and thus Stark effects would be negligible.

4.4.3 Detection of the Lyman-α Signal

Initially it was believed that Ps* yields would be low, ~10^{-3} Ps*/e$^+$ as reported in the earlier work of Schoepf *et al* (1982), and a method to enhance any Lyman-α signal desirable. This was achieved by producing the Ps* inside a reflective quartz sphere of
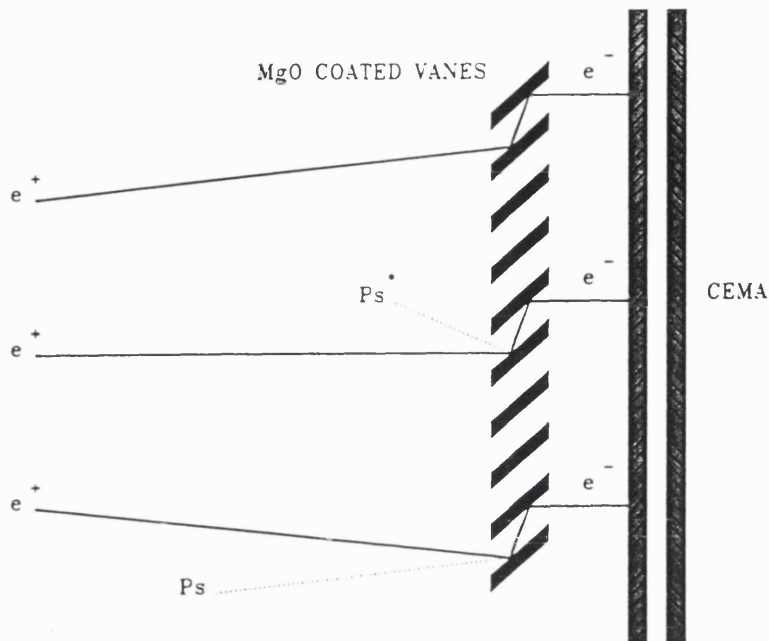
Figure 4.5 A schematic diagram of the positron timing arrangement used in the radiative lifetime experiments.
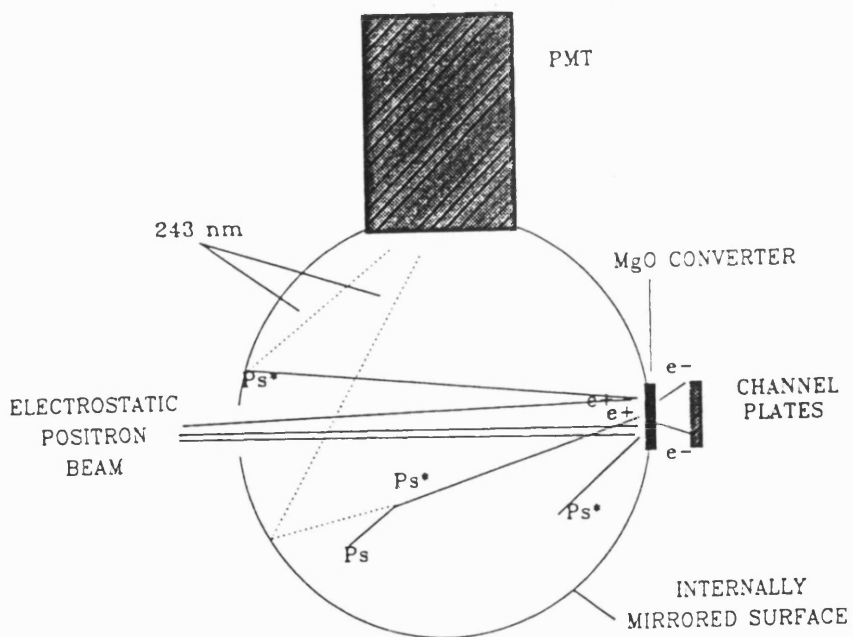
Figure 4.6 A schematic diagram of the reflective sphere and detector arrangement used in the radiative lifetime experiments.

131

9412   9829QA

PHOTO-
CATHODE

QUARTZ
WINDOW
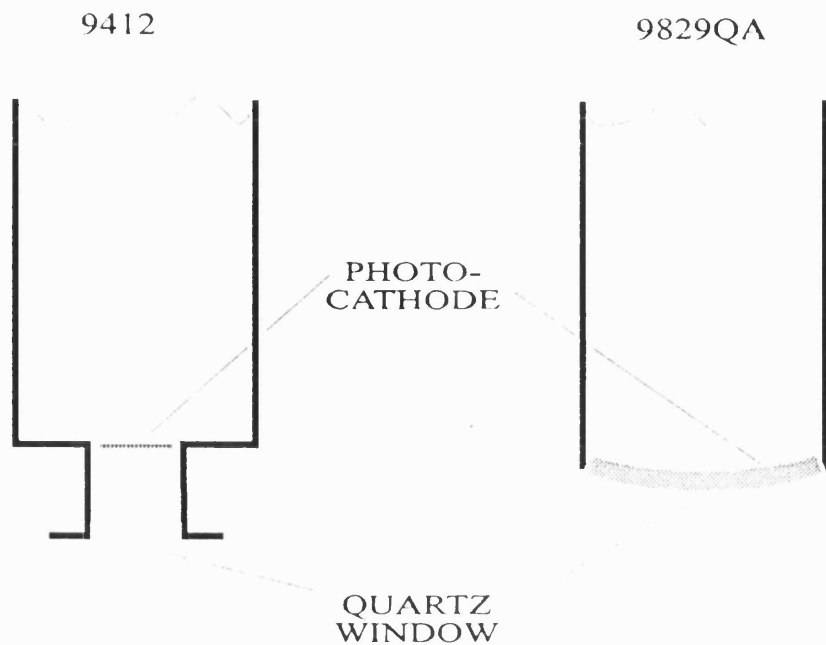
Figure 4.7 Schematic diagrams of the EMI 9412 and EMI 9829QA photomultiplier tubes.

25mm radius. Fig.4.6 is a schematic of the sphere with the detectors arranged around it. The internal surface was coated with a ~ 1000Å aluminium layer, 98% reflective at the 243nm wavelength. A 20mm diameter aperture at the top permitted the photocathode of a PMT to be positioned to intercept the reflected photons. The positrons entered the sphere through a 15mm diameter aperture and were incident on vanes positioned behind another 15mm aperture immediately opposite. It was estimated that approximately 90% of the Lyman-α photons would reach the photocathode, based on the reflective surface-to-aperture area ratio and the 98% reflectivity of the aluminium surface. The PMT used in conjunction with the sphere was a solar blind EMI 9412 tube. This tube had a quantum efficiency of ~ 10% at the 243nm wavelength and an 16mm effective diameter photocathode while in operation the dark count was of the order of 50Hz. Fig.4.7 is a schematic diagram of the EMI 9412 and the EMI 9829QA described in chapter 3 (see below). The construction of the EMI 9412 meant that for the light to be detected, its angle of incidence had to be approximately normal to the quartz window, and thus the tube was highly directional. The EMI 9412 failed during operation and was replaced in the later experiments by the EMI 9829QA tube described in chapter 3.
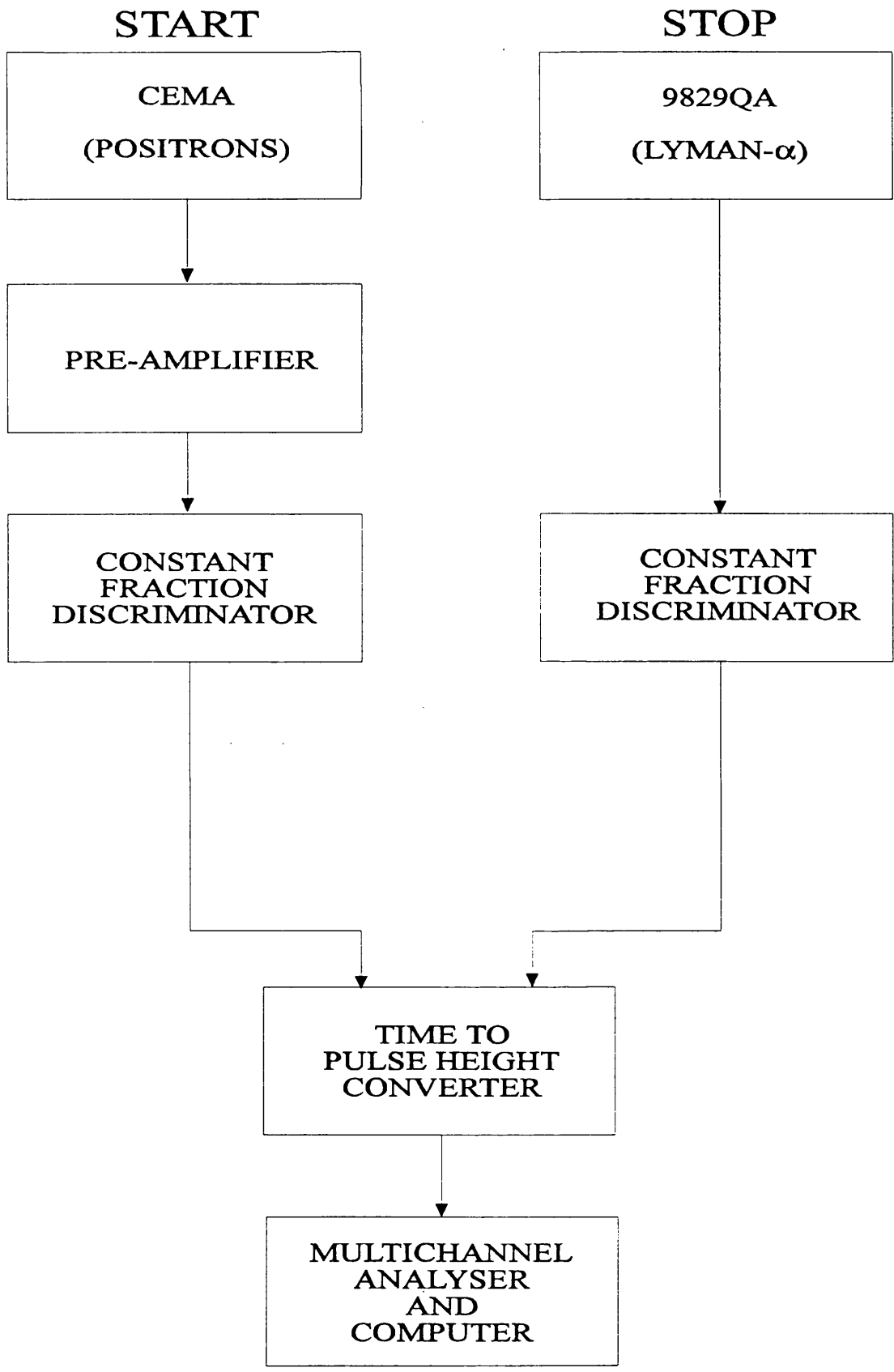
Figure 4.8 A block diagram of the timing electronics used in the radiative lifetime experiments.

4.4.4 The Timing Electronics

Fig.4.8 is a schematic of the electronics used. The output of the CEMA was fed via a ×10 fast preamplifier through an Ortec 463 Constant Fraction Discriminator to the start input of an Ortec 473A Time to Pulse Height Converter (TPHC), and the output of the PMT was fed through an Ortec 584 Constant Fraction Discriminator into the stop input. The output of the TPHC was then fed into an Ortec Maestro II Multichannel Analyser interfaced with a DECpc 222 microcomputer.

4.4.5 Results-Part (i)

These experiments solely used the solar blind EMI 9412 PMT. Fig.4.9 shows two spectra obtained with the sphere in place and a beam of approximately $200e^+s^{-1}$ with an impact energy of 120eV. This work was reported by Day et al (1992). One spectrum (b) was taken with a borosilicate slide between the PMT window and the 20mm diameter aperture at the top of the sphere, and the other spectrum (a) was taken with the slide removed. The MCA time calibration used was 0.125nsec per channel. Spectrum (b) displays a single peak of approximately 3nsec FWHM which corresponds to coincidences between the CEMA's and the PMT induced by positrons being detected by the CEMA's and then promptly annihilating. The resulting γ-rays then scintillate in the quartz window of the tube or elsewhere in the sphere and may give rise to a detectable photon.

Spectrum (a) displays an additional feature. A second very broad distribution can be seen to the right of the zero time peak. Note that in this case the prompt peak will contain, in addition to the γ-ray induced coincidences, a contribution due to 2P-1S de-excitation. The second peak was delayed with respect to the zero time peak by 12-13nsec, had a FWHM of around 20nsec and an asymmetric distribution. As this feature was extinguished by the introduction of the borosilicate slide the wavelength of the light giving rise to this component was estimated to be between 120-290nm, the available window being due to the PMT spectral response and the transmission of the borosilicate slide. To test that this feature was due to positrons only, an electron beam of the same impact energy was used and only random coincidences observed. Given the time delay
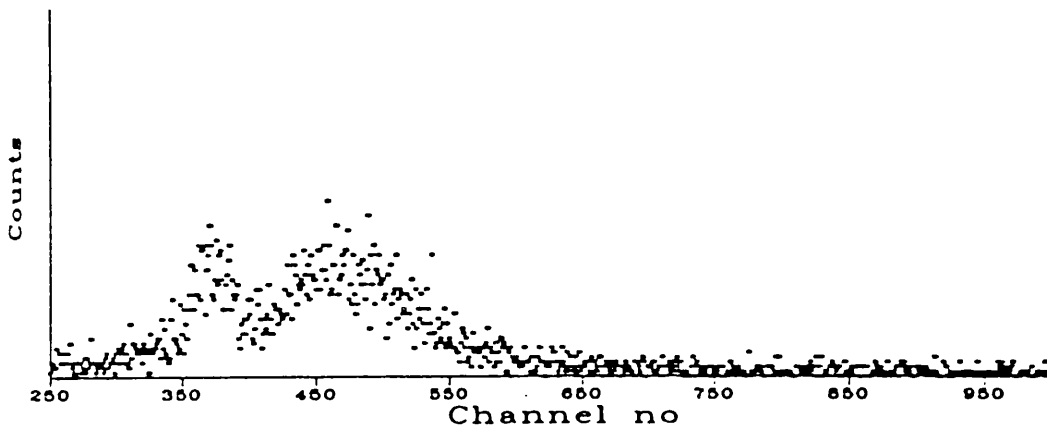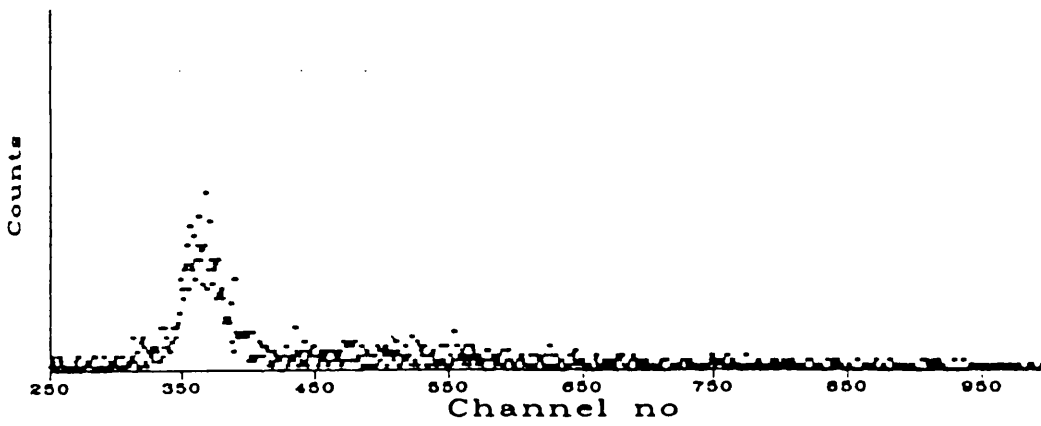
Figure 4.9 Coincidence spectra obtained by impacting 100eV positrons on MgO coated vanes with the sphere in place. Borosilicate slide out (a) and in (b). The time calibration is 0.13nsec/channel.

of the second peak and the fact that the 2P-1S radiative lifetime is ~ 3.2nsec, it is unlikely that enough Ps would survive in a 2P state sufficiently long to give rise to this feature. The lifetime of the metastable 2^3S_1 state, however, is determined by its annihilation rate, approximately 1.1μsec, and so it can be seen that such Ps* could give rise to the delayed signal if a suitable mechanism for de-excitation exists. Given the size of the sphere and the position of the peak, the Ps* kinetic energy was estimated to be of the order of 10eV, and it was proposed that some of the metastable atoms may experience a perturbation close to the sphere walls and thus de-excite before dissociation or quenching.

Although the 2^3S_1 state represents only 3/16 of the total available states, it can be seen that its detection may be enhanced over the twelve 2P states as this component will tend to de-excite away from the target. Of the 2P yield which decays close to the surface of the target, only half would be available for detection as the remainder would be likely to be absorbed by the target. In addition, the metastable atoms may de-excite closer to the PMT itself, and thus further increasing the probability of detection.

The presence of this delayed component held implications for the performance of the original experiment, as the faster elements of the delayed component would be superposed on the region where the 2P signal was to be expected. Further investigations however were prematurely brought to an end as the solar blind tube ceased to function. It was decided to replace the EMI 9412 by a tube with a higher quantum efficiency at the 243nm wavelength.

4.4.6 Results-Part (ii)

When attempting to repeat the experiment, as described in §.4.4.5, unforseen complications arose which led to a radical change in the geometry of the interaction region. The broad wavelength acceptance window of the 9829QA and large photocathode enabled the PMT to be much more sensitive to unwanted scintillations induced by γ-rays. This problem was not present in the work as described in chapter 3 as the order in which the radiations were detected meant that scintillations could be ignored, however in these
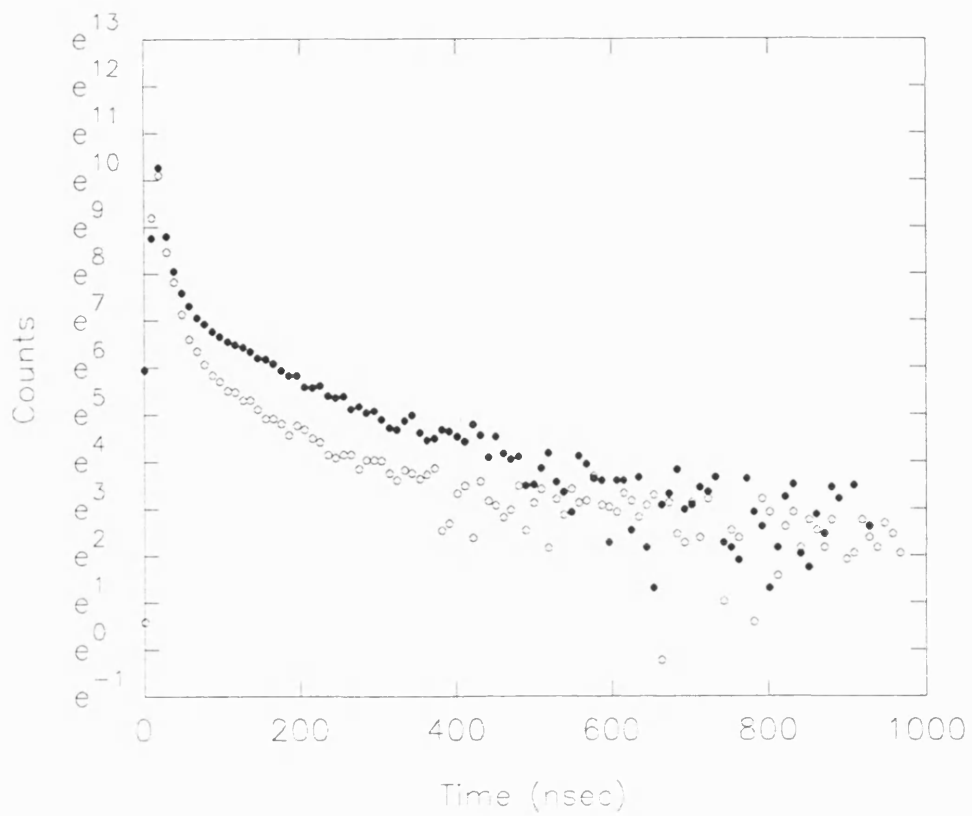
Figure 4.10 Coincidence spectra obtained by impacting 100eV positrons on MgO vanes with the sphere in place. CEMA/EMI9829QA (○) and CEMA/NaI (●).
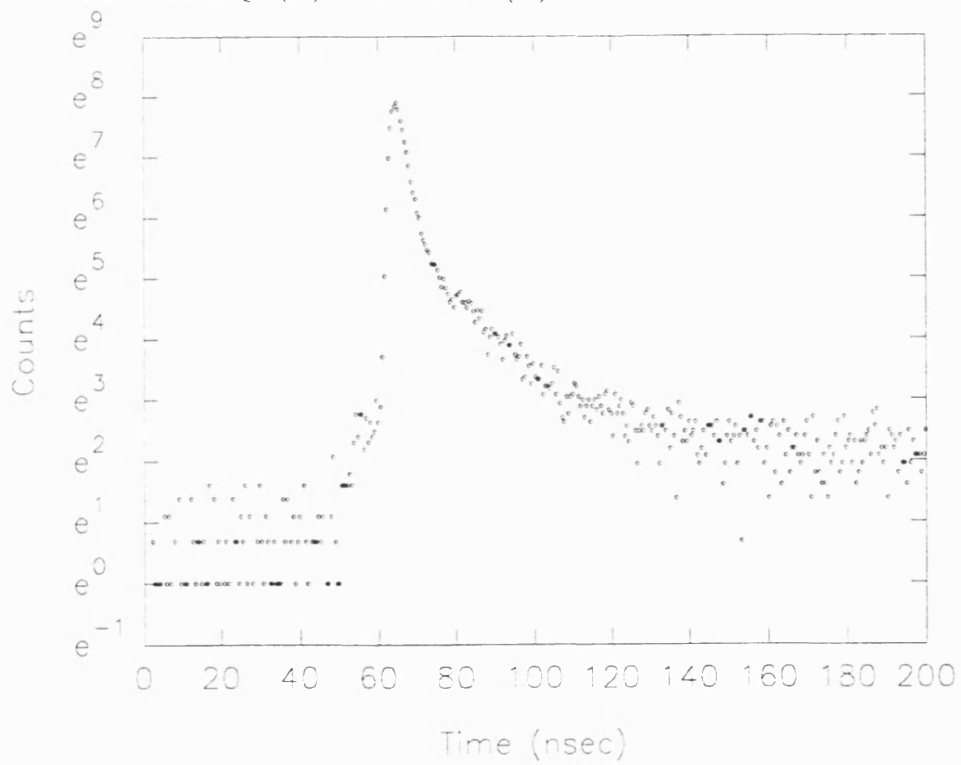
Figure 4.11 Coincidence spectrum obtained by impacting 100eV electrons on MgO vanes with sphere in place.

137

experiments this was not the case. Indeed, inserting the borosilicate shutter simply exacerbated the problem by providing a scintillator to amplify the γ-ray signal. Thus, these spectra were very similar to those obtained with the CEMA's and NaI detector in coincidence. Fig.4.10 (O) is a typical coincidence spectrum between the CEMA's and the 9829QA with the sphere in place and (●) with the NaI detector replacing the 9829QA. The long lived o-Ps component is clearly visible in both spectra. As this signal was not simply background but actually time correlated to the positrons, clearly it would be extremely difficult to separate the wanted 2P-1S signal, and so it was decided to remove the sphere and thus reduce the amount of correlated scintillations.

Removal of the sphere did indeed improve the situation, however with the beam on, there was still a larger number of events recorded by the PMT than would be expected. These counts disappeared with the beam off. To determine the origin of these events the positrons were replaced with an electron beam and the PMT count rate scaled with the relative beam intensity. Fig.4.11 is a coincidence spectrum between the CEMA's and EMI 9829QA with the electron beam on. Copious delayed coincidences can clearly be seen, which with the electron beam switched off would disappear. Finally the electron beam was left on and the plates were switched off. All the additional single events seen by the PMT above the dark count rate disappeared. Thus it was concluded that it was the plates themselves that led to the additional counts. By reducing the voltage across the plates and increasing the external amplification, further reductions to the light were made. Finally by shrouding the plates with neoprene sheet the light levels were reduced sufficiently so that any signal that might be attributable to the 2P-1S Lyman-α transition would be distinguishable. Fig.4.12 is a schematic diagram of this final configuration.

Fig.4.13 is a composite spectrum, taken in this final arrangement, with the aluminium shutter in and out. Note that, contrary to what might be expected, the prompt peak was actually larger with the shutter in. The shutter itself may enhance the γ-ray detection, either by reducing the photon energy in scattering events, thus leading to a more interactive γ-ray, or by virtue of its metallic character, increasing the rate of positron annihilation on contact with the surface. Moving away from the prompt peak, an enhancement can be seen with the shutter out, however, as the shape of the prompt peak
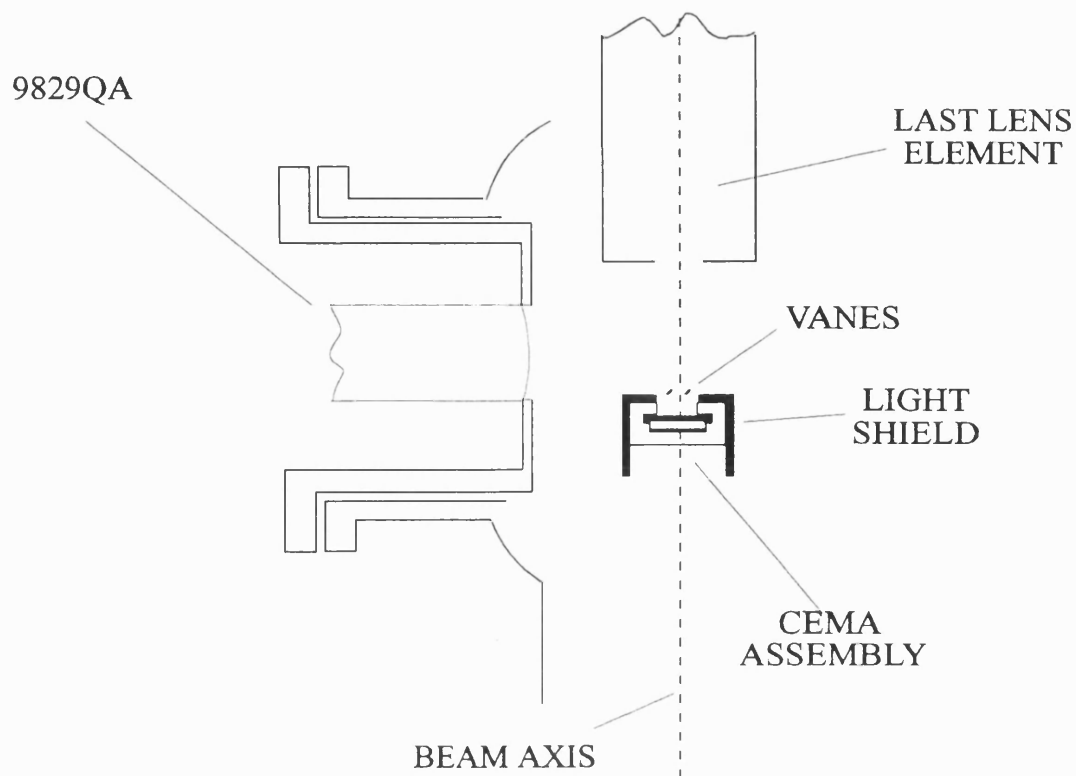
Figure 4.12 A schematic diagram of the interaction region used in the radiative lifetime experiments.
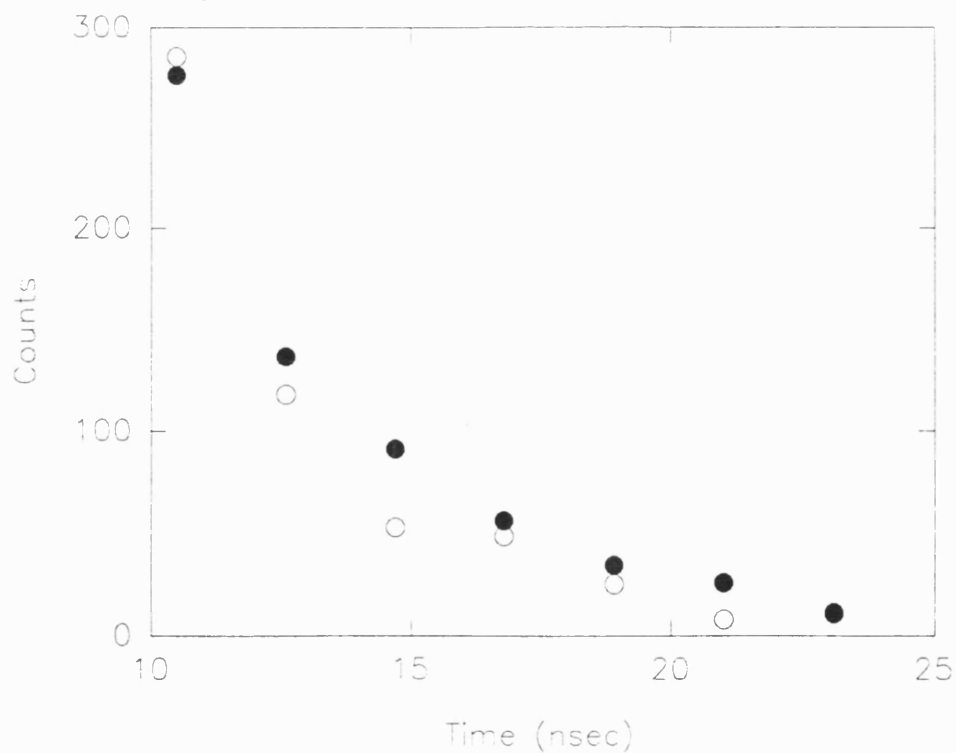
Figure 4.13 A composite coincidence spectrum obtained by impacting 100eV positrons on CuBe vanes with background light sources suppressed. with aluminium shutter in (o) and (•)out.

139

is different in each case it is impossible to make a meaningful fit to the data.

In conclusion, it has been found that the 2P-1S transition signal may be isolated from the other processes which occur when positrons are incident on targets, form positronium and subsequently annihilate, however the steps necessary to allow these observations preclude a detailed analysis of the lifetime. Additional comments on how to improve this situation in the light of the rest of the work in this thesis are given in Chapter 5.

CHAPTER 5

CONCLUSION

The work presented in this thesis falls into three parts, namely: the development of an electrostatic positron beam; the production of excited positronium by positron impact with solid surfaces, and an experiment designed to measure the radiative lifetime of the 2P-1S transition.

The electrostatic beam was designed to operate at low transport energies, $\leq 500\text{eV}$, while retaining beam qualities such as low divergence and small beam diameter. The advantages of using a ^{58}Co positron source has been demonstrated, for although the branching ratio for positron emission is lower than that of ^{22}Na, 15% as opposed to 90%, its high specific activity coupled which mechanical stability allows compact, open sources to be used. As a result loses induced by encapsulation and large emitting area are avoided. With this beam a maximum beam intensity of $170,000\text{e}^+\text{s}^{-1}$ was achieved with a beam diameter of less than 10mm. This beam was operated up to 500eV with no losses, and down to 25eV where losses of 50% were sustained. No measurements of the angular divergence were made, however it was assumed that the maximum divergence would be around $10°$, based on Lagrange's law (see chapter 2 §.2.10).

Using the electrostatic positron beam, studies of Ps* formation by positron impact with untreated surfaces were made. The Ps* was detected by monitoring the coincidences between the Lyman-α photons produced on de-excitation of the 2^3P_J state and γ-rays from the resulting o-Ps decay. From the timing spectra obtained it was possible to integrate over the Ps* signal, and by correcting for detector efficiencies and the number of available substates, the total Ps* yield was estimated. This was done for Be, Cu and Au samples, and also a disused CEMA. There was little difference in the maximum yields from each sample, with the possible exception of the CEMA which is explained in chapter 3 §.3.7, though a clear dependence with energy was observed. The highest yield

141

recorded was ~3% at 75eV impact energy, this value was consistent with the recent measurements of Steiger *et al* (1992), who found yields of ~2% for a wide range of samples also previously untreated. The yields observed in both this work and that of Steiger *et al* (1992) differ considerably from those measured by Schoepf *et al* (1992), around 0.3% from clean, well characterised surfaces. It is important to stress the dependence of these measurements on the assumed efficiencies of the various detectors, for the γ-ray detector this is especially difficult as the detection efficiency for 3γ decay is very dependent on the o-Ps speed and direction as it may move closer to, or further from, the detector, prior to decay, by virtue of its 142nsec lifetime. Thus a knowledge of the kinetic energy of the o-Ps is of paramount importance. Despite these reservations it is unlikely that the overall detection efficiency assumed in this case was underestimated by more than a factor of two, and so significantly high yields of Ps* were certainly observed.

In the work of both Steiger *et al* (1992) and Schoepf *et al* (1992), two Ps velocity distributions were hypothesised to explain an apparent additional exponential component in the timing spectra. The origins of these components were proposed to be epithermal positrons forming Ps* with kinetic energies below 6.8eV, which decayed with a rate close to that of the o-Ps vacuum decay rate, and backscattered positrons. The latter forming Ps* with energies above 6.8eV, and which annihilated on collision with a chamber wall thus giving rise to a component with a much faster decay rate. In this work a single exponential was observed for all impact energies and all targets for times greater than around 150nsec. When fitted it was found to be close to the o-Ps vacuum lifetime. If this component was subtracted a non-exponential component close to the prompt peak was revealed. The overall shape of all the spectra was found to be the same, and this prompted the belief that as opposed to two distinct velocity distributions, only one continuous distribution existed regardless of positron impact energy, and the resulting shape was more to do with a geometrical dependence in the NaI detection efficiency than the sample itself. To test this argument, positron re-emission spectra for positron incident on the Au sample were made. It was found that all the positrons were returned to the surface by a retarding potential of around 10eV, for positron impact energies of 25eV to 250eV. Finally the relative yield of positron re-emitted with energies of ≤ 15eV

was measured as a function of positron impact energy. The resulting yield peaked at 50eV, close to the peak for Ps* production.

The behaviour in the measured Ps* yield at low energies was similar to that of Schoepf *et al* (1992) and Ley *et al* (1990), with the Ps* yield falling off below 25eV. This was in marked contrast to the findings of Steiger *et al* (1992) where it appeared that the total yield was more or less constant from 100eV to 10eV. However, by considering the effects on positrons subject to retardation at the target itself, this behaviour may be explained if positrons are re-emitted by whatever process, since they are then accelerated by the potential difference between the target and another part of the chamber, possibly up to a kinetic energy close to that before retardation. These positrons may then strike some other part of the target assembly, while still in the view of the PMT, and form Ps*.

To take this work further it is important to establish more confidence in the overall detection efficiency. This could be done by forming the Ps* in a container of relatively small dimensions with respect to the γ-ray detector, and place the detector very close to it. By coating the container internally with a reflective material, such as aluminium, loses of the Lyman-α photons could be minimised. Finally by choosing a suitable geometry some degree of focussing may be obtained. A half ellipse for example, could focus u-v photons produced at the target to a photomultiplier, if both target and PMT were situated at the foci.

The effect of contaminants on surfaces would appear to enhance the Ps* yield. This could be investigated by having the facility to anneal and sputter a sample, measure the Ps* yield, then to expose the sample to a known contaminant and remeasure. Of particular interest would be rare gas solids, their ability to re-emit positrons with energies close to their band gap energy may render them efficient sources of Ps*, as these positrons would have sufficient residual energy, due to the large RGS band gap, at the surface to escape with an electron while satisfying the energy balance of eqn.3.13 (chapter 3 §.3.5.4).

With a knowledge of the behaviour of Ps* formation from solids an experiment to measure the radiative lifetime of the 2P-1S transition was made. Many unforeseen

problems arose during this experiment, partially due to necessary change of photomultiplier during the work. It was discovered that many materials will scintillate in the presence of γ-rays with very long decay times, some of the order of hundreds of nanoseconds. In the yield experiments, the order in which the u-v light and γ-rays were detected meant that it was a simple matter to distinguish between true Lyman-α events and scintillations, as they would appear before and after γ-ray detection respectively. In the radiative lifetime experiment however, this was not the case as the coincidence was between a positron detected by a CEMA followed by a photon, and so it became important to reduce the number of background photons. In the early stages of the experiment a solar blind PMT was used. This tube was less susceptible to scintillations due to its restricted spectral window. With this tube evidence for Ps*, particularly in the 2S state was observed. Unfortunately this tube ceased to function and was replaced by another ostensibly more efficient tube. However, the broader spectral window of this tube led to a much greater level of correlated background being observed. In addition, it was also realised that the CEMA's themselves led to further unwanted coincidences as they emitted light when detecting particles. After much work to reduce these sources of correlated background the transition was isolated, however the steps taken to achieve this, precluded an analysis of the lifetime.

As a result of these experiences it is clear that future experiment will benefit by having the positron detection component of the coincidence timing system removed from the Ps* production site. Tagging the positrons using a beam-foil technique at some point before the interaction region would be useful. If the Lyman-α detector was placed in coincidence with two γ-ray detectors set at the 511keV peak, the 2^1P_1 state could be isolated. This state has a lifetime against annihilation of 3.3msec, which occurs via a three photon process. Thus, it will de-excite by a Lyman-α transition to the 1^1S_0 state, where it will rapidly annihilate by a two photon process, which may be easily isolated from o-Ps decay. The reduction in background using this method may prove beneficial when attempting to extract the radiative lifetime as any o-Ps component superposed in the region of interest will be removed.

REFERENCES

Adachi, S., Chiba, M., Hirose, T., Nagayama, S., Nakamitsu, Y, Sato, T. and Yamada, T., Phys. Rev., **A65**, 2634 (1990)

Adams, A., Read, F.H., J. Phys. E, **5**, 150 (1972)

Adkins, G.S., Ann. Phys. (N.Y.), **146**, 78 (1983)

Alekseev, A. I., J. Exptl. Theoret . Phys. (U.S.S.R.), **34**, 1195 (1958)

Alekseev, A. I., J. Exptl. Theoret . Phys. (U.S.S.R.), **36**, 1435 (1959)

Anderson, C. D., Phys. Rev., **41**, 405 (1932)

"Antihydrogen" Proc. Antihydrogen Workshop, (Eades, J., ed.; J.C. Baltzer A.G.) (1993)

Bennett,, W.R., Thomas, W., Hughes, V.W. and Wu, C.S., Bull. Amer. Phys. Soc., **6**, 49 (1961)

Bisi, A., Dupasquier, A. and Zappa, L., J. Phys. C, **4**, L33 (1971)

Blackett P.M.S. and Occhialini, G.P.S., Proc. Roy. Soc., **A139**, (1933)

Brandes, G.R., Canter, K.F. and Mills, A.P., Jr., Phys. Rev. Letts., **61**, 492 (1988)

Brandes, G.R., Mills, A.P., Jr. and Zuckerman, D.M., Materials Science Forum, Vols. 105-110 (1992) pp. 1363-1366

Brock, R.L. and Strieb, J.F., Phys. Rev., **109**, 399 (1958)

Brunings, J., Physica, **1**, 996 (1934)

Canter, K.F., Coleman, P.G., Griffith, T.C. and Heyland, G.R., J. Phys. B, **20**, L167 (1972)

Canter, K.F., Mills, A.P., Jr. and Berko, S. Phys. Rev. Letts., **33**, 177 (1975)

Canter, K.F. and Mills, A.P., Jr., Can. J. Phys. **60**, 551 (1982)

Canter, K.F., Brandes, G.R., Horsky, T.N., Lippel, P.H. and Mills, A.P., Jr., "Positron Studies of Solids, Surfaces and Atoms". Edited by Mills, A.P., Jr., Crane, W.S. and Canter, K.F., (World Scientific Singapore, 1986) pp. 18-27

Canter, K.F., "Positron Studies of Solids, Surfaces and Atoms". Edited by Mills, A.P., Jr., Crane, W.S., and Canter, K.F., (World Scientific Singapore, 1986) pp. 199-206

Canter, K.F., Brandes, G.R., Lippel, P.H. and Mills, A.P., Jr., in "Atomic Physics with Positrons" (Humberston, J.W. and Armour, E.A.G., eds.; Plenum NY) (1987)

145

p153

Caswell, W.E. and Lepage, G.P., Phys. Rev. A, **20**, 36 (1979)

Chang, T-B., Li, Y-Q., Wang, Y-Y. and Tang, X-W., "Positron Annihilation", (Coleman, P.G., Sharman, S.C. and Diana, L.M., eds; World Scientific) 32 (1982)

Chang, Tianbao., Tang, Hsiaowei. and Li Yaoqing., "Positron Annihilation", (Jain, P.C., Sigru, R.M. and Gopinathan, K.P., eds; World Scientific) 212 (1985)

Charlton, M., Griffith, T.C., Heyland, G.R., Lines, K.S. and Wright, G.L., J. Phys. B, **13**, L757 (1980)

Charlton, M., Andersen, L.H., Brun-Nielsen, L., Deutch, B.I., Hvelplund, P., Jacobsen, F.M., Knudsen, H., Laricchia, G., Poulsen, M.R. and Pedersen, J.O., J. Phys. B, **21**, L545

Cherry, W., Ph.D Thesis, Princeton University (1958)

Chu, S. and Mills, A.P., Jr., Phys. Rev. Letts., **52**, 1689 (1984)

Cohen, E.R. and Taylor, B.N., J. Phys. Chem. Ref. Data, **2**, 663 (1973)

Coleman, P.G. and McNutt, J.D., Phys. Rev. Letts., **42**, 1130 (1979)

Costello, D.G., Groce, D.E., Herring, D.F. and McGowan, J.W., Phys. Rev., B5, 1433 (1972a)

Costello, D.G., Groce, D.E., Herring, D.F. and McGowan, J.W., Can. J. Phys., **50**, 1433 (1972b)

Curry, S. and Schawlow, A.L., Phys. Letts., **37A**, 5 (1971)

Dahm, A.J. and Eck., T.G., Phys. Letts., **49A**, 267 (1974)

Dale, J.M., Hulett, L.D. and Pendyala, S., Surf. Int. Anal., **2**, 199 (1980)

Day, D.J., Laricchia, G., Charlton, M., Hyper. Int., **73**, 223 (1992)

Deutch, B.I., Hyper. Int, **73**, 175 (1992)

Deutsch, M., Phys. Rev., **82**, 455 (1951)

Deutsch, M.N., Evans, R.D. and Kendall, H.W., Mass. Inst. Tech. L.N.S.E. Progr. Rep. Nov. 1953

Dirac, P.A.M, Proc. Roy. Soc., **A126**, 360 (1930a)

Dirac, P.A.M, Proc. Camb. Phil. Soc., **26**, 361 (1930b)

Duff, B.G. and Heymann, F.F., Proc. Roy. Soc. London, A272, 363 (1963)

Dupasquier, A., Proc. Int Sch. of Phys., (Brandt, W. and Dupasquier, A, eds.; North

Holland) (1983) pp. 510-558

Egan, P.O., Hughes, V. and Yam, M.H., Phys. Rev., A15, 251 (1977)

Eldrup, M., Vehanen, A., Schultz, P.J. and Lynn, K.G., Phys. Rev. Letts., 51, 2007 (1983)

Fagg, L.W., Nuc. Inst. & Meth., 85, 53 (1970)

Fell, R.N., Phys. Rev. Letts., 68, 25 (1992)

Fischer, D.A., Lynn, K.G. and Gidley, D.W., Phys. Rev., B33, 4479 (1986)

Floeder, K., Fromme, D., Raith, W., Schwab, A. and Sinapius, G., J. Phys. B, 18, 3347 (1989)

Fornari, L.S., Diana, L.M. and Coleman, P.G., Phys. Rev. Letts., 51, 2276 (1983)

Frieze, W.E., Gidley, D.W. and Lynn, K.G., Phys. Rev., B31, 5628 (1985)

Fromme, D., Kruse, G., Raith, W. and Sinapius, G., Phys. Rev. Letts., 57, 3031 (1986)

Fulton, T. and Martin, P.C., Phys. Rev., 95, 811 (1954)

Gidley, D.W., Ph.D. thesis, The University of Michigan, Ann Arbor, (1979) unpublished

Gidley, D.W., Rich, A., Sweetman, E. and West, D., Phys. Rev. Letts., 49, 525 (1982)

Gramsch, E., Throwe, J. and Lynn, K.G., Appl. Phys. Letts., 51, 1862 (1987)

Groce, D.E, Costello, D.G., McGowan, J.W. and Herring, W.F., Bull Am Phys. Soc., 13, 1397 (1968)

Gullikson, E.M. and Mills, A.P., Jr., Phys. Rev. Letts., 57, 376 (1986)

Hagena, D., Ley, R., Weil, D., Werth, G., Arnold, W., Rückert M. and Schneider, H., Hyper. Int., 76, 297 (1993)

Hasbach, P., Hilkert, G., Klempt, E. and Werth, G., Nuovo Cimento, 97A, 419 (1987)

Hewitt, R.N., Noble, C.J. and Bransden, J. Phys. B, 23, 4185 (1990)

Howell, R.H., Rosenberg, I.J. and Fluss, M.J., Phys. Rev., B34, 3069 (1986)

Hughes, R.J. and Deutch, B.I., Phys. Rev. Letts., 69, 578 (1992)

Hughes, V.W, J. Appl. Phys., 28, 16 (1957)

Hughes, V., Private Communication To Gidley, D.W., (1982) unpublished

Hutchins, S.M., Coleman, P.G., Stone, R.J., and West, R.N., J.Phys. E, 19, 282 (1986)

Igarashi, A., Toshima, N., Phys. Rev., A47, 2386 (1993)

Ito, Y., Hirose, M., Kanazawa, I, Sueoka, O. and Tanamura, S., Materails Science Vols 105-110 (1992) pp. 1893-1896

Khan, P., Mazumdar, P.S. and Ghosh, A.S., J. Phys. B, **17**, 4785 (1984)

Khan, P., Mazumdar, P.S. and Ghosh, A.S., Phys. Rev., A**31**, 1405 (1985)

Kielkopf, J.F. and Ouseph, P.J., Bull. Am. Phys. Soc., **19**, 592 (1974)

Kim, L., Pratt, R.H., Seltzer, S.M. and Berger, M.J., Phys. Rev., A**33**, 3002 (1986)

Klemperer, O. and Barnet, M.E., Electron Optics, 3rd Edition (Cambridge Univ. Press) (1971)

Laricchia, G., Charlton,. M., Clark, G. and Griffith, T.C., Phys. Letts., 109A, 97 (1985)

Laricchia, G., Charlton,. M., Davies, S.A., Beling, C.D. and Griffith, T.C., J. Phys. B, **20**, L99 (1987)

Laricchia, G., Davies, S.A., Charlton,. M. and Griffith, T.C., J. Phys. E, **21**, 886 (1988)

Lennard, W.N., Schultz, P.J. and Massoumi, G.R., Nucl. Inst. Meth., B**33**, 128 (1988)

Ley, R., Niebling, K.D., Werth, G., Hahn, C., Schneider, H. and Tobe, I., J. Phys. B, **23**, 37 (1990)

Lo, C. and Girardeau, M.D., Phys. Rev., A**41**, 158 (1990)

Lynn, K.G., Nielsen, B. and Quateman, J.H., Appl. Phys. Letts., **47**, 239 (1985)

Lynn, K.G. and Nielsen, B. Phys. Rev. Letts., **58**, 81 (1987)

Mandal, P., Guha, S. and Sil, N.C., J. Phys. B, **12**, 2913 (1979)

Mandal, P., Guha, S. and Sil, N.C., Phys. Rev., A**22**, 2623 (1980)

Mandanski, L. and Rasetti, F., Phys. Rev., **79**, 397, (1950)

Marshall, D.J., Cathodoluminescence of Geological Materials, 1st Edition (Unnin Hyman Ltd.) (1988)

Massey, H.S.W. and Mohr, C.B.O, Proc. Phys. Soc., **67**, 695 (1954)

McCall, S., Bull. Amer. Phys. Soc., **18**, 1512 (1973)

Merrison, J.P., Charlton, M., Deutch, B.I., and Jørgensen, L.V., J. Phys. Condens. Matter, **4**, L207 (1992)

Mikhailov, A.I., and Porsev, S.G., J. Phys. B, **25**, 1097 (1992)

Mills, A.P., Jr., Berko, S. and Canter, K.F., Phys. Rev. Letts., **33**, 1541 (1975)

Mills, A.P., Jr., Platzman, P.M. and Brown, B.L., Phys. Rev. Letts., **41**, 1076 (1978)

Mills, A.P., Jr. and Pfieffer, L., Phys. Rev. Letts., **43**, 1961 (1979)

Mills, A.P., Jr., Appl. Phys. Letts., **37**, 667 (1980b)

Mills, A.P., Jr. and Crane, W.S., Phys. Rev. A, **31**, 593 (1985)

Mills, A.P., Jr. and Pfieffer, L., Phys. Rev., **B32**, 53 (1985)

Mills, A.P., Jr. and Guillikson, E.M., Appl. Phys. Letts., **49**, 1121 (1986)

Mogensen, O.E., J. Chem. Phys., **60**, 998 (1974)

Mogensen, O.E., Shantarovich, V.P., Chem. Phys., **6**, 100 (1974)

Murray, C.A. and Mills, A.P., Jr., Solid State Comm., **34**, 789 (1980)

Nico, J.S., Gidley, D.W., Skalsey, M. and Zitzewitz, P.W., Materials Science Forum, Vols. 105-110, (1992) pp. 401-410

Nieminen, R.M. and Oliva, J., Phys. Rev., **B22**, 2226 (1980)

Ore, A., Univ. of Bergen Arbok, **9** (1949)

Ore, A. and Powell, J.L., Phys. Rev., **75**, 1696 (1949)

Overton, N., Mills, R.J., Coleman, P.G., submitted To J. Phys. B, (1993)

Peach, G., Willis, S.L. and McDowell, M.R.C., J. Phys. B, **18**, 3921 (1985)

Paulin, R. and Ambrosino, G., J.Phys. (Paris), **29**, 263 (1968)

Read, F.H., Adams, A., and Soto-Montiel, J.R., J. Phys. E, **4**, 625 (1971)

Risley, J.S., Rev. Sci. Instrum., 43, **1**, 95 (1972)

Salpeter, E.E. and Bethe, H.A., Phys. Rev., **84**, 1232 (1951)

Schoepf, D.C., Berko, S., Canter, K.F. and Sferlazzo, P., Phys. Rev., A45, 1407 (1992)

Schultz, P.J. and Campbell, J.L., Phys. Letts., **A112**, 316 (1985)

Schultz, P.J. and Lynn, K.G., Rev. Mod. Phys., **60**, 701 (1988)

Schwinger, J., Proc. Natl. Acad. Sci. U.S., **37**, 452, 455 (1951)

Shearer, J.W. and Deutsch, M., Phys. Rev. **76**, 462 (1949)

Shimizu, S., Mukoyama, T. and Nakayama, Y., Phys. Letts., **17**, 295 (1965)

Soa, E.A., Jenear Jahrbuch (1959) I, pp.115-153

Sodickson, L., Bowmann, W. and Stephenson, J., Phys. Rev., **124**, 1851 (1961)

Sperber, W., Becker, D., Lynn, K.G., Raith, W., Schwab, A., Sinapius, G., Spicher, G., Weber, M., Phys. Rev. Letts., **68**, 3690 (1992)

Steiger, T.D. and Conti, R.S., Phys. Rev., A45, 2744 (1992)

Stein, T.S., Kauppila, W.E. and Roellig, L.O., Rev. Sci. Inst., **45**, 951 (1974)

Stein, T.S., Kauppila, W.E., Kwan, C.K., Parikh, S.P. and Zhou, S., Hyper. Int., **73**, 53, (1992)

Theriot, E.D., Beers, R.H. and Hughes, V., Phys. Rev. Letts., **18**, 767 (1967)

Theriot, E.D., Beers, R.H. and Hughes, V. and Ziock, K.O.H., Phys. Rev., A2, 7070 (1970)

Valkealahti, S. and Nieminen, R.M., Appl. Phys. A32, 95 (1983)

Varghese, S.L., Ensberg, E.S., Hughes, V.W. and Lindgren, I., Phys. Letts., **49A**, 415 (1974)

Vehanen, A., Lynn, K.G., Schultz, P.J. and Eldrup, M., Appl. Phys., A32, 163 (1983)

Weber, M., Schwab, A., Becker, D. and Lynn, K.G., Hyper. Int., **73**, 147 (1992)

Weiss, A.H., Rosenberg, I.J., Canter, K.F., Duke, C.B. and Paton A., Phys. Rev., B**27**, 867 (1983)

Weyl, H., "Gruppentheorie und Quantenmechanik" 2nd ed., p234 (1931)

Yang, C.N., Phys. Rev., **77**, 242 (1950)

Zafar, N., Chevallier, J., Jacobsen, F.M., Charlton, M. and Laricchia, G., Appl. Phys., A**47**, 409 (1988)

Zafar, N., Ph.D Thesis, University College London (1990) unpublished

Zafar, N., Laricchia, G., Charlton, M. and Griffith, T.C., J. Phys. B, **24**, 4661 (1991)

Zhang, C., Tzoar, N. and Platzman, P.M., Phys. Rev., B**37**, 7326 (1988)

Ziock, K. P., Howell, R.H., Magnotta, F. and Failor, R.A., Phys. Rev. Letts., **64**, 2366 (1990)